Kinetics of Competing Reactions on Metal Oxide Semiconductors during the Course of Photoelectrochemical Water Oxidation

Charles R. Lhermitte

A dissertation submitted in partial fulfillment
of the requirements for the degree of
Doctor of Philosophy
(Chemistry)
in the University of Michigan
2017

Doctoral Committee:

Associate Professor Bart M. Bartlett, Chair
Professor Raoul Kopelman
Associate Professor Stephen Maldonado
Associate Professor Vanessa Sih

To my papa, maman, brother and nanny without whom I could not have succeeded

Acknowledgements

I would first like to thank my father, the original Dr. Lhermitte, for everything that he has done for me and my family. My Papa always did the best he could to support us and always encouraged my continued education. His number one priority has always been his family and I retain no doubts about the magnitude of his love and appreciation for us. He was an amazing researcher and professor, living on the cutting edge between science and technology and has been described by many of his esteemed colleagues as a giant in his field and true pioneer in radar meteorology. It is in great part thanks to him that the system of Doppler radars that we use today to investigate and understand weather patterns even exists. He has been and always will be my inspiration and I will keep him close to my heart until the last of my breath. I can only hope that one day I might have a similar impact on my field, but indeed the bar has been set high with his past achievements. There are no words nor phrases that are sufficient to describe how much I miss him, although an excerpt from a poem by Dylan Thomas comes to mind:

"And you, my father, there on the sad height,
Curse, bless, me now with your fierce tears, I pray.
Do not go gentle into that good night.
Rage, rage against the dying of the light."

He was fighter until the end, and I hope to embody his fighting spirit. *Papa, je t'aime très fort et tu me manques terriblement. J'espère que tu es confortable au Paradis avec tonton Andre.*

Next I would like to thank my mother for her continued love and support. My mom, has always had my back and she is one of the most intelligent and amazing people I know. Her kindness and love knows no bounds and I am forever grateful to have her in my life.

My brother Julien has been an inspiration to me as well. He is one of the most intelligent physicists that I have ever met and I am in awe of his intellectual capacity. Julien has always been on my side and even been my fiercest protector at times. I have been lucky to grow up with a

brother who I could bother to tutor me in calculus and physics and the successes that I had when studying those subjects are in part thanks to him.

I would be remiss if I omitted my grandmother. Once again I find myself lucky to have such a caring spirit in my life. Despite how far away she is, I know that she will always be there for me. Je t'aime très fort Nanny!

I would also like to thank all of my lab mates, past and present, for their support over the years. Jimmy and Kim, thank you for being such good friends. I will miss going over to your place for board game nights. Joe, thank you for showing me the ropes in lab and being a good mentor. I learned a lot from you and really appreciate the time you took to help me along my way. Tanya, thank you for all your help and support over the years, especially with providing advice on the post doc search. Kayla, you were my desk mate for so many years! You are a great friend and I genuinely appreciate all that you have done for me and the rest of the lab. You were always there for practice talks and helpful discussions and you helped push me with all of your questions. It meant a lot to me that you were always there to help. Emily, thanks for all your support as well in addition to all the rides to the airport! Ben and Doodle thanks for being good friends!

To the young Bartlett lab members, Aaron, Sam, Adam and Andy, thanks for all the good times. I had lots of fun going on camping trips, riding motorcycles, playing board games and talking trash about fantasy football (Jarvis Landry was such a disappointment!). I really hope that you guys turn the lab camping trip into a tradition because it really was a blast. Also, I can't forget Dan and John D.! Dan thanks so much for your patience in attending all my post doc practice talks and thanks for being a great lab mate. John, thanks for being such a great friend and desk mate. You have really helped to make our lab atmosphere great and I'm going to miss working alongside you.

Special recognition must also be given to some of my past mentors. Mrs. Barkow, my high school chemistry teacher was the first person to really expose me to the wonders of chemistry. Although I actually was an awful student in her class at first, her drive and encouragement helped me to push past barriers and eventually become one of her best students. I learned a lot about the merit of hard work and persistence in her class and I will carry those lessons with me for the rest of my life. Next I must also acknowledge my undergraduate advisor, Dr. Carl D. Hoff for his

encouragement and support as well. Dr. Hoff has been an excellent mentor who I have always been able to count on over the years.

I must also thank my girlfriend Samantha for all her love and support. I know that it has been difficult at times to deal with me, especially with all the stress and mood swings that this PhD. has caused. But she has always been there to push me and help me along my way. Words can't express my appreciation for you and how happy I am to have you in my life.

My Miami people, Khalil, Julian, Thomas I. and Manu must not be forgotten as well. I have known all four of you for almost two decades. We grew up together and I am very grateful that we are still such great friends. You guys have been there for me when I really needed you and I will never forget that. Good friends are hard to find but I seem to have hit the jackpot with you. I looked forward to many more years of friendship and good times.

Next I would like to thank my committee members Prof. Maldonado, Prof. Sih, and Prof. Kopelman. Thank you for being on my committee and for your help and guidance over the years. Finally I would like to thank my advisor Prof. Bart Bartlett. Thank you for all your help and support over the years. I would especially like to thank you for your kindness and understanding during the difficult times that I have had in graduate school. I am happy that I was able to work in your lab during my graduate studies. I could not have asked for a better advisor. I'm a bit sad that it will all be over soon, but I will keep with me and cherish all the memories from the time I spent in your lab.

I have been lucky to have developed such a strong network of friends and family over the years. Without all of you (and others too!) I would not be where I am today. To anyone who I might have forgotten to add to this, I am sorry! I am blessed to have so many wonderful people in my life. Honestly, there is so much more that I would like to write, however, I could probably write another whole thesis just thanking people so I must stop here.

I often find written words to be insufficient to describe the importance of all your support, but seriously, *thank you for everything*.

Table of Contents

List of Figures

List of Abbreviations

Ag/AgCl	silver / silver chloride reference electrode
AMT	ammonium metatungstate
CB	conduction band
CL-LSV	linear sweep voltammogram conducted under chopped illumination
CPC	controlled potential coulometry
$CuCl_2$	copper (II) chloride
D-LSV	linear sweep voltammogram conducted in the dark
EC	electrochemical
EDTA	ethylenediaminetetraacetic acid
EDX	electron dispersive X-ray spectroscopy
E_f	Fermi level
E_g	band gap energy
e^-/h^+	electron/hole pair
EIS	electrochemical impedance spectroscopy
$FeCl_2$	iron (II) chloride
HER	hydrogen evolution reaction / proton reduction from water
HOMO	highest occupied molecular orbital
KB_i	aqueous potassium borate solution
KP_i	aqueous potassium phosphate solution
L-LSV	linear sweep voltammogram conducted under illumination
LSV	linear sweep voltammogram
LUMO	lowest unoccupied molecular orbital
MO	metal oxide

NHE	normal hydrogen electrode
OER	oxygen evolution reaction / water oxidation
PCET	proton coupled electron transfer
PEC	photoelectrochemical
RHE	reversible hydrogen electrode
RRDE	rotating ring disk electrode
RRDPE	rotating ring disk photoelectrode
SEM	scanning electron micrograph
SP	spray pyrolysis
UV	ultraviolet
VB	valence band
UV	visible
WO_3	tungsten oxide
WO_3:Pt	tungsten oxide thin film grown on a Pt disk electrode
XPS	X-ray photoemission spectroscopy
XRD	X-ray diffractogram

List of Appendices

Abstract

Photoelectrochemical (PEC) water splitting is a sustainable and environmentally friendly method for the conversion of solar energy into a portable H_2 fuel. However, in order to drive the paradigm shift toward these new sources of energy, the efficiency of this process must be improved to make it a cost competitive means of solar energy storage. Because the oxygen evolution reaction (OER) is the kinetically slowest step for overall water splitting, it is imperative to develop materials that demonstrate high efficiencies and turnover frequencies for this reaction. This would allow photoelectrochemical cells to achieve the requisite efficiencies to make them a competitive means of solar energy storage.

As a result, this thesis focuses on developing metal oxides capable of using visible light to drive water oxidation in addition to obtaining a more fundamental understanding of the kinetics of the processes that take place on the electrode surface. The major contribution of the work presented in this thesis focuses on understanding how the catalysis of a few select metal oxide materials may be affected via doping or through the addition of co-catalysts. Furthermore, particular emphasis is placed on understanding how competitive side reactions, such as electrode degradation and anion oxidation, may affect the OER efficiency of metal oxide photoelectrodes.

WO_3 was first evaluated as a visible light absorbing photoelectrode for water oxidation. However, this material demonstrates poor stability and Faradaic efficiency for OER under photoelectrochemical conditions. To improve these latter two aspects, a solid state FeOOH co-catalyst was grown on the surface of the WO_3. Through the use of a combination of electrochemistry, SEM imaging, and UV-Vis spectroscopy, it was observed that the FeOOH surface layer plays a significant role in improving the resulting electrode's stability. Moreover, this surface layer also imparts a Faradaic efficiency for OER of nearly 100%—a 70% improvement,—during the course of extended electrolysis of water. Furthermore, the role of anion oxidation in addition to the possible formation of detrimental peroxide intermediates during the course of PEC OER was investigated using a novel rotating ring disk photoelectrode (RRDPE)

technique. Anion oxidation was observed to only account for a small fraction of observed current. Moreover, peroxide formation is not observed under acidic conditions (1N H_2SO_4 and 1N H_3PO_4). Instead, electrochemical, SEM imaging, and spectroscopic data suggest that the observed photocurrent degradation in acidic solution may primarily result from the oxidation of reduced W sites present in the electrode and not from detrimental side reactions that degrade the electrode itself.

Ternary phase metal oxides were also investigated as OER photoelectrodes. By incorporating Cu into WO_3, the ternary phase $CuWO_4$ is formed. Including the secondary metal cation reduces the band gap from 2.7 to 2.2 eV which improves visible light absorption. Furthermore, $CuWO_4$ demonstrates near unity Faradaic efficiency for OER, even in the presence of more kinetically accessible anions such as Cl^-. Despite this, $CuWO_4$ demonstrates large (161 mV/dec) Tafel slopes which suggest that the kinetics of OER may be slow. In an effort to improve the kinetics, spray pyrolysis was employed to produce thin film solid solutions of $Cu_{1-x}Co_xWO_4$. The photo-inactive $CoWO_4$ demonstrates a high turnover frequency for OER in the dark. Therefore, it was hypothesized that the incorporation of Co^{2+} into $CuWO_4$ to form $Cu_{1-x}Co_xWO_4$ solid solutions would yield photoelectrodes that demonstrate higher turnover frequency for photoelectrochemical OER. It is demonstrated that high purity thin film solid solutions of these materials can be produced using a simple spray pyrolysis procedure. Furthermore, we find through a combination of UV-Vis spectroscopy, XRD, and electrochemistry that although both the dark catalysis and visible light absorption is enhanced in the $Cu_{1-x}Co_xWO_4$ thin films, the presence of Co^{2+} introduces trap states which quench the photocurrent.

Finally, in an effort to synthesize visible light absorbing ternary metal oxide phases that lack inter band gap trap states, the ternary phase metal oxide, $PbCrO_4$, was investigated. This material was selected due to its combination of a d^{10}/d^0 metal cations which was hypothesized to reduce the probability of the formation of trap states due to the absence of partially filled d-orbitals. To produce thin films electrodes of this material, a novel spray pyrolysis synthesis was developed that used the chelating ligand, ethylenediaminetetraacetic acid (EDTA), to stop the precipitation reaction between Pb^{2+} and Cr^{6+} salts. This, in turn, yielded stable precursor solutions that could be spray deposited to form thin film $PbCrO_4$ electrodes. The resulting $PbCrO_4$ electrodes were investigated using a combination of electrochemistry, XPS, and SEM imaging to understand the

nature of their reactivity. The data indicate that $PbCrO_4$ is a 2.2 eV band gap semiconductor that demonstrates a large absorption coefficient for visible light (2400 cm^{-1} at 516 nm). However, this material is unstable during the photoelectrolysis of water and decomposition reactions were observed to out compete OER and eventually shut down the reactivity of the electrode over time. Despite this material's poor stability in aqueous solution, it demonstrates promise as a photoelectrode for organic oxidation reactions since it exhibits higher stability during the course of photoelectrochemical methanol oxidation in a 10% v/v methanol aqueous solution.

Chapter 1

Introduction

1.1 Challenges with Solar Energy

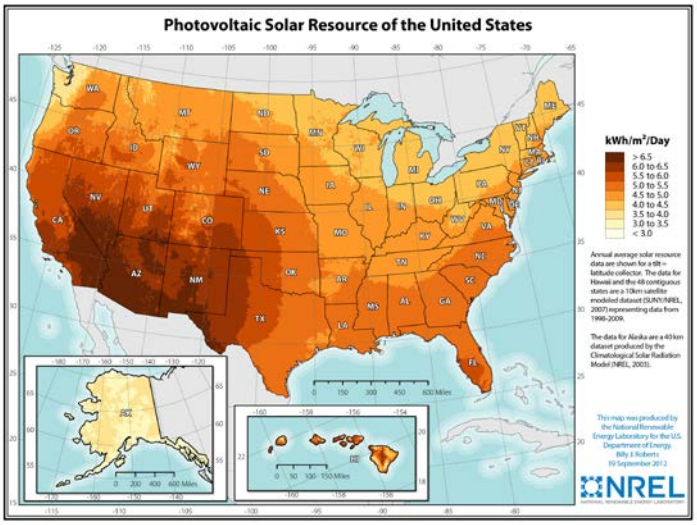

Figure 1.1: Photovoltaic solar resources of the United States. Reproduced from ref. 14.

The sun provides us with enough energy in one hour to power our planet for one year.[1–3] As a result, solar energy has emerged as a popular replacement for fossil fuels over the last few decades. Indeed, the amount of research efforts devoted to improving solar harvesting efficiencies has increased exponentially this last decade.[3–13] Although solar energy is an attractive means of providing electrical energy, a few challenges remain. First, solar irradiation is not homogeneous across the planet so not all regions on Earth receive the same amount of sunlight (Figure 1.1).[14] Furthermore, sunlight will vary across the day as a function of time (day vs. night), weather (cloudy day) or season (less sunlight during winter months). As a result, the sporadic nature of this renewable makes it difficult to implement and highlights the importance of developing a means of storing this energy to increase solar energy's grid penetration.

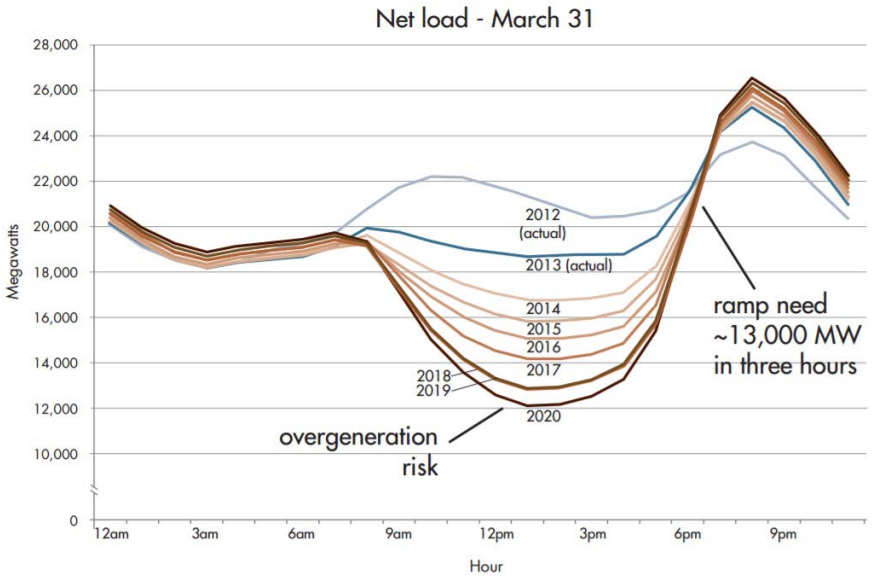

Figure 1.2: "duck curve" depicting grid load on March 31 in California from 2012 and projected out to 2020. During mid-day, the grid load decreases which puts the grid at a higher over generation risk if coupled with solar resources since that is peak time for solar production. Reproduced from ref. 15.

Furthermore, another prominent challenge associated with solar and other forms of renewable energy is the potential for grid overload. Figure 1.2 depicts the grid load, or amount of energy drawn by the population, from a study conducted by the California ISO.[15] It is observed that the load placed on the grid varies significantly during the day. Of particular importance is the decrease in grid load during the mid-day between 12-3pm. Because the amount of energy drawn by the population is at its lowest during these hours, this is the time of day most susceptible to over generation risk from renewable energy.[15] Since photovoltaics continuously pump energy while the sun is shining, if the amount of energy drawn by the population is lower than that produced by a solar farm, this introduces a significant risk for overproduction which would overload the grid. As a result, this highlights the need to develop new means of solar energy storage to allow a place for all this extra energy to go. Furthermore, if this energy could be pumped into a fuel generator this would allow us a means of storing the extra energy in the form of a portable chemical fuel.

To date, there are multiple means of storing solar energy available, but they still possess drawbacks that prevent their widespread implementation.[16] Currently, the most widely implemented means of solar energy storage take the form of ion intercalation batteries and thermal storage using molten salts.[16] However, these forms of energy storage have the drawback of requiring large amounts of space in addition to issues associated with battery lifetime and

cyclability. Furthermore, energy density of these storage systems and technical complications (such as the exceedingly high temperatures of thermal molten salts) make them difficult to implement on a smaller scale and makes it almost impossible to package them in transportable forms that would aid in spreading their grid impact over a wider area.

However, it is possible to directly store solar energy in the form of chemical bonds in a process known as photolysis. In fact, plants and some small microbes have been using photolysis to power the photosynthesis of sugars that they use as food to provide them with energy for millions of years.[3] By using sunlight to power photocatalysts in their cells they are able to fix CO_2 from the atmosphere and convert it sugars. Over the last few decades photolysis, or artificial photosynthesis, has emerged as a promising means of solar energy storage. In this thesis, I will describe how metal oxide materials have emerged as attractive candidates as photocatalysts to power artificial photosynthetic devices.

1.2 Photoelectrochemical Water Splitting as a Means of Solar Energy Storage

In plants, solar energy storage is accomplished via the following chemical reactions:

(Eqn. 1.1) $$6\ H_2O \rightarrow 3\ O_2 + 12\ H^+ + 12\ e^-$$

(Eqn. 1.2) $$6\ CO_2 + 24\ H^+ + 24\ e^- \rightarrow C_6H_{12}O_6 + 6\ H_2O$$

In the oxidation half reaction (1.1), water is oxidized to form O_2, H^+ ions and electrons. In the following step, eq. (1.2), H^+ and electrons are used to reduce CO_2 to a sugar molecule. By capturing CO_2, and breaking apart water, plants can use these solar powered reactions to effectively store energy from the sun.

A variation of this process can be used to store solar energy via photolysis. However, instead of forming sugars using captured CO_2, the H^+ ions themselves can be reduced in the following reaction:

(Eqn. 1.3) $$2\ H^+ + 2e^- \rightarrow H_2$$

By coupling this process with oxygen evolution from water a closed cycle is generated as in Figure 1.3.

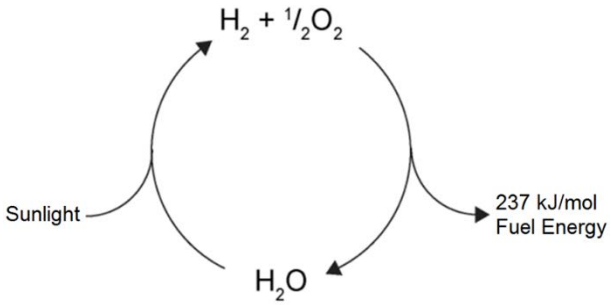

Figure 1.3: Proposed water splitting cycle. Water could be split into H_2 and O_2 using sunlight and a photocatalyst. The H_2 produced could then be collected and used to extract 237 kJ/mol of energy.

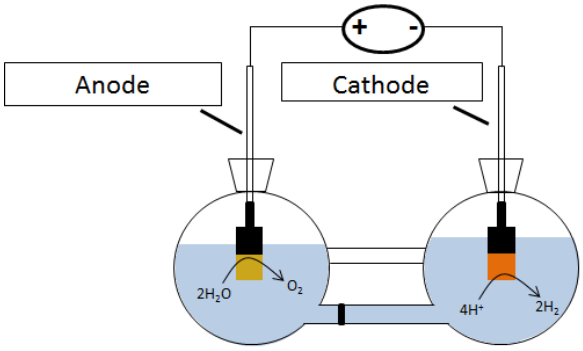

Figure 1.4: Two sided electrochemical water splitting cell. When an electrical bias is applied across the two electrodes the anode will perform water oxidation while the cathode will reduce protons to yield H_2.

It is possible to drive the overall water splitting process using an applied electric field. Figure 1.4 depicts a water splitting electrolysis cell. In this configuration, the water splitting reaction is separated into two separate half reactions which together yield overall water splitting as follows:

(Eqn. 1.4) $2\ H_2O \rightarrow O_2 + 4\ H^+ + 4\ e^-$ $E^o = 1.23$ V vs. NHE

(Eqn. 1.5) $2\ H^+ + 2\ e^- \rightarrow H_2$ $E^o = 0$ V vs. NHE

(Eqn. 1.6) $2\ H_2O \rightarrow O_2 + 2\ H_2$ $E_{cell} = 1.23$ V

It is observed that the minimum potential required to drive this reaction thermodynamically is 1.23 V vs. RHE. Thus, it is predicted that by placing two metal electrodes in an aqueous solution at pH 0 and applying a potential difference across them of 1.23 V, the electrodes should spontaneously carry out OER at the anode and HER at the cathode. However, to date, this has yet to be accomplished.

In reality the thermodynamic potential only describes the difference in energy between the starting material and the final product. Thus it does not take into account the kinetics of the

reaction. In the case of the OER, significant kinetic barriers arise due to the formation of high energy intermediates such as $^{\bullet}OH$ as in the following equation:

(Eqn. 1.7) $H_2O \rightarrow {}^{\bullet}OH + H^+ + e^-$ $E^o = 2.72$ V vs. NHE

It is observed that the E^o for this reaction is significantly higher than that of OER. This is important because it reveals how the formation of high energy species such as $^{\bullet}OH$ presents significant barriers that impede OER. Thus these types of intermediates are hypothesized to be significant contributors to the high overpotentials required to drive OER on an electrode and highlights the need to investigate materials that have the potential to form and stabilize these types of intermediates in order to facilitate OER.

1.3 Semiconducting Oxides for Energy Conversion

Although the basic premise behind artificial photosynthesis is inspired by plants, the real world application of this system is quite abstract from its biological counterpart. Throughout this thesis I will demonstrate that light absorbing semiconducting materials are able to disrupt equilibrium and drive chemical reactions at their surface.

Semiconducting materials can drive chemical reactions using incident radiation due to their possession of bands. These energy bands are formed as the number of discrete atomic orbital energy states increases to approximately 10^{23} and translational symmetry is taken into account as dictated by Bloch theory.[17] Band structure plays an important role in governing the light absorbing and chemical properties of semiconducting materials. In the case of a visible light absorbing metal oxide semiconductors the (often) empty t_{2g} and e_g orbitals of the highly oxidized metal compose the empty conduction band of the semiconductor. This conduction band is analogous to the LUMO of a molecule. The valence band of the semiconductor is analogous to the HOMO of a molecule.[17] In the case of metal oxides it is often composed mainly of the filled 2p orbitals from the O^{2-} ligands. In between the valence and conduction bands is a forbidden energy region in which there are no available energy states that can be occupied. This region is referred to as the band gap, and it is

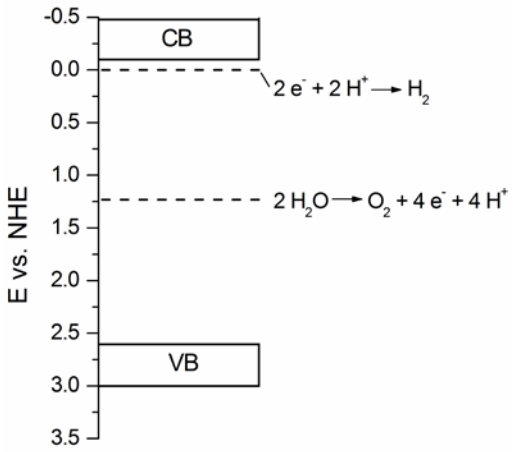

Figure 1.5: Band diagram of a wide band gap metal oxide. CB is the conduction band and VB represents the valence band. Overlaid are the potential for HER and OER.

the width of this gap which determines what portion of the electromagnetic spectrum can excite an electron from the valence band to the conduction band.

Upon illumination with electromagnetic radiation that has an energy $h\nu \geq E_g$ an electron can be excited from the valence band to the conduction band leaving behind a hole (h^+).[18,19] The excited electron can then go on to reduce a species in solution if the redox potential of that species lies at a more positive potential relative to the conduction band potential. Conversely, the hole that remains in the valence band can perform oxidative chemistry on some species in solution if the valence band potential is more positive than the redox couple of the species in solution.[19] Figure 1.5 depicts the band diagram of a wide band gap semiconductor with the HER and OER redox potentials overlaid. In this particular case, once an electron is excited into the conduction band it can then reduce protons in solution. Additionally, the hole that is left behind in the valence band is able to oxidize water to form oxygen.

Metal oxides (MO) are particularly well suited for water oxidation for a number of reasons. First, most MO's such as WO_3, Fe_2O_3, and $CuWO_4$, all contain the metals in their highest oxidation states (W^{6+}, Fe^{3+}, Cu^{2+}). This makes these materials more stable during the highly oxidizing conditions found in OER. Second, many of these materials possess band gaps $2.2\ eV \leq E_g \leq 2.7\ eV$ which improves visible light absorption. Figure. 1.6 depicts the solar radiation at sea level.[20] It is observed that the majority of light coming from the sun has wavelengths within the visible range which highlights the importance of investigating *visible* light absorbing materials to carry out solar

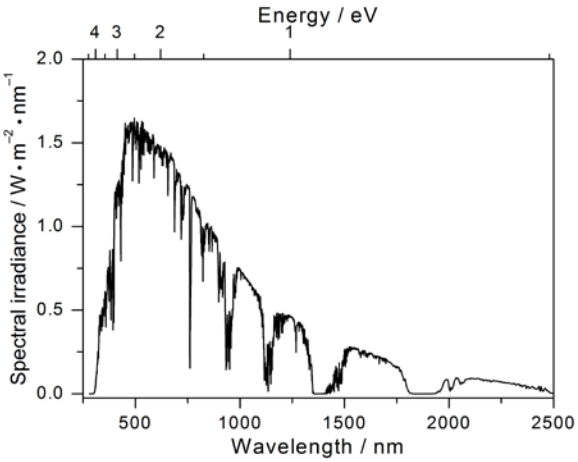

Figure 1.6: Solar radiation spectrum at sea level. The spectrum was constructed using the data from ref. 20.

powered water splitting. Finally, for most MOs the valence band is primarily O 2p in character which situates it at a potential near 3V vs. NHE as depicted in Figure 1.5. Because the VB lies at such an oxidizing potential, this means that holes generated upon photoexcitation will have a significant amount of overpotential to drive water oxidation on the surface. This important aspect allows metal oxides to overcome the kinetic barriers for OER by producing highly reactive species on their surfaces using visible light. Thus, these materials demonstrate a few key properties that make them promising candidates as water oxidation photocatalysts.

1.4 Photoelectrochemical Water Oxidation Using Semiconducting Metal Oxides

In the case of the work presented in this thesis, the metal oxide materials investigated were sought out for use as water oxidation photoanodes. Because the kinetic barriers associated with OER are so great, it is the rate determining step for overall water splitting.[21] As a result, speeding up the kinetics of OER in addition to decreasing the overpotential required to execute this reaction has been a prominent area of research.[3,21,22]

Because many metal oxides are photoactive and their valence bands are very oxidizing, they can carry out OER under illumination. However, because the visible light absorbing oxides often possess insufficiently reducing valence bands they are unable to execute overall water splitting. Although, if an n-type photoanode is coupled with an appropriate p-type photocathode, then a “z-scheme” cell can be constructed that can operate at zero bias and solely run off visible

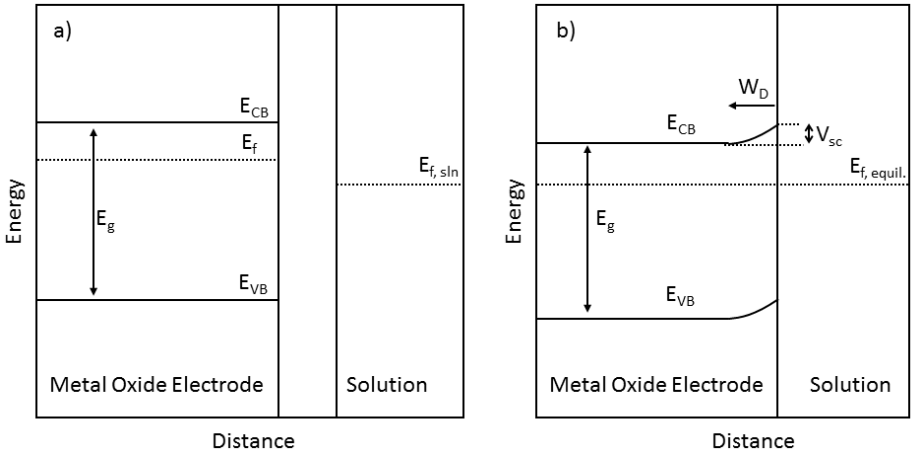

Figure 1.7: The formation of a junction between an n-type semiconductor and an electrolyte solution. a) depicts the separated systems and b) after equilibration.

light.[6] In this configuration, the photoanode executes photocatalyzed OER while the photocathode performs photocatalyzed HER. Because there is no single material that demonstrates all the desired qualities of a photocatalyst (notably visible light absorption and appropriately positioned bands to execute overall water splitting) researchers have focused on developing photoanodes and photocathodes separately.

In the case of many metal oxides, oxygen vacancies in the structure can be produced which result in some fraction of the metal component in the oxide being reduced. The reduced metal functions as a donor impurity whose donor level exists in a state just below the conduction band minimum. This, in turn, raises the Fermi level (E_f). This donor is typically ionized at room temperature, and the extra electron resides in the conduction band.[23] These extra electrons are predominantly responsible for conducting current, and therefore most metal oxide semiconductors are n-type. In an n-type semiconductor, electrons are the majority carrier and holes are considered the minority carrier. The donor density (N_D), or concentration of majority charge carriers (electrons for n-type semiconductors), controls the electrostatics at the electrode/electrolyte interface and is measurable.[19]

When considering n-type semiconducting photoelectrodes, it is important to consider what happens when the electrode is immersed in an electrolyte solution. The electrode/electrolyte interface is described by the same physical quantities that describe a Schottky barrier.[24] When the electrode is submerged in an electrolyte solution, the Fermi levels of the semiconductor and

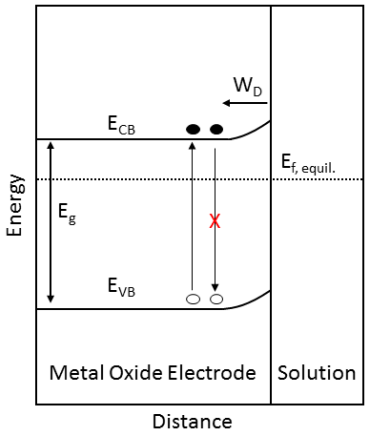

Figure 1.8: Photogeneration of e^-/h^+ pairs in the bulk and depletion layer of an n-type semiconductor. e^-/h^+ pairs are produced due to photon absorption. Photoexcited e^-/h^+ pair formation is demonstrated with an arrow, whereas recombination is expressed as an arrow with a red x.

solution must equilibrate. In other words, the electrochemical potential of the solution and E_f of the semiconductor equilibrate to the same energy. This process is described in Figure 1.7.

Whenever two phases of different electrochemical potentials are brought into contact, the phase that has the more negative electrochemical potential (or E_f) will tend to lose electrons to the phase with the more positive potential. In most cases, E_f of an n-type semiconductor is typically at a higher potential energy than that of the solution. As a result, charge transfer between the solution and electrode will occur until an equilibrium is established. To allow this equilibrium to take place, electrons from the semiconductor must flow into solution, lowering E_f and disrupting the charge neutrality of the semiconductor. This forms a built in voltage (V_{sc}) of the semiconductor which is quantified as the difference in electrostatic potential between the surface of the semiconductor and its bulk.[25] After equilibrium is reached, the surface of the n-type semiconductor has been depleted of majority carriers and is positively charged with respect to the bulk, forming a depletion region. This charge difference produces an electric field, and the N_D dictates the width of the depletion region (W_D).

N-type materials are well suited as photoelectrodes for photoelectrochemical water oxidation since, upon illumination, it is the *minority* charge carriers that are responsible for the chemistry that occurs on the surface. When a semiconductor electrode is irradiated by light with energy greater than the band gap energy of the semiconductor, the electrode absorbs the photon energy to excite electrons from the valence band to the conduction band. This produces

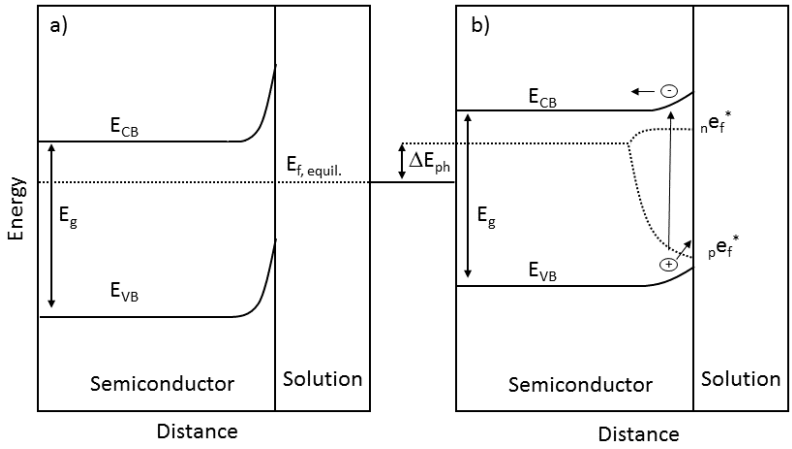

Figure 1.9: Energy diagrams for an n-type semiconductor electrode (a) in the dark and (b) in the photoexcited state: E_{CB} = conduction band edge level; E_{VB} = valence band edge level; E_f = Fermi level in the dark; $_ne_{f*}$ = electron Fermi level after photoexcitation; $_pe_f^*$ = hole Fermi level after photoexcitation.

photoexcited pairs of electrons in the conduction band and holes in the valence band as shown in Figure. 1.8. For n-type semiconductors, the photoexcited electrons hardly influence the concentration of electrons in the conduction band because electrons are the majority charge carriers. However, the photoexcited holes significantly increase the total concentration of holes (minority charge carriers) in the valence band. Generally, in semiconductor electrodes, photoexcitation significantly increases the concentration of minority charge carriers, but barely influences the concentration of majority charge carriers.

In the dark, thermal equilibrium is established between electrons in the conduction band and holes in the valence band so that both the quasi-Fermi level of electrons ($_ne_f^*$) and the quasi-Fermi level of holes ($_pe_f^*$) equal the original Fermi level of the semiconductor (E_f) as depicted in Figure 1.9a. Under the condition of photoexcitation, however, the quasi-Fermi level of electrons and holes split (Figure. 1.9b). In this case, $_ne_f^*$ is slightly higher and $_pe_f^*$ is lower than the original Fermi level of the semiconductor ($_ne_f^* > E_f > {}_pe_f^*$). This split in the Fermi levels provides the driving force to perform chemistry on the surface of the electrode.

As a result, these photoexcited e^-/h^+ pairs create an unequal distribution of charge, disrupting the equilibrium at the semiconductor/electrolyte interface. The formed photovoltage drives a photocurrent. When an n-type semiconductor performs water oxidation, h^+ are driven to the surface to perform OER. The resulting photoexcited e^- can be driven through the external circuit via the back contact to the counter electrode, or sent to a photocathode. In either case, this results in proton reduction at the counter electrode.

1.5 Kinetics of OER on Metal Oxides and the Effects of Competing Side Reactions

The previous section outlined how photo-driven chemical reactions can be conducted on the surface of a semiconducting photoelectrode. However, the descriptions presented described the surface reactions using a purely thermodynamic perspective. In reality, the surface processes that take place on these electrodes are complex and kinetics play a significant role in controlling what reactions dominate on the electrode surface.

Although metal oxides possess valence bands that are sufficiently oxidizing (E_{VB} = ~3 V vs. NHE) to drive OER, it has been frequently demonstrated in the literature[6,26–28] that competing side reactions such as anion oxidation can dominate, despite these reactions having more positive standard electrode potentials (E^o values) versus OER. Using the photoelectrolysis of a NaCl aqueous solution on WO_3 photoelectrodes as a specific example, the oxidation half reaction:

(Eqn. 1.8) $2\ Cl^- \rightarrow Cl_2 + 2\ e^-$ $E^o = 1.36$ V vs. NHE

will dominate on WO_3.[6,27] This is despite the concentration of H_2O being significantly greater than that of Cl^- in aqueous solution. Additionally, the E^o of H_2O/O_2 is 1.23 V vs. NHE, while Cl^-/Cl_2 has an E^o of 1.36 V vs. NHE. If thermodynamics were the dominating factor in dictating the chemistry that occurs on the electrode surface, then OER should dominate instead since the net potential is 1.23 V vs. NHE in addition to the concentration of H_2O being orders of magnitude larger than the dissolved Cl^- since it is the solvent.

However, this is not the case and the observed behavior suggests that Cl^- oxidation dominates primarily for the following reason; since the metal oxide VB is ~3V vs. NHE, a photogenerated hole will have more than enough overpotential to drive either H_2O (via OER) or Cl^- oxidation. In this situation, the hole will preferentially react with the more "kinetically accessible" anion. When considering the kinetics of the two reactions, that is Cl^- oxidation versus OER, a few significant differences emerge. First, Cl^- oxidation is only a 2 e^- oxidation reaction while OER is a 4 e^- process. If e^- removal proceeded through a series of 1 e^- oxidation steps, then OER would require twice as many of these elementary reactions in order to proceed. As a result, this effect contributes to the sluggish kinetics of OER and is proposed to be an important contributing factor towards the low OER Faradaic efficiencies observed on semiconducting metal oxide photoelectrodes such as WO_3.

Furthermore, OER is also a protic reaction. This implies that the 4 electron oxidation must proceed via series of proton coupled electron transfer (PCET) steps.[29,30] Proton involvement in this reaction only serves to further complicate the kinetics since protons must be removed and transferred in addition to electrons in order for OER to proceed. Furthermore, to execute OER the removal of *four* protons is required. This slows the reaction kinetics (i.e., results in a reduced rate constant *k*) since protons are considerably heavier than e^- and thus will be transferred more slowly than electrons.[29,30] By comparison, Cl^- oxidation is a *proton independent* reaction which only requires electron transfer via the oxidation of 2 Cl^- anions with consequent Cl-Cl bond formation to yield Cl_2. This yields more rapid kinetics for Cl^- oxidation relative to OER. Finally, another potential kinetic complication for OER is that as the reaction proceeds, the equilibrium is shifted further to the left (reagents' side) due to the generation of protons (Eqn. 1.4). Thus if protons are not efficiently ferried away from the surface during the course of OER this can dramatically impact kinetics if the local concentration of protons at the electrode surface is allowed to increase significantly.

Throughout this thesis I will explore how competing reactions may interfere with OER. Specifically, in this work I aim to identify the alternate competing mechanisms that will affect the photocurrent of the photoelectrode. In particular, anion oxidation in addition to electrode degradation processes are explored in detail in the hopes of obtaining a better understanding as to how these processes might be reduced or eliminated and how they affect OER.

1.6 Strategies for Developing Semiconducting Metal Oxide Materials

When designing photocatalysts to perform OER using visible light, a few key considerations must be made. First, the material must possess a small band gap and a high absorption coefficient to improve its ability to produce photogenerated charge carriers upon visible light illumination.

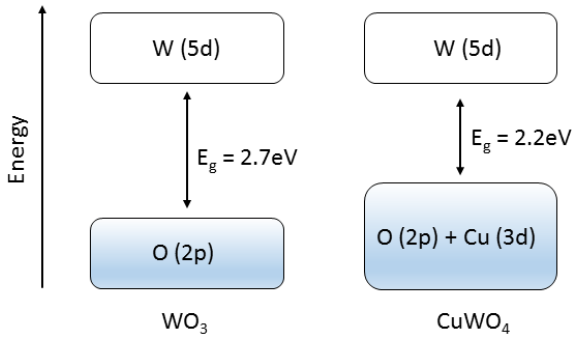

Figure 1.10: Band diagram demonstrating how the band gap of a metal oxide may be reduced by adding a secondary metal cation to form a ternary phase. In this case, Cu is added to WO_3 to form $CuWO_4$. The Cu (3d) orbitals can hybridize with the O 2p which raises the valence band maximum and reduces the band gap.

Second, the material must demonstrate high conductivities for both electrons and holes in order to effectively separate the photogenerated charges and perform the desired chemistry on the surface. Third, the catalyst must demonstrate a high degree of selectivity in addition to a high turnover frequency for the desired reaction. Finally, the material in question should be photoelectrochemically stable.

With these motivations in mind, this thesis focuses on exploring how these different attributes can be promoted in metal oxide materials. One strategy to form visible light absorbing oxides is to form ternary phases (ABO_x) whose valence band maximum is not predominantly comprised of O 2p orbitals. In this case, the valence band will often consist of a mix of metal based orbitals hybridized with O 2p. If the ternary phase is selected carefully, this can have the effect of reducing the band gap without adding inter band gap states that could lead to charge recombination. This effect is demonstrate in Figure 1.10.

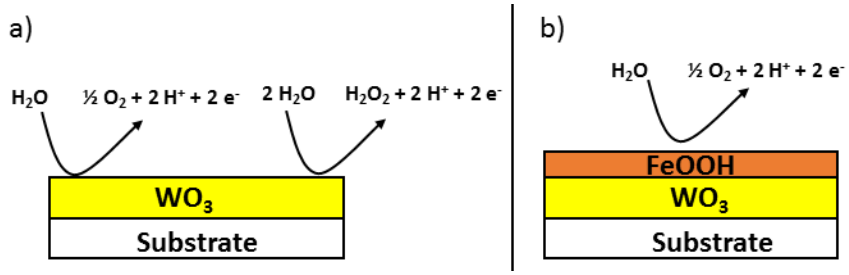

Figure 1.11: a) a WO_3 electrode without an electrocatalytic surface layer. In this configuration a variety of reactions can take place on the surface which can degrade the WO_3 and decrease its Faradaic efficiency. b) WO_3 coated with a protective FeOOH catalyst. The presence of the FeOOH improves selectivity and stability of the electrode by only allowing OER to take place on the surface due to its high selectivity for this reaction.

The most important requirement in forming a ternary phase semiconductor is that the M(s/d) orbitals must be sufficiently electronegative to effectively hybridize with the oxygen based orbitals in the band structure. This improves orbital overlap which can result in improved charge mobility across the material. Most ternary phase semiconducting oxides are derived from oxyanions (BO_x^{n-}) in which the empty valence orbitals of the d^0/d^{10} metal component (B) form the conduction band. The valence band is typically formed from filled, or nearly filled, s or d orbitals of the metal cation (A^{m+}) component of the ternary phase that hybridize with O 2p orbitals from the O^{2-} ligands. The selection of metal cations with either full (d^{10}) or empty (d^0) d shells is particularly important since this can impact the recombination rate and conductivity of the resulting material.[31] One example of a d^0/d^{10} ternary metal oxides that shows significant promise is $BiVO_4$. The Bi(6s) orbitals dominate the valence band maximum, forming a 2.5 eV band gap material.[10,32]

Selectivity and turnover frequency of materials can also be manipulated. One potential strategy is the coupling of an electrocatalyst with a photoelectrode. In this configuration, the catalysis and photogeneration of charge carriers are separated since the catalysis is now shifted entirely to the surface layer as demonstrated in Figure 1.11. e^-/h^+ pairs can be generated within the light absorber under illumination and, in the case of n-type semiconductors, the photogenerated holes can then be transferred to the electrocatalyst so that it can perform OER. This strategy has been proven to be effective at increasing the turn over frequency for OER in addition to providing a means of protecting unstable semiconducting surfaces which allows them to perform photoelectrochemical OER for extended periods of time.[5,28,33,34]

Finally the stability of the resulting metal oxide is crucial to its success as a photoanode. It is important to select materials that do not undergo adverse side reactions which can lead to their degradation. An example of an unstable semiconducting material is CdS. Although it is an n-type semiconductor with a small band gap of 2.4 eV, it has been demonstrated to be very unstable when performing OER photoelectrochemically in aqueous solution.[35] Instead of performing OER the following side reaction dominates:

(Eqn. 1.9) $$CdS + 4\,h^+ + 2\,H_2O + O_2 \rightarrow Cd^{2+} + SO_4^{2-} + 4\,H^+$$

This example highlights the importance of developing materials that are stable during the highly oxidizing conditions of photoelectrochemical water oxidation. In particular, it is important

to develop metal oxide materials that are unable to undergo side reactions that could lead to their degradation. Thus it is critical to select materials that are composed only of metals in their highest or most stable oxidation states to reduce the chances of adverse side reactions occurring.

1.7 Scope of this Thesis

This thesis is structured around obtaining a more profound understanding of *how* semiconducting metal oxides conduct water oxidation in addition to determining *which* aspects of photocatalysis (light absorption, kinetics, carrier recombination) are most important when driving water oxidation. As a result, this thesis adopts a more kinetic oriented approach to the chemistry of this diverse class of materials. Particular attention is devoted to competing side reactions such as anion oxidation (with WO_3) or detrimental electrode self-oxidation (with $PbCrO_4$). In chapter 2 the effects of the growth of an electrocatalytic FeOOH on the selectivity and rate of OER on WO_3 electrodes is explored. Furthermore, it is demonstrated that this layer also serves to greatly enhance the stability of the resulting electrode which allows its use at higher pH values ($pH \leq 7$). In chapter 3 the kinetics of OER on WO_3 are further explored using a novel rotating ring disk technique. Particular attention is paid to developing an understanding of why WO_3 electrodes demonstrate photocurrent losses even at lower pH values where they are thermodynamically stable. With RRDPE experiments it is observed that only a minor amount of peroxo species (in the form of persulfate and peroxophophate) are produced during photoelectrochemical OER on WO_3 electrodes in 1N acidic solution of H_2SO_4 and H_3PO_4. Furthermore, it is discovered that a reversible electrode oxidation reaction, which is most likely a result of WO_3's inherent electrochromism, is responsible for this photocurrent loss. In Chapter 4 the kinetics of OER on the ternary phase metal oxide, $CuWO_4$ are explored. It is observed that the kinetics of PEC OER on $CuWO_4$ are slow which is exhibited by large Tafel slopes. Furthermore, the reaction is zeroth order in borate electrolyte which indicates that the anion in that system is non-participating in the rate determining step of OER. Improvements in the kinetics of OER on $CuWO_4$ were explored via Co doping. It was observed that $Cu_{1-x}Co_xWO_4$ thin film solid solutions could be easily produced using a simple spray pyrolysis procedure. However, the incorporation of Co appears to dramatically increase charge recombination which results in lower photocurrents. Finally chapter 5 explores the synthesis and characterization of the novel ternary metal oxide, $PbCrO_4$. This material, being composed only of metals with completely empty or filled d-shells, demonstrates a high absorption

coefficient in addition to a small band gap which makes it a promising candidate for PEC OER. However, it is observed in aqueous solution that a passivation reaction dominates which shuts off reactivity when electrodes of this material are subjected to an applied electric field under illumination. This results in the formation of a surface passivating PbO_2 layer with consequent removal of Cr^{6+} most likely as water soluble CrO_4^{2-} species from the electrode surface. On the other hand, catalytic activity can be restored upon reannealing and the electrodes demonstrate improved stability when performing organic oxidation reactions which suggests that they are more suitable for that type of chemistry. Finally, it is demonstrated that the novel chelation synthesis that was developed to synthesize thin films of $PbCrO_4$ can be expanded towards the synthesis of other highly active and aqueous stable photocatalysts such as $BiVO_4$. Following the thesis, there are appendices containing supporting data pertinent to each chapter. They are separated by chapter and appendix A-C is each for Chapters 2, 3 and 5, respectively. The appendix figures are referenced throughout each chapter.

1.8 References

(1) Chen, L.; Shet, S.; Tang, H.; Ahn, K.; Wang, H.; Yan, Y.; Turner, J.; Al-Jassim, M. *J. Appl. Phys.* **2010**, *108* (4), 43502.
(2) Turner, J. A. **1999**, *285* (5428), 687.
(3) Lewis, N. S.; Nocera, D. G. *Proc. Natl. Acad. Sci. U. S. A.* **2006**, *103* (43), 15729.
(4) Ding, C.; Qin, W.; Wang, N.; Liu, G.; Wang, Z.; Yan, P.; Shi, J.; Li, C. *Phys. Chem. Chem. Phys.* **2014**, *16* (29), 15608.
(5) Seabold, J. A.; Choi, K. *Chem. Mater.* **2011**, *23* (5), 1105.
(6) Hill, J. C.; Choi, K. *J. Phys. Chem. C* **2012**, *116* (14), 7612.
(7) Pilli, S. K.; Deutsch, T. G.; Furtak, T. E.; Brown, L. D.; Turner, J. A.; Herring, A. M. *Phys. Chem. Chem. Phys.* **2013**, *15* (9), 3273.
(8) Valenti, M.; Dolat, D.; Biskos, G.; Schmidt-Ott, A.; Smith, W. a. *J. Phys. Chem. C* **2015**, *119* (4), 2096.
(9) Reece, S. Y.; Hamel, J. A.; Sung, K.; Jarvi, T. D.; Esswein, A. J.; Pijpers, J. J. H.; Nocera, D. G. *Science.* **2011**, *334* (6056), 645.
(10) Park, Y.; McDonald, K. J.; Choi, K.-S. *Chem. Soc. Rev.* **2013**, 2321.
(11) Centi, G.; Perathoner, S. *ChemSusChem* **2010**, *3* (2), 195.
(12) Herron, J. A.; Kim, J.; Upadhye, A. A.; Huber, G. W.; Maravelias, C. T. *Energy Environ. Sci.* **2015**, *8*, 126.
(13) Sivula, K.; Le Formal, F.; Grätzel, M. *ChemSusChem* **2011**, *4* (4), 432.
(14) Roberts, B. J. Photovoltaic Solar Resources of the United States http://www.nrel.gov/gis/solar.html (accessed Nov 26, 2016).
(15) *Fast Facts: What the Duck Curve Tells Us About Managing a Green Grid*; 2016.
(16) Cook, T. R.; Dogutan, D. K.; Reece, S. Y.; Surendranath, Y.; Teets, T. S.; Nocera, D. G. *Chem. Rev.* **2010**, *110* (11), 6474.
(17) Hoffmann, R. *Solids and Surfaces: A Chemist's View of Bonding in Extended Structures*; 1988.
(18) Rajeshwar, K. **1990**.
(19) Norio Sato. *Electrochemistry at Metal and Semiconductor Electrodes*, First Edit.; Elsevier:

Amsterdam, **1998**.
(20) NREL. Reference Solar Spectral Irradiance: ASTM G-173 http://rredc.nrel.gov/solar/spectra/am1.5/astmg173/astmg173.html (accessed Jan 23, 2016).
(21) Bediako, D. K.; Surendranath, Y.; Nocera, D. G. *J. Am. Chem. Soc.* **2013**, *135* (9), 3662.
(22) Nocera, D. G. *Acc. Chem. Res.* **2012**, *45* (5), 767.
(23) Dmochowski, J. E. *J. Phys. Conf. Ser.* **2007**, *79*, 12010.
(24) Gerischer, H. *J. Electroanal. Chem. Interfacial Electrochem.* **1975**, *58* (1), 263.
(25) Bisquert, J.; Cendula, P.; Bertoluzzi, L.; Gimenez, S. *J. Phys. Chem. Lett.* **2014**, *5* (1), 205.
(26) Mi, Q.; Coridan, R. H.; Brunschwig, B. S.; Gray, H. B.; Lewis, N. S. *Energy Environ. Sci.* **2013**, *6* (9), 2646.
(27) Mi, Q.; Zhanaidarova, A.; Brunschwig, B. S.; Gray, H. B.; Lewis, N. S. *Energy Environ. Sci.* **2012**, *5* (2), 5694.
(28) Lhermitte, C. R.; Verwer, J. G.; Bartlett, B. M. *J. Mater. Chem. A* **2016**, *4*, 2960.
(29) Cukier, R. I.; Nocera, D. G. *Annu. Rev. Phys. Chem.* **1998**, *49*, 337.
(30) Solis, B. H.; Hammes-Schiffer, S. *Inorgani* **2014**, *53*, 6427.
(31) Lhermitte, C. R.; Bartlett, B. M. *Acc. Chem. Res.* **2016**, *49* (6), 1121.
(32) Martinez Suarez, C.; Hernández, S.; Russo, N. *Appl. Catal. A: Gen.* **2015**, 504, 158.
(33) Pilli, S. K.; Deutsch, T. G.; Furtak, T. E.; Turner, J. a.; Brown, L. D.; Herring, A. M. *Phys. Chem. Chem. Phys.* **2012**, *14* (19), 7032.
(34) Abdi, F. F.; Firet, N.; van de Krol, R. *ChemCatChem* **2013**, *5* (2), 490.
(35) Meissner, D.; Memming, R.; Kastening, B. *J. Phys. Chem.* **1988**, *92* (12), 3476.

CHAPTER 2

Improving the Stability and Selectivity for the Oxygen-Evolution Reaction on Semiconducting WO_3 Photoelectrodes with a Solid-State FeOOH Catalyst

Portions of this chapter have been published:
Lhermitte, C. R., Verwer, J. G., Bartlett, B. M., *J. Mat. Chem. A*, **2016**, 4, 2960. Reproduced by permission of the Royal Chemical Society.

2.1 Introduction

The primary research goal of this thesis was to obtain a better understanding of how metal oxide materials behave as photoanodes for water oxidation. As a result a large portion of this work is dedicated to learning more about the kinetics of water oxidation on these surfaces in addition to any detrimental degradation processes that may take place concurrently. WO_3 was selected as an ideal model for study due to its small band gap (2.7 eV, 460 nm), high Hall mobility (10 $cm^2 \bullet V^{-1}s^{-1}$) and long minority-carrier diffusion length (0.3-4.2 μm).[1,2] However, this material suffers from poor selectivity for OER in addition to poor stability in non-acidic aqueous solutions (pH > 4). This is despite the fact that it is predicted to be thermodynamically stable when used as a photoanode for water oxidation (OER) due to its anodic decomposition potential being located 1.1 V more positive than the OER potential.[3]

It has been observed that WO_3 gradually loses its catalytic performance over time when used as a photoanode for water oxidation. This effect is exacerbated at higher pH values. The source of this degradation is two-fold; first WO_3 can behave as an Arrhenius acid, which reduces its stability in more basic solutions since it has the potential to undergo acid-base reactions with OH^- in solution.[4,5,6] Additionally, it is proposed that during the course of PEC OER, WO_3 produces and accumulates peroxo- species on its surface, which can accelerate its degradation.[3,7] These two effects are suspected to be the cause of the decrease in stability and Faradaic efficiency for OER on WO_3 with increasing alkaline pH.

We sought to develop a solution to stabilize the surface of WO_3. It was determined that the growth of an oxygen evolution (OEC) catalyst on the surface might effectively protect the WO_3 surface. This strategy has been previously demonstrated to work with cobalt phosphate (CoP_i) and nickel borate (NiB_i) OECs on WO_3 and $BiVO_4$ photoanodes.[3,8]

Recently, it has been shown that electrochemically grown NiOOH and FeOOH films are effective catalysts for OER.[9–14] However, the coupling of these particular OECs to the surface of a light- absorbing metal oxide has been limited to $BiVO_4$ and Fe_2O_3.[8,15,16] Ni and Fe based oxyhydroxides are ideal candidates for use as co-catalysts on WO_3 due to the simplicity of their syntheses and the earth abundance of their constituent elements. Although NiOOH demonstrates higher activity,[10,11] the more basic and reductive growth conditions were incompatible with the WO_3 electrodes. However, FeOOH can be grown under oxidative conditions at a low pH (~4).[8] These growth conditions coupled with the hardiness of this material made it an attractive candidate to couple with WO_3 as an OER co-catalyst.

2.2 Sol-Gel Synthesis and Characterization of WO_3 Photoelectrodes

WO_3 electrodes were synthesized via a sol-gel method. By spin coating a tungstic acid colloid that was produced by running a sodium tungstate solution through an ion exchange column and repeatedly annealing at 500°C after each layer, WO_3 electrodes with a glassy greenish appearance were obtained. XRD data (Figure. A.1) reveal that the films are phase pure monoclinic WO_3 and SEM images (Figure. 2.1) show that the films appear to be dense and homogeneous in texture. The cross-sectional SEM image indicate that the films are ~2 μm thick and comprised of interconnected nanoparticles with some porosity.

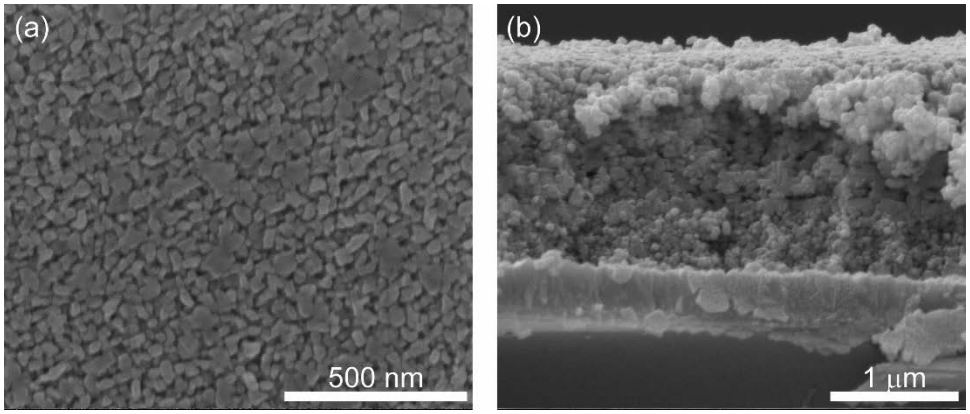

Figure 2.1: a) Top-down SEM image of a WO_3 photoanode, b) cross-section of a WO_3 photoanode.

WO_3 is known to display poor stability in higher pH aqueous solutions.[4] To gain more insight concerning the degradation of the WO_3 electrodes, representative samples were left to soak overnight without stirring in pH 4 and pH 7 KP_i solutions. After the overnight soak, the morphology of the electrode left in the pH 4 solution appeared unchanged via SEM. On the other hand, there was a visible amount of WO_3 removed from the electrode soaked in the pH 7 solution. These SEM images (Figure. 2.2) reveal that the WO_3 soaked in the pH 7 solution had eroded significantly, most likely due to the aqueous acid-base reaction[4]:

(Eqn. 2.1) $$WO_3\,(s) + H_2O\,(l) \rightarrow 2H^+\,(aq) + WO_4^{2-}\,(aq)$$

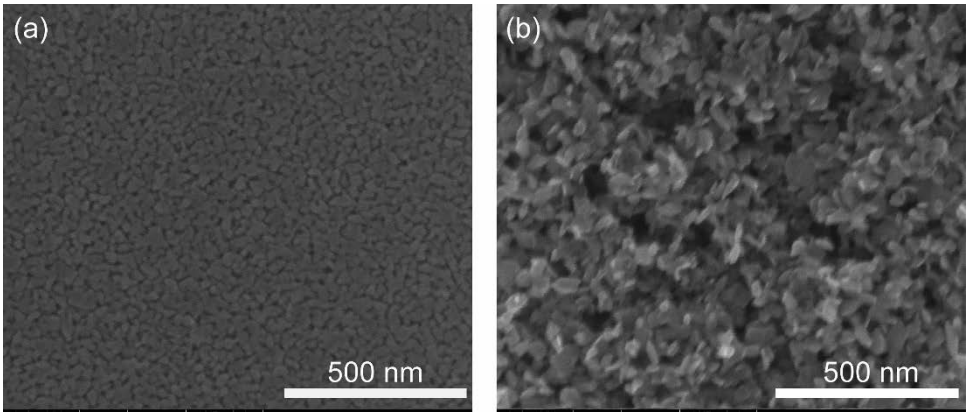

Figure 2.2: SEM images of WO_3 electrodes soaked in a) pH 4 and b) pH 7 KP_i buffered solutions overnight.

As for the electrode soaked in the pH 4 solution, the material does not appear to have degraded significantly via SEM imaging. Furthermore, chopped light linear sweep voltammograms (CL-LSVs) of the two films were collected in pH 4 KP_i before and after soaking the films overnight in their respective solutions (Figure. A.2). The WO_3 electrode soaked in the pH 7 KP_i demonstrate a 95% (0.038 mA/cm^2 vs 0.808 mA/cm^2) loss in saturated photocurrent. On the other hand, the electrode soaked in the pH 4 KP_i electrode surprisingly displays a 9.7% (0.947 mA/cm^2 vs. 0.863 mA/cm^2) *increase* in saturated photocurrent. The observed increase may simply be due to the overnight soaking acting as a pre-treatment which may render the WO_3 surface more catalytically active. This is supported by the concurrent increase in electrocatalytic current in the CL-LSV. The importance of pre-treatments in increasing catalytic activity has been previously reported with other materials.[11,12,17] These results indicate that acid base interactions in the 0.1 M

pH 4 KP_i solution is not the primary cause for the observed degradation in photocurrent during controlled potential coulometry (CPC or bulk electrolysis).

2.3 Deposition of a FeOOH Electrocatalyst onto WO_3

To improve the stability and Faradaic efficiency for OER of the sol-gel WO_3 photoanode, a solid state FeOOH electrocatalyst was deposited on its surface. The growth of the FeOOH film was accomplished by combining a photoelectrochemical (PEC) deposition followed by an electrochemical (EC) deposition in a 0.1 M $FeCl_2$ solution. This procedure was adapted from one previously published to deposit FeOOH onto $BiVO_4$.[12] It was observed that preceding an EC step with a short PEC deposition appeared to increase the rate of film growth for the EC deposition that followed. Thus it was hypothesized that the PEC deposition served to generate nucleation sites nearest to where the electron-hole pairs are generated under illumination, which would then allow more rapid film growth during the EC deposition step. Unless specified otherwise, after the FeOOH film was grown, the electrodes were immediately used (within minutes) in the following experiments. This prevented cracks from forming due to dehydration of the electrode (Figure. A.3).

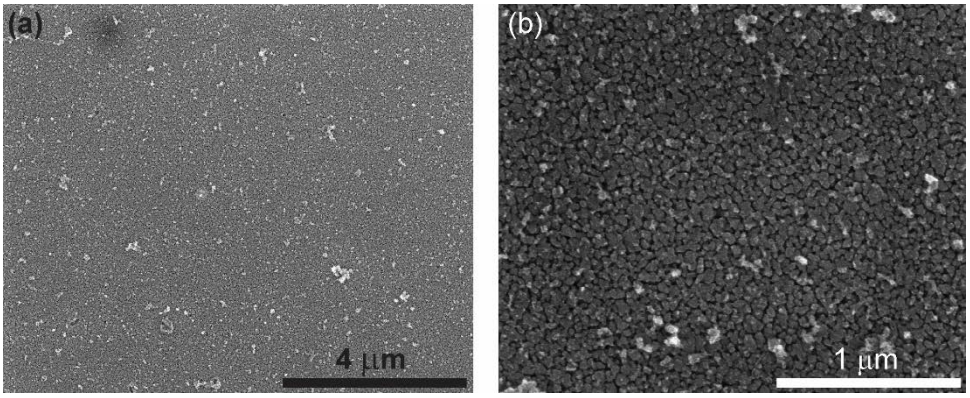

Figure 2.3: SEM images of WO_3-FeOOH at a) 25K magnification and b) 100K magnification.

After FeOOH deposition, the morphology of the resulting films do not appear significantly altered via SEM imaging (Figure 2.3). Rather, small islands of FeOOH form on the surface of the WO_3. It must be noted that the WO_3 films appear somewhat porous, so it is possible that there may be FeOOH deposited in the interstices of the film, which may not be easily viewed via SEM. The FeOOH itself appears to be amorphous, displaying no distinct Bragg reflections in its XRD pattern (Figure. A.4). Nevertheless, the presence

of Fe on the surface of the WO_3 was confirmed via EDX spectroscopy (Figure. A.5). In addition, the onset of electrocatalytic current in CL-LSVs shifts to much lower overpotentials, indicating the presence of the OEC on the WO_3 surface (Figure. 2.4).

2.4 Electrochemistry of WO_3-FeOOH Electrodes

The growth of FeOOH on WO_3 decreases the saturated photocurrent by 48 – 50%, from ~0.8 to ~0.4 mA•cm^{-2} for an average film (Figure. 2.4). However, because the measured current density is a sum of all current derived from the electrochemical reactions occurring at the surface, this means that not all the current generated is from the desired OER in the case of the bare WO_3 electrodes. We note that another possible cause of the decrease in the

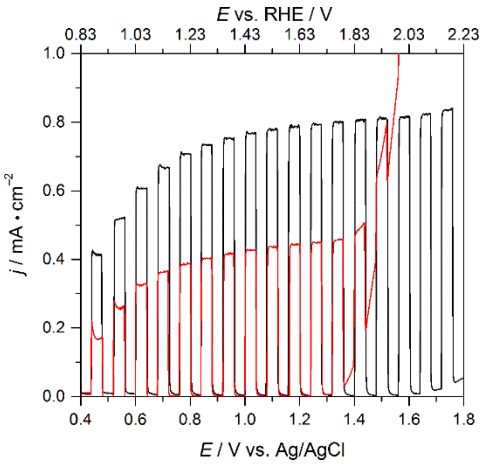

Figure 2.4: Chopped Light linear sweep voltammograms (CL-LSVs) of a WO_3 electrode before (black) and after the growth of an FeOOH OEC (red) in pH 4 KP_i buffered solution under 1 sun AM1.5G illumination.

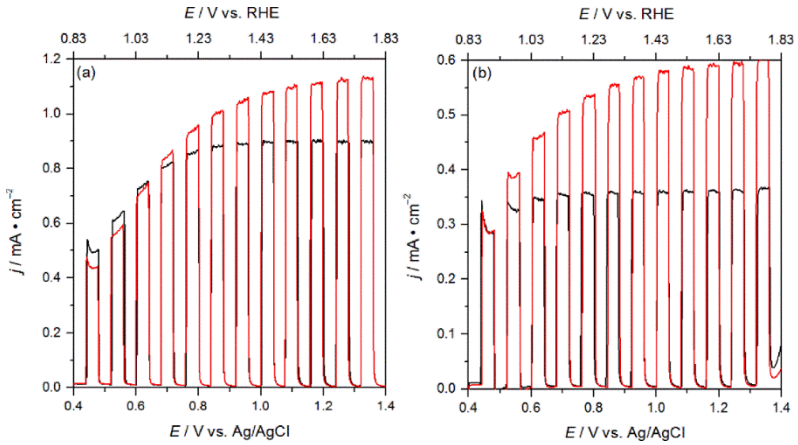

Figure. 2.5: CL-LSVs for a) WO_3 and b) FeOOH recorded in 0.1 M KP_i buffer at pH 4 under 100 mW/cm^2 AM1.5G illumination. The sweep rate is 20 mV/s. Data in black represent voltammograms recorded under front-side illumination, and data in red under back-side illumination.

measured photocurrent density may be due to competitive light absorption from the FeOOH. The UV-vis absorption spectra (vide infra, Figure. A.6) indicate that the FeOOH does indeed absorb visible light (λ_{max} of 425 nm), so it may compete with WO_3 for light absorption. Furthermore, CL-LSVs with FeOOH grown on FTO (Figure. A.7) demonstrate that any light absorbed by the FeOOH does not contribute to the photoresponse of the WO_3-FeOOH system, thus any current generated is solely due to electron-hole pairs generated within the WO_3. To better evaluate how competitive absorption from the FeOOH layer might affect electrode behavior, CL-LSVs with front (electrode /electrolyte) and back (substrate/electrode) illumination were collected (Figure. 2.5). Upon front-side illumination, the WO_3-FeOOH electrode displays saturated photocurrent densities of 0.35 mA•cm^{-2}. However, upon back-side illumination, the current does indeed increase by 71% or from 0.35 to 0.6 mA•cm^{-2}. Although an increase in the saturated current density is observed upon back illumination, it is still possible that the FeOOH functions as a co-incorporated layer, and thus still provides parasitic absorption. In order to reduce this effect, all PEC experiments reported herein are conducted with back illumination unless specified otherwise.

2.5 Faradaic Efficiency and Stability of WO_3-FeOOH Electrodes

The Faradaic efficiency for OER on the FTO|WO_3|FeOOH hybrid electrodes (hereafter denoted as WO_3-FeOOH) was evaluated by measuring the O_2 produced with a commercial fluorescence probe during a CPC experiment. These O_2-probe measurements were conducted under 200 mW•cm^{-2} AM1.5G illumination (2-suns) at 1.43 V vs. RHE in a pH 4 KP_i solution in order to generate enough O_2 to obtain sufficient accuracy. To determine the maximum quantity of O_2 that could be generated from water photoelectrochemically, the charge passed after 3.5 hours was converted to μmols O_2 using the following equation:

(Eqn. 2.2)
$$O_2\ (\mu mols) = \frac{Charge\ Passed\ (C) \times 10^6 (\frac{\mu mol\ O_2}{mol\ O_2})}{4(\frac{mol\ e^-}{mol\ O_2}) \times 96485 (\frac{C}{mol\ e^-})}$$

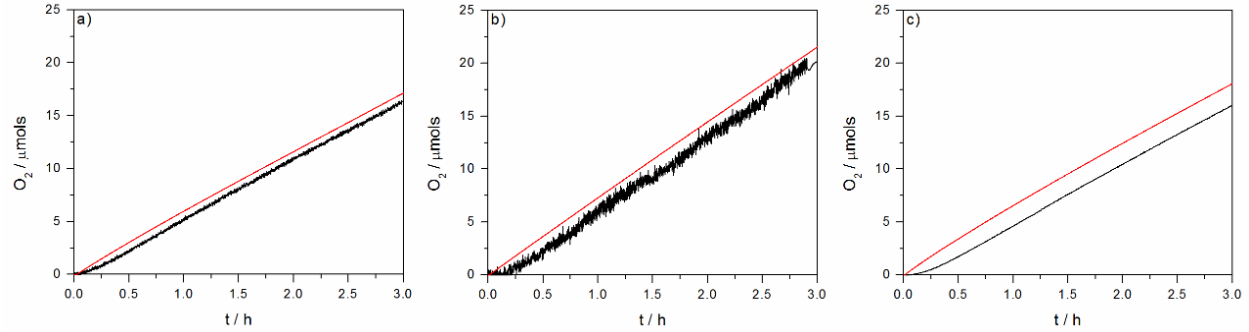

Figure. 2.6: Three trials of oxygen-evolution Faradaic efficiency measurements on WO_3-FeOOH recorded at 1.43 V vs. RHE in 0.1 M KP_i buffer at pH 4 under 200 mW/cm^2 AM1.5G illumination. The red lines represent the theoretical yield of O_2 based on the charge passed, and the black lines indicate the O_2 measured by the Neofox O_2 fluorescence probe. For each experiment, a fresh WO_3-FeOOH electrode was employed. From left to right, the Faradaic efficiencies are 95.6, 97.7, and 94.5% respectively.

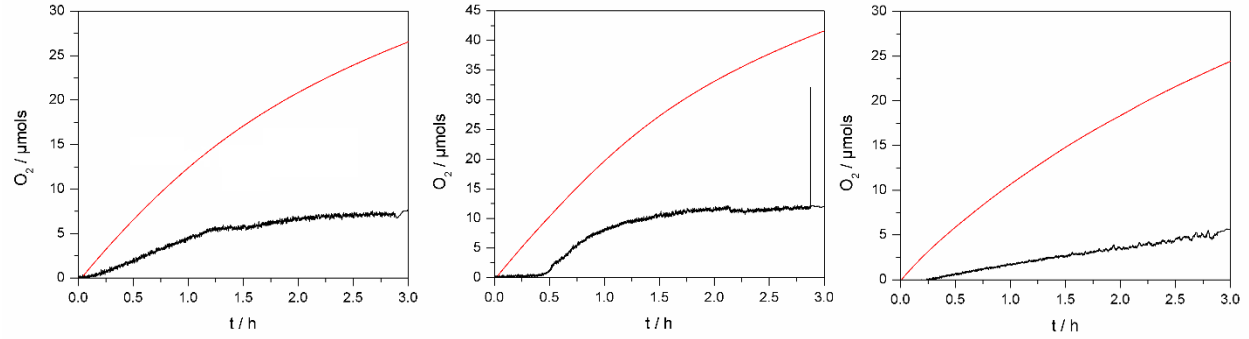

Figure. 2.7: Three trials of oxygen-evolution Faradaic efficiency measurements on WO_3 recorded at 1.43 V vs. RHE in 0.1 M KP_i buffer at pH 4 under 200 mW/cm^2 AM1.5G illumination. The red lines represent the theoretical yield of O_2 based on the charge passed, and the black lines indicate the O_2 measured by the Neofox O_2 fluorescence probe. For each experiment, a fresh WO_3 electrode was employed. From left to right, the Faradaic efficiencies are 28.7, 28.8, and 23.1% respectively.

The Faradaic efficiency is then computed by dividing the O_2 measured after 3.5 hours by the maximum possible quantity of O_2 then multiplying by 100. The O_2 measured after 3.5 hours was used to calculate the Faradaic efficiency because large amounts of bubbles stick to the reference electrode and the sides of the cell after the lamp was turned off even with vigorous stirring, which causes the O_2 signal to continue rising as O_2 was being driven off. The signal typically stabilizes within 30 minutes of the light being turned off. The Faradaic efficiency for OER on WO_3-FeOOH hybrid electrodes is 95.9 ± 1.6%, averaged over three trials. Figure. 2.6 depicts three trials of O_2 Faradaic Efficiency measurements for a WO_3-

FeOOH electrodes in a 0.1 M pH 4 KP_i solution. In contrast, the bare WO_3 electrodes demonstrated an average Faradaic efficiency for OER of 26.8 ± 3.2% over three trials (Figure. 2.7) which agrees well with previously published work.[18] Thus the WO_3-FeOOH electrodes display an increase of ~70% in Faradaic Efficiency for OER over bare WO_3.

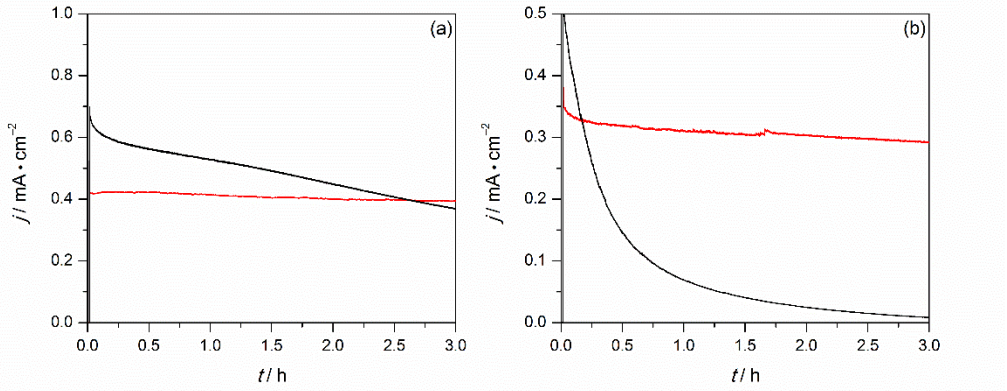

Figure 2.8: CPC curves of WO_3 (black) and WO_3-FeOOH (red) at 1.23V vs. RHE and 1-sun illumination in a) pH 4 and b) pH 7 0.1M KP_i solutions.

In addition to the Faradaic efficiency, we evaluated the stability of the hybrid electrode in aqueous KP_i solutions. For these experiments, CPC at 1.23 V vs. RHE under 1-sun illumination was conducted for 3 hours in pH 4 and in pH 7 KP_i buffered solutions (Figure 2.8). In the pH 4 solution, the WO_3 electrode gradually produces less photocurrent, decaying from 0.70 to 0.37 $mA \cdot cm^{-2}$, indicating that the electrode is undergoing photodegradation. On the other hand, the WO_3-FeOOH electrode displays a stable photoelectrolysis curve over the three hours with its final current of 0.39 $mA \cdot cm^{-2}$ surpassing that of WO_3. Additionally, when the pH of the solution is increased to 7, the WO_3 electrode undergoes rapid degradation in which it loses ~70% of its photocurrent in 30 minutes. However, the WO_3-FeOOH electrode displays a much more stable electrolysis curve during that time period, losing less than 20% of the initial current density (from 0.35 to 0.29 $mA \cdot cm^{-2}$). Finally, by the end of the experiment, the control film was completely removed from the surface of the electrode while the WO_3-FeOOH electrode appeared unchanged.

Furthermore, the chemical stability of WO_3-FeOOH electrodes was probed by soaking them in aqueous KP_i solutions at pH 4 and 7 overnight. CL-LSVs collected in pH 4 buffer both before and after the soaking (Figure. A.8) indicate that no chemical degradation

occurred in either pH, and thus the FeOOH is able to function as a true protective layer. This behavior is in stark contrast to control WO_3 electrodes which degraded significantly—losing as much as 90% of the photocurrent after having been soaked in a pH 7 KP_i solution overnight.

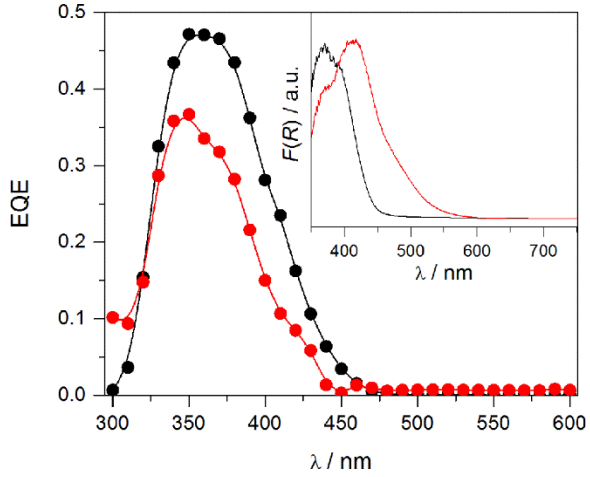

Figure. 2.9: EQE of WO_3 (black) and WO_3-FeOOH (red) at 1.23V vs. RHE in a 0.1M pH 4 KP_i buffered solution with a light chopping frequency of 20 Hz. Inset: absorption spectrum of a WO_3 film before (black) and after (red) growing an FeOOH catalyst on the surface.

The external quantum efficiencies (EQE) and UV-Vis spectra for WO_3 and WO_3-FeOOH electrodes are compared in Figure. 2.9. When back illuminated, the WO_3 electrodes display EQE values of 45 – 47% in the wavelength range 350 – 400 nm. Toward longer wavelengths, the EQE decreases, which is reflective of WO_3's indirect band gap (Eg = 2.7 eV or 459 nm). Once the FeOOH is added, the EQE decreases by about 10% in the region of 350 – 400 nm. The source of this may be threefold. First, the growth of the OEC layer on top of the WO_3 introduces a new heterojunction that could behave as a recombination center for electrons and holes.[19] Secondly, it is known that WO_3 displays relatively low Faradaic efficiency for OER and thus it will readily oxidize other species in solution.[18,20,21] Thus, adding a selective OEC layer on the surface will block these side reactions from occurring, which could account for the lower measured current. Finally, the FeOOH may be behaving as a competitive light absorber, which would reduce the amount of photons reaching the WO_3.

Additionally, the possibility of transient incorporation into the EQE data was examined since this transient photocurrent can lead to inflated values. For this experiment, the EQE

of a single WO_3 film was measured at 15 and 20 Hz light chopping frequencies before and after loading the FeOOH (Figure. A.9). We observed an increase in EQE with decreasing chopping frequency for both the WO_3 and the WO_3-FeOOH case. This result indicates that transient incorporation into the data at 20 Hz is not significant. Furthermore, we attribute the observed increase in EQE with decreasing chopping frequency to a slow photocurrent response time of the electrode either due to slow kinetics for OER on the surface (i.e. the time constant for the reaction is longer than the chopping frequency), or due to slow carrier mobility within the electrode. This type of behavior has been observed in similar systems such as DSSCs which also rely on a chemical redox event to supply current.[22] However, at both chopping frequencies, a decrease in EQE was still observed upon the growth of the FeOOH, which further supports the notion that FeOOH may be competitively absorbing light.

2.6 Discussion

As an electrocatalyst, FeOOH is known to evolve oxygen from water at moderate overpotentials of ~ 300 mV, but it has not been investigated as thoroughly as its Co and Ni counterparts.[23,24] Furthermore, examples of coupling the FeOOH OEC with a semiconducting metal oxide light absorber are limited, and only one such case using $BiVO_4$ has been reported so far.[8] Thus, we desired to measure how the growth of this co-catalyst influences electrode stability and Faradaic efficiency for OER. We hypothesized that by depositing the FeOOH oxygen evolution catalyst on the surface of WO_3, we would shift the OER to FeOOH sites rather than WO_3 sites, which in turn, would protect the WO_3 surface from high energy intermediates formed during the reaction and block its contact with the aqueous electrolyte. Fabricating such an electrode is attractive due to the simplicity of the synthesis and the earth abundance of the materials used. Because WO_3 is a binary metal oxide that can be prepared by simple sol-gel processing, we expect few impurities in the synthesis. Using an Earth abundant Fe-based OEC as opposed to more expensive IrO_x and Ru-based catalysts also enhances the feasibility of using these electrodes in an actual PEC cell.

We relay a simple sol-gel synthesis coupled with a photoelectrodeposition to yield WO_3-FeOOH electrodes. These techniques were targeted due to the known high performance

and the desired reproducibility in the data recorded on the generated films. Electrodes synthesized using these techniques demonstrated a high degree of consistency, which facilitated the collection of three trials for each Faradaic efficiency measurement to

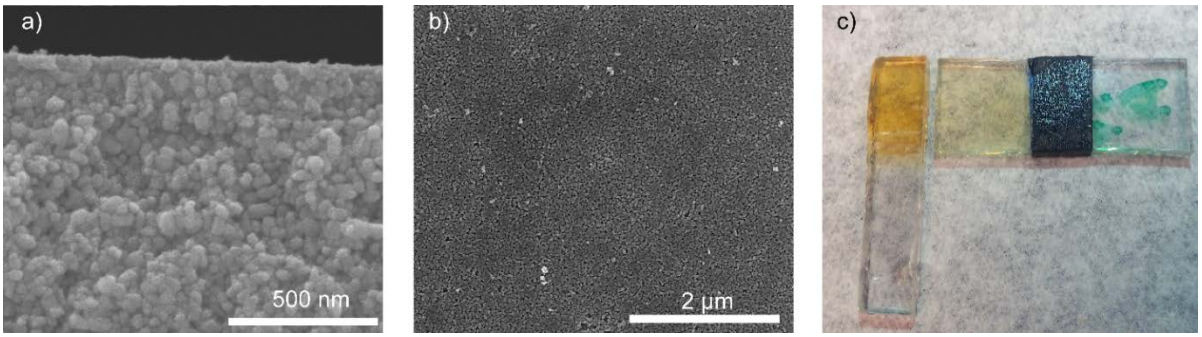

Figure. 2.10: 1) Cross-sectional SEM image of a WO_3-FeOOH electrode; b) top-down SEM image, and c) photograph of the electrode. For c), the electrode on the left is the sample used for SEM imaging and the electrode on the right is a WO_3 film for comparison. No additional layer is visible in the cross-sectional SEM image, indicating that the FeOOH may grow primarily in the interstices of the film.

establish a reliable average. Through repeated spin coating and annealing at 500 °C, we are able to obtain a thick (ca. 2 µm) and dense layer of WO_3. We have demonstrated that the addition of the FeOOH co-catalyst on the surface of WO_3 greatly enhances the Faradaic efficiency for OER as well as its stability in aqueous KP_i buffers at pH 4 and 7. Our data demonstrate that it may not be necessary to grow a thick co-catalyst layer in order to obtain improved stability and high Faradaic efficiencies for OER. Specifically, cross-sectional SEM imaging does not reveal the formation of a new distinct layer on the surface of WO_3 after FeOOH deposition (Figure. 2.10). The FeOOH film may be sufficiently thin such that it does not display a contrast difference in the SEM image. Alternatively, the FeOOH may deposit in the interstices of the WO_3 electrode. This result is intriguing since similarly constructed photoanodes using cobalt phosphate as an OEC have relied on significantly thicker (~1 µm) layers to protect the WO_3 surface.[3] It must be noted that in the previous case, the WO_3 was grown electrochemically, which yielded very dense films while the sol-gel synthesis presented here produces electrodes of a higher porosity as determined via SEM imaging.

We have observed a marked improvement in electrode stability upon the growth of the FeOOH co-catalyst on the surface of WO_3. It has been previously reported in the literature

that H_2O_2 intermediates formed during the course of OER may be responsible for the degradation of the film during the photoelectrolysis of water. To investigate this possibility, we attempted to detect peroxide using a previously reported procedure.[3] In brief a WO_3 electrode was used in a CPC experiment under 1-sun illumination for 2 hours. A reductive LSV trace in pH 4 0.1 M KP_i was collected before and after the experiment in an attempt to detect peroxide species adsorbed to the surface (Figure. A.10). We find no detectable peroxide present on the surface of the electrode after CPC under illumination, suggesting that peroxo species in this case may not be the primary cause for the observed photocurrent decline of the films. However, because soaking a WO_3 electrode overnight in a pH 4 KP_i buffer leaves both its morphology and LSV trace unchanged, the observed photocurrent decrease during electrolysis is likely photoelectrochemical in nature. Despite not observing H_2O_2, it is still possible that high energy intermediates such as $^{\bullet}OH$ formed during OER may react with WO_3.

Although the growth of the FeOOH on the sol-gel WO_3 films does enhance the stability and Faradaic efficiency for OER, we observe that adding FeOOH leads to a decrease in the chopped-light photocurrent response. We postulate that this effect may stem from three possibilities. First, it is well known that WO_3 suffers from poor selectivity for OER in a variety of buffered solutions. Indeed, our results demonstrate that the WO_3 control films only yielded Faradaic efficiencies of ca. 26.8 ±3.2% in a pH 4 KP_i electrolyte under 2-sun illumination, compared to ca. 95.9 ±1.6% Faradaic efficiency for WO_3-FeOOH electrodes. These experiments indicate that in the case of the WO_3 control, only about ~27% of the observed current in the CL-LSV may be derived from OER. Because the saturated photocurrent densities were, on average 0.8 $mA \cdot cm^{-2}$, approximately 0.22 $mA \cdot cm^{-2}$ of the observed current may be derived from water oxidation. In contrast, using the ~96% Faradaic efficiency and 0.4 ± 0.1 $mA \cdot cm^{-2}$ saturated current densities for the WO_3-FeOOH electrodes, it is determined that approximately 0.384 $mA \cdot cm^{-2}$ of current in that case is generated from OER.

Figure. 2.11 depicts CPC plots for a WO_3 and a WO_3-FeOOH electrode in which the current density has been corrected for the Faradaic efficiency for OER. These data

demonstrate that including the FeOOH OEC on WO_3 is still effectively improving both the rate and selectivity for OER since the current derived from OER is significantly greater.

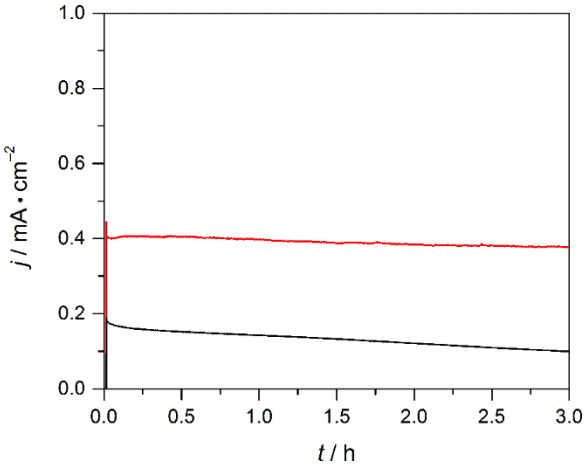

Figure. 2.11: CPC curves corrected for current derived from OER for WO_3 (black) and WO_3-FeOOH (red) at 1.23V vs. RHE and 1-sun illumination in pH 4 0.1M KP_i solution.

This result is noteworthy because if such an electrode were to be used in a PEC water splitting cell, its efficiency for OER needs to be nearly 100%.[25,26] We hypothesize that the decrease in the observed photocurrent in the CL-LSVs may be due in part to the FeOOH effectively barring side reactions from occurring. Thus although there is an observed decrease in photocurrent in the CL-LSVs, the actual Faradaic efficiency and turnover frequency for the desired reaction, i.e. the oxygen evolution reaction, is dramatically improved. It should also be noted that during the course of the oxygen detection experiments, visible bubbling was observed on the WO_3-FeOOH and not the WO_3 controls, which corroborates the fact that the hybrid electrodes have a higher turnover frequency for OER. Finally, the total amount of O_2 generated by the WO_3-FeOOH electrodes was 2–3 times greater than the total amount generated by the WO_3 controls across three trials, which further supports the conclusion that FeOOH effectively functions as a co-catalyst for OER.

Second, it may also be possible that the FeOOH OEC might effectively reduce the total surface area of the electrode. If the OEC is growing within the interstices of the porous electrode, the total active surface area of the electrode will decrease if the FeOOH grows sufficiently thick. We report the current density with respect to planar electrode area, so a reduction in active surface area would also reduce the observed current densities since there would be a lower coverage of catalytically active sites on the surface. To probe this question

further, we conducted Cottrell experiments in 0.1 M KCl solution in the presence of 6 mM $K_3[Fe(CN)_6]$ following a previously reported procedure.[27] In these experiments, the current decay vs. time was measured for the reduction of $[Fe(CN)_6]^{3-}$ to $[Fe(CN)_6]^{4-}$ in solution

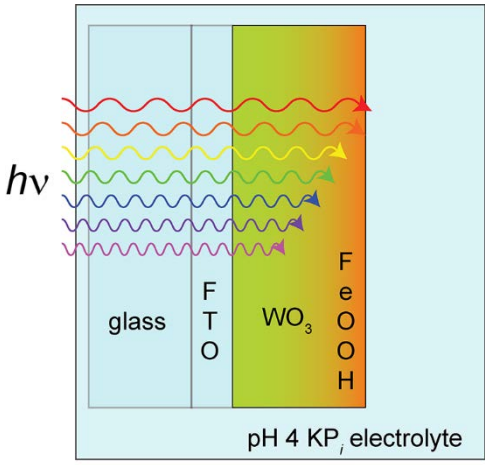

Figure. 2.12: Proposed schematic of WO_3-FeOOH electrodes.

(Figure. A.11), and we find that the electrochemically active surface area does not change significantly before and after the PEC-EC FeOOH film growth (1.06 cm^2 for the WO_3-FeOOH versus 1.07 cm^2 for the WO_3 electrode). Thus, we conclude that a change in active surface area upon deposition of the FeOOH does not play a significant role in the observed decrease in photo-current density in the CL-LSVs.

However, a third possibility for the observed decrease in saturated photocurrent may stem from parasitic light absorption from the FeOOH film. Indeed, the Kubelka-Munk F(R) spectrum of an FeOOH spectrum grown on FTO (Figure A.6) demonstrates that this layer can behave as a strong light absorber, and it may therefore compete with WO_3 for photon absorption. To probe this question further, we plotted the results of the EQE experiments as the ratio of EQE WO_3-FeOOH / EQE WO_3 at each wavelength (Figure. A.12). We observe a decrease in EQE with an increase in wavelength. Because we back illuminated the electrodes during this experiment, photons must first travel through the FTO/WO_3 interface of the film. Because longer wavelength photons have less energy, they are less likely to be absorbed closest to the FTO/WO_3 interface. As a result, they travel further through the film and nearer to the WO_3/FeOOH junction where they can be parasitically absorbed by the FeOOH OEC, illustrated in Figure 2.12. This explains why the ratio of EQE WO_3-FeOOH/ EQE WO_3 decreases with increasing wavelength and suggests that

parasitic absorption from the FeOOH reduces the number of photons reaching the WO_3 which in turn decreases the photocurrent response.

Finally, our results indicate that incorporating FeOOH onto WO_3 appears to decrease the EQE by a maximum of 10% in the region of near UV (350 – 400 nm). We hypothesize that the observed effect may again be related to the difference in Faradaic efficiencies between the two systems as well as competitive light absorption from the FeOOH. EQE simply measures current out regardless of the reaction from which it is generated. Thus, it is possible that WO_3 may display a higher EQE because it transfers holes to $H_2PO_4^-$, HPO_4^{2-}, or PO_4^{3-} with $^{\bullet}OH$ to form peroxodiphosphate ($P_2O_8^{4-}$) or peroxophophate (PO_5^{3-}).[21,24] Additionally, previous works indicate that WO_3 will readily oxidize kinetically accessible species in solution.[18,20,21] In stark contrast, our work indicates that WO_3-FeOOH electrodes will only transfer holes to water yielding O_2 as the only product in the same KP_i solution. Because OER on FeOOH occurs a lower overpotential, the increase in selectivity could in part explain why adding FeOOH decreases the EQE and saturated photocurrent in CL-LSVs. Additionally, competitive light absorption from the FeOOH layer also plays an important role since the ratio of EQE WO_3-FeOOH/EQE WO_3 decreases with increasing wavelength.

2.7 Conclusions

A simple ion-exchange and spin-coating sol-gel method gives rise to high quality, solar-responsive WO_3. Adding the solid-state FeOOH OEC by electrochemical and photoelectrochemical methods increases electrode stability and Faradaic efficiency for PEC OER in 0.1 M KP_i buffers. When a bare WO_3 electrode is used, the Faradaic efficiency for OER at pH 4 is 26.8 ±3.2%, which indicates that a significant portion of the measured current is derived from competing side reactions. Furthermore, WO_3 electrodes display poor stability at higher pH, which is reflective of photodegradation processes that may occur during the course of OER at higher pH values. In contrast, when a thin FeOOH layer is photoelectrochemically grown on the surface of these WO_3 electrodes the Faradaic efficiency is dramatically increased up to 95.9 ± 1.6%. Furthermore, this OEC significantly improves electrode stability in aqueous solutions up to pH 7. The WO_3 electrodes used in

this study were not optimized to enhance the reaction rate with respect to the active electrode surface area exposed to the electrolyte. Thus, present work focuses on generating nanostructured electrodes to yield a more efficient WO_3-FeOOH system.

2.8 Experimental

Materials. Hydrochloric acid (HCl, 36.5-38%) was purchased from VWR. Sodium tungstate ($NaWO_4$, 99+% ACROS Organics), potassium hydrogen phosphate (K_2HPO_4, 98.0% min., Alfa Aesar), potassium dihydrogen phosphate (KH_2PO_4, 99.0% min., Alfa Aesar), potassium hydroxide (KOH pellets, ≥85.0%, Fisher Chemical) and iron (II) chloride (Alfa Aesar, 99.5%) were purchased from Fisher Scientific. Attempts were made to use $FeCl_2$ from other vendors, however the solubility was different possibly due to impurities present, so only $FeCl_2$ from Alfa Aesar was used in these experiments. All reagents were used as purchased without further purification. Solutions were prepared using high purity water (Millipore Milli-Q purification system, resistivity > 18.2 MΩ).

Synthesis of WO_3 Electrodes. The WO_3 electrodes used in this work were prepared via a sol-gel method adapted from a previous report.[7,28,29] 10 mmol (3.29 g) of sodium tungstate dihydrate was dissolved in 20 mL deionized water and run through a Dowex ion exchange column that had been acidified previously with 6 M HCl and rinsed back to pH 7 with Milli-Q water. A yellow solution was eluted into in a round-bottom flask containing 20 mL absolute ethanol while stirring. The resulting transparent yellow solution (tungstic acid) was concentrated on a rotovap until the final volume was approximately 20 mL, at which time 6.6 g PEG-300 (TCI, lot. UP2XKAA, d 1.13) was added as a stabilizer. At this point, the solution was significantly more viscous and had a cloudy yellowish color. The suspension was kept stirring constantly at 1200 rpm on a stir plate and used for up to 3 days. Over time the solution's color turned dark green. However, this color change did not appear to affect the consistency or quality of the resulting electrodes. WO_3 electrodes were synthesized by dropping 30 μL of the suspension onto clean FTO slides (Pilkington Glass, TEC-15) and spinning at 2500 rpm using a Laurel spin coater for 30 seconds, followed by annealing the electrodes in a muffle furnace preheated to 500°C for 30 minutes in air. The electrode area was kept at 1 cm^2 by masking off the electrode with electrical tape prior to

spin coating. The spinning and annealing process was repeated ten times to obtain electrodes of sufficient thickness (ca. 2 μm).

Growth of FeOOH Films. A FeOOH co-catalyst layer was grown using a PEC deposition onto the WO_3 by applying a bias of 0.4 V vs. Ag/AgCl (sat'd KCl) while front illuminating a 1 cm^2 WO_3 electrode with 100 mW/cm^2 of AM1.5G light in a 0.1 M solution of $FeCl_2$ in Millipore water (pH ~4). The PEC deposition was stopped after 0.087 C of charge had passed, which took approximately 5 – 10 minutes. The purpose of the PEC deposition step is to generate nucleation sites for the FeOOH near the areas with the highest concentration of photogenerated electron-hole pairs. Following the PEC deposition, an electrochemical (EC) deposition was performed by applying a bias of 1.2 V vs. Ag/AgCl (sat'd KCl) in the dark in the same $FeCl_2$ solution. This deposition was performed until 0.07 C of charge had passed, which also took 5 – 10 minutes.

Materials Characterization. X-ray diffraction was recorded on a Bruker D8 Advance diffractometer equipped with a graphite monochromator, a Lynx-Eye detector, and parallel beam optics using Cu Kα radiation (λ = 1.541 84 Å). Patterns were collected using a 0.6 mm incidence slit, with a step size and scan rate of 0.04 °/step and 0.5 s/step, respectively. The WO_3 phase was identified as WO_3 (JCPDF 72-0677) using MDI Jade version 5.0.

UV−vis spectra were recorded using a Cary 5000 spectrophotometer (Agilent) equipped with an external diffuse reflectance accessory. Spectra were recorded in reflectance mode and transformed mathematically into the Kubelka-Munk function, F(R).

Scanning electron microscopy (SEM) images were collected using an FEI Nova Nanolab SEM/focused ion beam (FIB) instrument with an accelerating voltage of 10 kV, WD of 5 mm and beam current of 0.54 nA. For cross-sectional images, the WO_3/WO_3-FeOOH electrodes were sputter coated with Au for 10 s to dissipate surface charging and ease the imaging process.

Photoelectrochemistry. Photoelectrochemistry was performed using a CH Instruments 760 E electrochemical workstation. All PEC measurements were performed in custom-built cells with quartz viewing windows. Three-electrode voltammetry experiments were

performed using the working WO_3/WO_3-FeOOH thin-film photoanode, a Ag/AgCl (saturated KCl) reference electrode, and a Pt wire counter electrode. The supporting electrolyte in all PEC experiments was 0.1 M KP_i at pH 4 or 7. Unless specified otherwise, a 1 cm^2 area of the working electrode from the back side (glass side) was irradiated through a quartz window. Freshly prepared electrodes were employed to start each experiment to avoid cracking of the FeOOH by dehydration of the film. The light source was a Newport-Oriel 150W Xe arc lamp fitted with an AM1.5G simulating solar filter (Newport). The lamp power was adjusted to 100 mW•cm^{-2} (except for O_2 detection experiments described below) using an optical power meter (Newport 1918-R) equipped with a thermopile detector (Newport 818P-015-19).

Oxygen-Evolution Measurements. Oxygen detection was performed in a custom-built two-compartment cell separated by a fine frit. For O_2 detection experiments, the working electrode, Ag/AgCl reference electrode, and fluorescence probe (FOSSPOR, 1/8 in., Ocean Optics Inc.) were sealed in one compartment, separated from the Pt auxiliary electrode. To generate significant quantities of O_2 to provide a good signal, the O_2 detection experiments were carried out at 1.43 V vs RHE in 0.1 M KP_i electrolyte using an AM1.5G filter and custom-built water filter. The lamp power was adjusted to 200 mW/cm^2. The number of moles of O_2 produced was determined from the ideal gas law using the measured volume of the head space, the temperature recorded using a NeoFox temperature probe, and the partial pressure of O_2 recorded by the FOSSPOR fluorescence probe. Dissolved O_2 in the solution was accounted for through Henry's law using the measured partial pressure of O_2 and the volume of solution in the cell. Throughout the experiment, the solution was stirred to aid O_2 dissociation from the working electrode. The working electrode compartment contained 20 mL of electrolyte and 25 mL of head space. The fluorescence probe was calibrated with a two point calibration (0.00% O_2 and 20.9% O_2) using NeoFox software (Ocean Optics Inc.). Before the experiment was begun, the percentage of O_2 was recorded for 30 – 45 min to ensure the cell was sealed completely from the atmosphere and to create a baseline. Then, it was measured for a period of time after the light was turned off. An important note is that during O_2 measurements, some O_2 was detected that was not produced photoelectro-chemically, but was detected because of drift in the fluorescence probe's calibration as the temperature slightly increased over the course of illumination.

This fluctuation was accounted for by subtracting it from the baseline in the data work up. The Faradic efficiency was determined by dividing the measured moles of O_2 by the theoretical yield, which is determined by dividing the total charge passed during the experiment by 4F (4-electron oxidation, F = Faraday's constant, 96 485 C/mol of e^-).

External Quantum Efficiency Measurements. Quantum efficiency measurements were obtained with an Oriel 150 W Xe arc lamp (Newport) and a quarter-turn single-grating monochromator (Newport). Sample measurements were recorded with chopped illumination (15/20 Hz), and a quartz beam splitter was used to simultaneously record the light output intensity with a separate Si photodiode (Newport) to adjust for fluctuations in lamp intensity. The potential of the working photoelectrode was poised to 1.23 V vs. RHE, and the absolute photocurrent was measured by a digital PAR 263 potentiostat. The output current signal was connected to a Stanford Instruments SR830 lock-in amplifier, and the output signals from the lock-in amplifier and the reference Si photodiode were fed into a computer controlled by custom written LabVIEW software. Spectral response measurements were obtained in a pH 4 0.1 M KP_i buffered solution.

2.9 References

(1) Reyes-Gil, K. R.; Wiggenhorn, C.; Brunschwig, B. S.; Lewis, N. S. *J. Phys. Chem. C* **2013**, *117*, 14947.
(2) Wang, H.; Lindgren, T.; He, J.; Hagfeldt, A.; Lindquist, S.-E. *J. Phys. Chem. B* **2000**, *104*, 5686.
(3) Seabold, J. A.; Choi, K. *Chem. Mater.* **2011**, *23* (5), 1105.
(4) Yourey, J. E.; Bartlett, B. M. *J. Mater. Chem.* **2011**, *21* (21), 7651.
(5) Liu, R.; Lin, Y.; Chou, L. Y.; Sheehan, S. W.; He, W.; Zhang, F.; Hou, H. J. M.; Wang, D. *Angew. Chemie - Int. Ed.* **2011**, *50* (2), 499.
(6) Lillard, R. S.; Kanner, G. S.; Butt, D. P. *J. Electrochem. Soc.* **1998**, *145* (8), 2718.
(7) Augustynski, J.; Solarska, R.; Hagemann, H.; Santato, C. *Proc. SPIE* **2006**, *6340* (2006), 63400J.
(8) Seabold, J. A.; Choi, K.-S. *J. Am. Chem. Soc.* **2012**, *134* (4), 2186.
(9) Louie, M. W.; Bell, A. T. *J. Am. Chem. Soc.* **2013**, *135* (33), 12329.
(10) Klaus, S.; Cai, Y.; Louie, M. W.; Trotochaud, L.; Bell, A. T. *J. Phys. Chem. C.*, **2015**, 119 (13), 7243.
(11) Trotochaud, L.; Young, S. L.; Ranney, J. K.; Boettcher, S. W. *J. Am. Chem. Soc.* **2014**, *136* (18), 6744.
(12) Bediako, D. K.; Surendranath, Y.; Nocera, D. G. *J. Am. Chem. Soc.* **2013**, *135* (9), 3662.
(13) Chemelewski, W. D.; Rosenstock, J. R.; Mullins, C. B. *J. Mater. Chem. A* **2014**, *2*, 14957.
(14) Chemelewski, W. D.; Lee, H. C.; Lin, J. F.; Bard, A. J.; Mullins, C. B. *J. Am. Chem. Soc.* **2014**, 136 (7), 2843.
(15) Tamirat, A. G.; Su, W.-N.; Dubale, A. A.; Chen, H.-M.; Hwang, B.-J. *J. Mater. Chem. A* **2015**, *3*, 5949.
(16) McDonald, K. J.; Choi, K.-S. *Energy Environ. Sci.* **2012**, *5* (9), 8553.

(17) Damjanovic, A.; Dey, A.; Bockris, J. O. *Electrochim. Acta.* **1966**, *11*, 791.
(18) Hill, J. C.; Choi, K. *J. Phys. Chem. C.* **2012**, *116* (14), 7612.
(19) Henry, C. H.; Logan, R. A.; Merritt, F. R. *J. Appl. Phys.* **1978**, *49*, 3530.
(20) Mi, Q.; Zhanaidarova, A.; Brunschwig, B. S.; Gray, H. B.; Lewis, N. S. *Energy Environ. Sci.* **2012**, *5* (2), 5694.
(21) Mi, Q.; Coridan, R. H.; Brunschwig, B. S.; Gray, H. B.; Lewis, N. S. *Energy Environ. Sci.* **2013**, *6* (9), 2646.
(22) Bardizza, G.; Pavanello, D.; Mullejans, H.; Sample, T. *Prog. Photovoltaics Res. Appl.* **2014**, *29th EU PV*.
(23) Schultze, J. W.; Mohr, S.; Lohrengel, M. M. *J. Electroanal. Chem.* **1983**, *154*, 57.
(24) Lyons, M. E. G.; Burke, L. D. *J. Electroanal. Chem. Interfacial Electrochem.* **1984**, *170* (1–2), 377.
(25) Alexander, B. D.; Kulesza, P.; Rutkowska, I.; Solarska, R.; Augustynski, J. *J. Mater. Chem.* **2008**, *18*, 2298.
(26) Maeda, K.; Higashi, M.; Lu, D.; Abe, R.; Domen, K. *J. Am. Chem. Soc.* **2010**, *132* (16), 5858.
(27) Konopka, S. J.; McDuffie, B. *Anal. Chem.* **1970**, *42* (14), 1741.
(28) Santato, C.; Odziemkowski, M.; Ulmann, M.; Augustynski, J. *J. Am. Chem. Soc.* **2001**, *123* (43), 10639.
(29) Solarska, R.; Jurczakowski, R.; Augustynski, J. *Nanoscale* **2012**, *4* (5), 1553.

Chapter 3

In Operando Detection of Intermediates Formed during the Photoelectrochemical Oxygen Evolution Reaction on a WO_3 Rotating Ring Disk Electrode

3.1 Introduction

Although WO_3 is an attractive material for use as a photocatalyst for water oxidation, it has been observed that its photocurrent still decreases over time, even in pH regimes in which it is predicted to be thermodynamically stable ($pH \leq 4$).[1] It has been proposed that the source of the observed photocurrent degradation under anodic conditions is due to the formation of peroxo intermediates on the surface which could possibly attack the WO_3 to degrade it via the production of water soluble peroxo-tungstate species:[2,3]

(Eqn. 3.1) $$2\ WO_3 + 3\ H_2O_2 \rightarrow W_2O_{11}^{2-} + H_2O + 4\ H^+ + 2e^-$$

To date, most techniques that have been employed to detect these species have used electrochemistry or UV-Vis spectroscopy to search for these products post mortem.[2–4] A limitation of these types of techniques is that they are unable to probe species that are formed in-operando since there is inherently a time delay between the formation of the species and the measurement employed. This is particularly important if the species produced during the photoelectrochemical oxidation of water are highly energetic oxidants; oftentimes, such species are short lived and their short lifetimes make them difficult to detect.

In order to detect these types of intermediates and to further probe the nature of the observed photocurrent decay on WO_3 photoelectrodes, we built a rotating ring disk Photoelectrochemistry (RRDPE) setup that allows for the study of thin films of metal oxides. Rotating ring disk voltammetry is an attractive means of detecting products *in operando*. Furthermore, this technique is easy to adapt for the investigation of photoelectrodes if a special optical cell is constructed allowing illumination from the bottom.[5] In particular, this procedure is

well suited towards the detection of H_2O_2 byproducts and has been employed for this specific task for the last few decades with the investigation of the ORR.[6] As a result, we sought to further develop this method and use it for *in-operando* product detection during the course of photoelectrochemical water oxidation on WO_3.

3.2 Rotating Ring Disk Photoelectrode Design

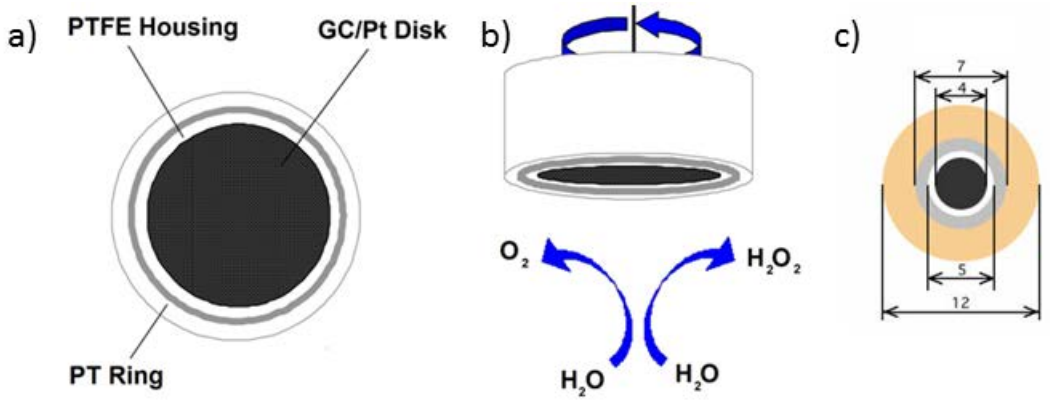

Figure 3.1: a) Bottom view of a rotating ring disk electrode. b) View of a RRDE from the side. As the electrode is rotated solution flows from the center of the electrode out towards the edges. Products formed at the disk can then be detected at the ring. c) Depicts the specific dimensions in mm of the RRDPE employed for this work.

When designing the apparatus we sought a modular system that would allow for the use of multiple types of disk electrodes. Furthermore, having a removable disk would be particularly advantageous since this would make it easy to use with common thin film deposition methods such as spray pyrolysis and sol-gel spin coating.[7] Furthermore, previous reports using rotating ring disk electrodes of metal oxides employed the use of a compacted metal oxide pellet as the central disk.[5,8] Using a thin film electrode instead provides a more accurate representation of how a real electrode would work since these types of designs would be the easiest to deploy in actual devices.

Figure 3.1a depicts a rotating ring disk photoelectrode viewed from below. In the center is the removable disk which is made of either Pt or glassy carbon. Outside the disk lies a Teflon spacer which electrically isolates it from the platinum ring which is used to detect errant species that are projected from the disk under rotation. Because the disk is removable, thin films of metal oxides can easily be loaded onto the disk via spin coating a sol-gel precursor or by using spray pyrolysis.

When the disk is rotated solution flows towards the center of the disk and is projected out towards the edges as depicted by Figure 3.1b. By controlling the rotation speed of the electrode, the flux of the solution to the primary working electrode (disk) can be regulated. Because the solution flows from the center of the RRDE to the outside edges, this allows for products formed at the disk to be detected at the ring since the solution flux forces these products to flow over the ring. Furthermore, in the rotating ring disk electrode, both the ring and the disk function as independent working electrodes controlled by a bipotentiostat. As a result, by poising the ring at different potentials, different species may be detected.

In the case of laminar flow (lower rotational velocity where turbulence is not significant), the flux of solution can be modeled by solving the requisite fluid dynamics equations. Furthermore, from this analysis one can extract the theoretical collection efficiency (N) equation for any given rotating ring disk electrode[9]:

(Eqn. 3.2) $N_t = 1 - F\left(\frac{\alpha}{\beta}\right) + \beta^{\frac{2}{3}}[1 - F(\alpha)] - (1 + \alpha + \beta)^{\frac{2}{3}}\{1 - F\left[\left(\frac{\alpha}{\beta}\right)(1 + \alpha + \beta)\right]\}$

Where N is the collection efficiency and α and β are given by[9]:

(Eqn. 3.3) $\alpha = (\frac{r_2}{r_1})^3 - 1$

(Eqn. 3.4) $\beta^{2/3} = (\frac{r_3^3}{r_1^3} - \frac{r_2^3}{r_1^3})^{2/3}$

The values of r_1, r_2 and r_3 correspond to the disk diameter and the inner and outer diameters of the ring respectively. These dimensions are determined by the specific design of the rotating ring disk electrode employed and the ones used for this work are depicted in Figure 3.1c.

Although the theoretical collection efficiency equation is a useful aide when constructing a RRDE, there is often a variance between theoretical and empirical collection efficiencies due to small imperfections introduced onto the electrode when machining or polishing the surface. As a result, it is critical to evaluate an RRDE's collection efficiency empirically.[9] Consider the experiment in which the disk is held at some potential E_D, where the reaction O + n e^- → R produces a cathodic current i_D, while the ring is maintained at a sufficiently oxidizing potential E_R that any R that reaches the disk surface is immediately oxidized back to O. By determining the ratio of the currents i_R and i_D, we can define the empirical collection efficiency as:

(Eqn. 3.5) $$N_{emp} = \frac{-i_R}{i_D}$$

In the case of the RRDE employed for this work, r_1 = 2, r_2 = 2.5 and r_3 = 3.5mm (d_{disk} = 4, $d_{inside\ ring}$ = 5 and $d_{outside\ ring}$ = 7mm). By solving equation 3.1 we find N_t = 42.4 for this electrode geometry.

To determine the empirical collection efficiency of the Pt/Pt RRDE electrode the reduction of $K_3Fe(CN)_6$ to $K_4Fe(CN)_6$ was used a test reaction. This experiment was performed with the Pt disk only since competition from WO_3 reduction would deflate the actual collection

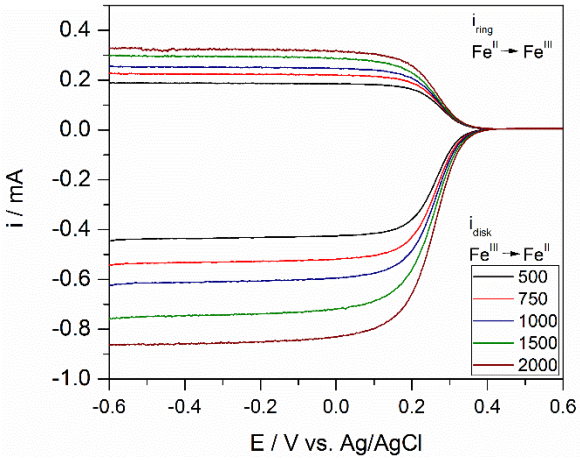

Figure 3.2: Empirical collection efficiency of a Pt/Pt rotating ring disk electrode with r_1 = 2, r_2 = 2.5 and r_3 = 3.5mm. $[Fe(CN)_6]^{3-}$ was reduced at the disk and reoxidized at the ring using linear sweep voltammetry while rotating the electrode at various RPMs (500-2000). The solution employed was 0.01M $K_3Fe(CN)_6$ and the disk electrode potential was swept at 20 mV/s while the ring potential was fixed at 1V vs. the Ag/AgCl reference.

efficiency since the disk current would be much larger than the ring current due to it being composed of reductive currents from two different processes (WO_3 reduction + $[Fe(CN)_6]^{3-}$ reduction).[10–12] The reduction of $[Fe(CN)_6]^{3-}$ was selected due the rapid kinetics of this reaction on a Pt surface.[5,13] To conduct this experiment, an LSV was performed at the disk while the electrode was spinning at various RPMs while the ring was held at a fixed potential such that any $[Fe(CN)_6]^{4-}$ that met the ring would be immediately oxidized. The results of this experiment are demonstrated in Figure. 3.2 and the calculated N_{emp} is 40.6 ±2.4%. The slight variance in N_{emp} vs N_t could result from surface imperfections introduced when polishing, or due to a slight difference in height between the central disk and the outer ring.[9] This height difference may arise since the central disk is removable and must be mounted into the electrode prior to all experiments. Typically, after the disk is mounted into the RRDE the electrode is polished to obtain a flat and

level surface. Because we are using a Pt disk that has a thin (< 5 μm) film of WO_3 on the surface, polishing is challenging since it could potentially remove the WO_3 thin film in its entirety. As a result, after the disk was mounted no polishing was performed.

3.3 Spray Pyrolysis Synthesis of WO_3

WO_3 was deposited onto a Pt disk substrate via spray pyrolysis. Briefly, a solution containing a mixture of ammonium metatungstate and PEG-300 was sprayed onto a Pt disk heated to 205°C. It is hypothesized that the following chemical reaction took place:

(Eqn. 3.6) $$(NH_4)_6H_2W_{12}O_{40}\ (aq.) \rightarrow 12WO_3\ (s.) + 6NH_3\ (g.) + 4H_2O\ (g.)$$

This morphology was desirable in order to avoid any exposed Pt substrate being in contact with the solution. The spraying was pulsed and the nozzle would actively spray solution for 1s

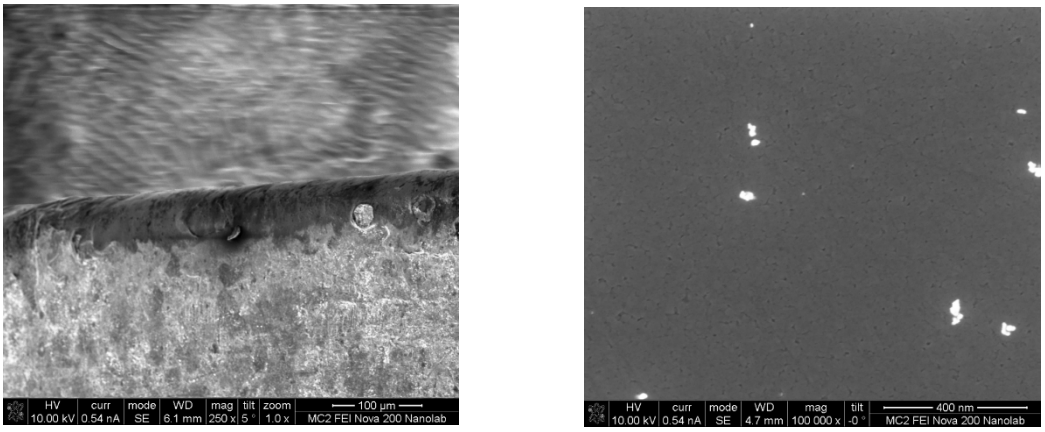

Figure 3.3: Cross sectional (left) and top down (right) SEM images of a WO_3 thin film that was spray deposited onto a Pt disk substrate. The white spots on the right image are alumina powder used for electrode polishing.

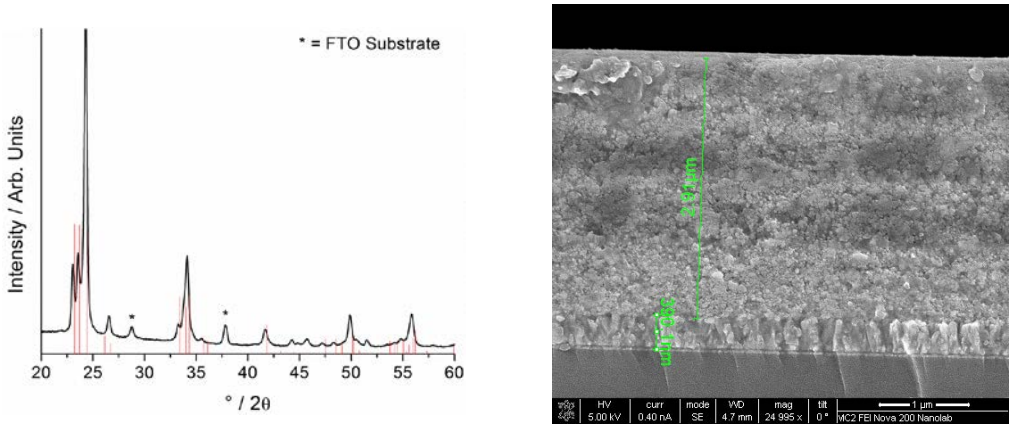

Figure 3.4: a) X-ray diffraction pattern of a WO_3 grown via spray pyrolysis on a FTO coated glass substrate. *'s indicate peaks from the underlying FTO substrate and vertical red lines indicate peaks identified from JCPDF #72-0677. b) Cross sectional SEM image of the same WO_3 thin film electrode.

with a 5s delay in between sprays to allow for solvent evaporation. The spraying was repeated for 200 cycles and once it was complete the electrode was placed in a furnace that was preheated to 500°C so that the WO_3 could anneal for one hour. This procedure was repeated a total of five times to obtain a thick layer of WO_3 on the surface of the platinum electrode.

SEM images of the WO_3 deposited onto the Pt electrode reveal a compact and dense surface layer. Because of the way the material deposited on the edges of the Pt disk, this made it difficult to accurately determine the WO_3 thickness (Figure 3.3). As a result, WO_3 was grown on FTO coated glass slides using the same spraying procedure. XRD data for these films indicate that they are pure WO_3 (Figure 3.4a). Furthermore, cross-sectional SEM images indicate that the films are ~3 µM thick (Figure 3.4b).

3.4 Electrochemistry of WO_3:Pt RRDPE in Acidic Solutions

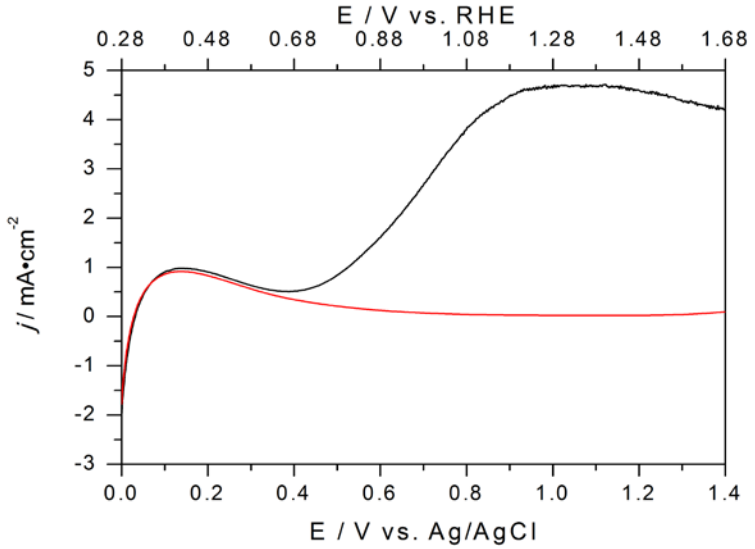

Figure 3.5: Linear sweep voltammograms of a WO_3 thin film grown on a Pt RRDE. Black represents the LSV under illumination by a 150 W Xenon lamp and red is in the dark. Solution is 1N H_3PO_4, pH 1.4. Sweep rate is 20 mV/s.

Figure 3.5 depicts LSVs of a WO_3 thin film grown on a Pt disk (hereafter referred to as WO_3:Pt) in the dark and under illumination. A large oxidation wave is observed at 0.38 V vs. RHE due to the oxidation of H_xWO_3 impurities with concurrent proton deintercalation.[10,14] Protons can be intercalated into WO_3 at the starting potential of 0.28 V vs. RHE for the LSV so as the potential is swept further positive, these protons can then be deintercalated with concurrent H_xWO_3 oxidation in the following reaction:

(Eqn. 3.7) $H_xWO_3 \rightarrow WO_3 + x\,H^+ + x\,e^-$

A one to one electron to proton ratio is observed since electrons are added to the WO_3 via the reduction of the W^{6+}. As a result, H^+ cations are intercalated into the structure to compensate for the additional negative charge around the W cations.[14] The reverse process takes place upon re-oxidation of the WO_3 electrode. This effect is tied to the electrochromic properties of WO_3 which are a result of its reversible redox chemistry.[10] This peak is key since it demonstrates the chemistry of the electrode is governed by the WO_3 thin film and not the underlying Pt substrate. Furthermore, in the absence of illumination the current at 1.28 V vs RHE is ~0 $mA \bullet cm^{-2}$. However, upon illumination a maximal photocurrent of *4.5* $mA \bullet cm^{-2}$ is observed at this potential. The 360 fold increase in photocurrent upon illumination along with the minute dark current demonstrates that the photoactive WO_3 material dominates the observed chemistry under these conditions.

O_2 production under photoelectrochemical conditions was probed using RRDPE. For these experiments, the disk electrode was poised at 1.24 V vs. RHE with the ring poised at 0.36 V vs. RHE. This ring potential was selected since oxygen reduction is under diffusion control at this potential on Pt (Appendix B.1). For these experiments, the disk and ring currents were allowed to equilibrate in the dark for 100s prior to tuning on the light source. The light source was then chopped every 10s until 100s had passed.

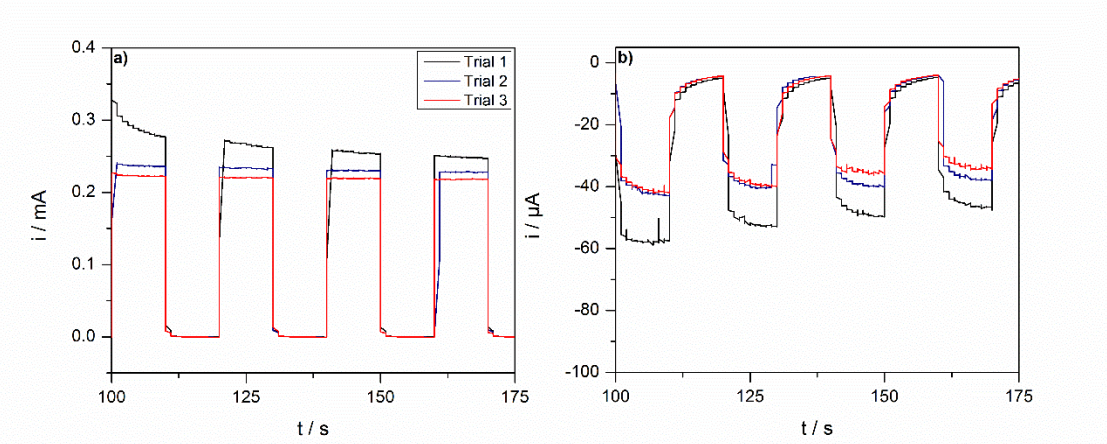

Figure 3.6: a) Disk current for a WO_3:Pt disk under chopped illumination after consecutive runs. b) Ring current at the Pt ring under chopped illumination after consecutive runs. For all trials the electrode was rotated at 2000 rpm in 1 N H_3PO_4. The applied potentials at the disk and the ring were 1.24 and 0.36 V vs. RHE respectively. The source of illumination was a 150 W xenon lamp.

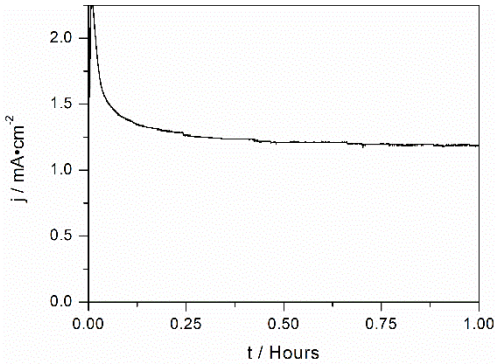

Figure 3.7: Bulk electrolysis of a WO_3:Pt RRDE under illumination by a 150 W xenon lamp in 1N H_3PO_4. The applied potential was 1.38 V vs. RHE.

In the case of a WO_3:Pt disk in 1 N H_3PO_4, photocurrent hysteresis was observed. Figure 3.6 demonstrates how photocurrent decreases with additional experimental trials at the same rotation speed which affirms that the photocurrent decrease is independent of rotation speed and thus is related to an electrode based process. However, it was observed that after pre-treating the electrode by applying a bias of 1.38 V vs. RHE under illumination by a 150 W xenon lamp for 1 hour the photocurrent would decrease and eventually reach a stable value (Figure 3.7). Once the pre-polarization was complete the disk photocurrent was stabilized and remained constant for the rest of the experimental runs. Similar photocurrent hysteresis was also observed in 1N H_2SO_4 solution (Appendix B.2). This supports the idea that the observed hysteresis is not related to the nature of the electrolyte. However, after pre-polarization, the photocurrent stabilized and again yielded consistent values for the disk.

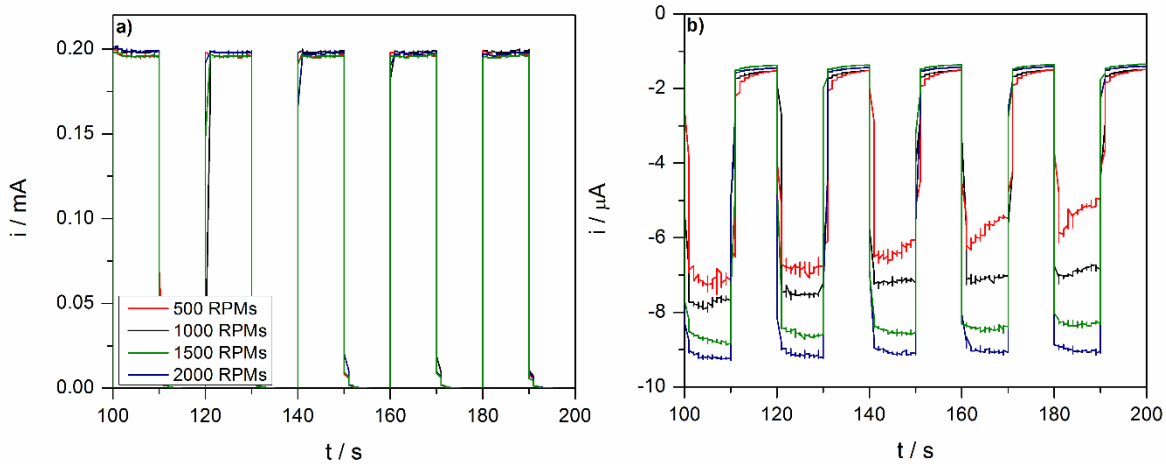

Figure 3.8: a) Disk current for a pre-electrolyzed WO_3 thin film grown on Pt under chopped illumination at various RPMs. b) Ring current at the Pt ring under chopped illumination at different RPMs. For all trials the solution employed was 1N H_3PO_4. The applied potentials at the disk and the ring were 1.24 and 0.36 V respectively. The source of illumination was a 150W xenon lamp.

For the O_2 detection experiments carried out in 1 N H_3PO_4 the disk photocurrent was independent of rotation speed and was 0.197 ± 0.001 mA (Figure 3.8a) across four different rotation speeds. This result indicates that above 500 RPMs the observed photocurrent at the disk is kinetically limited since if it was diffusion controlled there would be a clear dependence between photocurrent and rotation speed. On the other hand, the observed ring currents were dependent on rotation speed, with higher rotation speeds yielding higher ring currents (Figure 3.8b). Furthermore, the appearance of the ring currents coincided with the disk photocurrent. This behavior is consistent with the detection of a species that has a low concentration in solution which in turn, supports the idea that O_2 from the disk is detected. Since the local concentration of O_2 at the ring is dependent on the rate at which O_2 reaches the ring, higher rotation speeds will increase the flux of O_2 at the ring and thus will increase the observed current as well.

It is important to consider the magnitudes of the observed currents as well and to place them in the context of the calculated collection efficiency for the RRDE. For this particular electrode geometry, it was determined using a $Fe(CN)_6^{3-}/Fe(CN_6)^{4-}$ redox couple that N_{emp} = ~40.6. With this collection efficiency, if the WO_3 thin films produced O_2 with 100% F.E. and the Pt disk is assumed to immediately oxidize all O_2 back to H_2O at the applied potential, then the observed ring current should be (0.196*0.406) = ~0.079 mA. In the observed case the maximal ring current measured is 0.009 mA. Using the previous assumptions, a Faradaic efficiency may be calculated as follows:

(Eqn. 3.8) $\quad F.E. = (i_m/i_t)\bullet 100$

Where i_m is the measured current and i_t is calculated as follows:

(Eqn. 3.9) $\quad i_t = i_{m,d}\bullet N_{emp}$

Where $i_{m,d}$ is the measured disk photocurrent. Using these formulas, the calculated F.E. is 11.39%. This calculated value is much lower than that previously reported for WO_3.[1–4,15] The source of this discrepancy may be threefold: first, the H_3PO_4 employed contained trace amount of metals such as Fe (0.003% Fe). Thus, it is possible that over the course of multiple experimental runs trace metals may have deposited cathodically onto the Pt ring which would increase the overpotential required to drive ORR at the Pt ring and thus would decrease the observed current.[9,16] Appendix

B.3 demonstrates how the ring current decreased with consecutive runs which suggests the possibility that trace metals may have poisoned the ring during the course of the experiments.

Second it is important to consider the differences between an experiment that measures collection efficiency and the experiment at hand. For the collection efficiency measurement, it relied on a redox process that was under diffusion control at the disk. Thus the disk current would change as a function of rotation speed. Because the ring current relied on the flux of product from the disk, the process at the ring was under diffusion control as well and the two scaled together. In the case of O_2 detection using thin films of WO_3, the reaction at the disk is **not** under diffusion control but the reaction at the ring **is** (because there is no O_2 in solution to start with since it was sparged with N_2 beforehand). If the disk reaction were under diffusion control, then the disk current would vary as a function of rotation speed which is **not** observed in this case. Thus it is problematic to try to apply a collection efficiency that was derived using a reaction under pure diffusion control to a system in which the disk and ring currents are under two different types of control mechanisms (kinetic vs diffusion). As a result, this can impact the calculated F.E.

Finally, when calculating the F.E. the assumption is made that the only reaction occurring at the disk is the four electron ORR:

(Eqn. 3.10) $$O_2 + 4\,H^+ + 4\,e^- \rightarrow 2\,H_2O$$

However, it has been demonstrated in the literature[5] that partial reduction of O_2 to H_2O_2 can compete with ORR as follows:

(Eqn. 3.11) $$O_2 + 2\,H^+ + 2\,e^- \rightarrow H_2O_2$$

If a significant amount of the O_2 produced is reduced to H_2O_2 and not H_2O then this will decrease the observed ring current since H_2O_2 formation from O_2 is only a two electron process. Indeed, if the F.E. is calculated under the assumption that O_2 is solely reduced to H_2O_2, then the calculated F.E. for O_2 production at the ring is ~22% which is closer to the previously reported values for WO_3.[1,2,4]

In the present case it is difficult to discern what the source of the discrepancy in the measured F.E. for OER is. However, this effect has been previously observed using a TiO_2 rotating ring disk electrode.[5] The authors of the latter work concluded that the observed result was a

combination of the above possibilities. Despite this shortcoming, the above results demonstrate that the RRDPE can detect photogenerated species in operando.

The presence of photoelectrochemically generated H_2O_2 was probed as well. For these experiments a similar procedure was employed as that used for the O_2 detection with the exception that the applied bias that the ring was 1.24 V vs. RHE. Under these conditions, it was observed that H_2O_2 should be oxidized to O_2 if it was formed (Appendix B.4).

Figure 3.9 demonstrates the results of H_2O_2 detection in 1 N H_3PO_4 using a prepolarized WO_3 thin film grown on a Pt disk using spray pyrolysis. It is observed that the disk photocurrent is the same across four different rotation speeds which again indicates that the process at the disk is under kinetic control. On the other hand, the currents observed at the ring are *cathodic* and increase with increasing rotation speed. Furthermore, the ring currents appear when the electrode is illuminated which reveals that they are the result of photogenerated species that are produced at the disk. The presence of cathodic ring currents indicates that either H_2O_2 is not formed and released from the disk, or it is formed in such small concentrations that it is not detectable using this technique. Furthermore, the cathodic nature of the ring current reveals that a highly oxidizing product is formed at the disk, possibly peroxophosphate since the reduction potential of that species lies at 2.01 V vs. NHE.

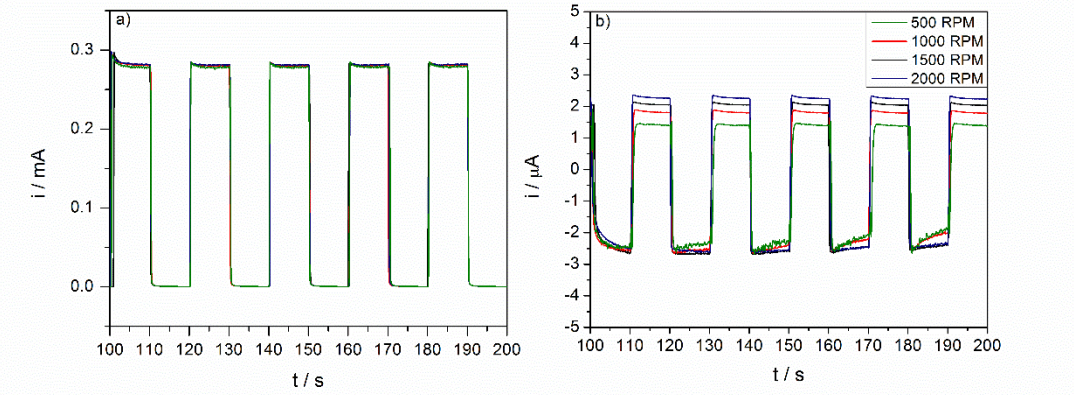

Figure 3.9: a) Disk current for a pre-electrolyzed WO_3 thin film grown on Pt under chopped illumination at various RPMs. b) Ring current at the Pt ring under chopped illumination at different RPMs. For all trials the solution employed was 1N H_3PO_4. The applied potentials at the disk and the ring were 1.24 and 1.24 V respectively. The source of illumination was a 150W xenon lamp.

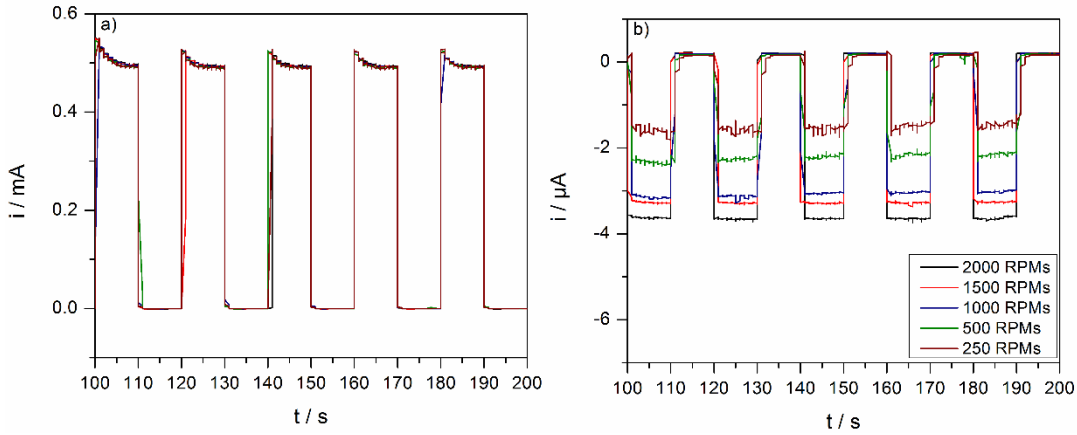

Figure 3.10: a) Disk current for a pre-electrolyzed WO_3 thin film grown on Pt under chopped illumination at various RPMs. b) Ring current at the Pt ring under chopped illumination at different RPMs. For all trials the solution employed was 1N H_2SO_4. The applied potentials at the disk and the ring were 1.24 and 1.24 V respectively. The source of illumination was a 150W xenon lamp.

To further investigate the nature of the cathodic ring currents, the same type of detection experiment was also conducted in 1 *N* H_2SO_4 solution (Figure 3.10). We observe that after prepolarizing the WO_3 thin film, the photocurrents remain stable and are the same across various rotation frequencies. However, we still observe the presence of cathodic photocurrents at the ring which appear only once the disk is illuminated. Again, this behavior suggests the detection of photogenerated species produced by the disk. It is possible that under these conditions, persulfate species are formed. Indeed, persulfate formation during the photoelectrolysis of water using WO_3 electrodes has been previously reported.[3] However, to quantify the amount of persulfate species formed, spectrometric titrations will need to be performed.

3.5 Photocurrent Hysteresis in WO_3 Photoelectrodes

While conducting rotating ring disk electrode experiments using WO_3:Pt photoelectrodes hysteresis was observed in the photocurrent. With increasing number of experiments conducted the observed photocurrent generated by the WO_3:Pt disk would decrease over time which was demonstrated in Figure 3.6. The observed photocurrent decrease is peculiar since thermodynamic Pourbaix diagrams of WO_3 predict this material to be oxidatively stable at this applied potential (1.24 V vs. RHE) and pH (pH = 1.4 for 1 N H_3PO_4).[2] Furthermore, the observed stabilization of the photocurrent (Figure 3.7) after controlled potential coulometry under illumination indicates that the photocurrent loss is due to processes that are not destructive in nature. Indeed, if this current loss was attributable to electrode degradation then it would continue to decline until all the

electrode material was destroyed and no photocurrent could be generated. The observed behavior in concentrated acidic solution raised the question of whether or not similar photocurrent decay that is observed at pH 4 (Figure 2.8) is a result of the same type of non-destructive process. To probe this matter further, controlled potential coulometry under constant illumination was conducted using sol-gel WO_3 electrodes. These experiments were followed by LSV and SEM experiments to further understand the nature of the observed photocurrent decay.

Figure 3.11a depicts the controlled potential coulometry of a sol-gel WO_3 film under 2 sun-illumination (200 mW/cm^2 AM1.5G filtered light) over 16 hours. It is observed that the photocurrent decreases from ~1.5 mA•cm^{-2} to ~0.25 mA•cm^{-2} over the course of 13 hours and that this photocurrent magnitude remains stable until the light was finally turned off at 18 hours. Furthermore, CL-LSVs collected before and after the experiment reveal a decreased in saturated photocurrent density (Figure 3.11b). Of note is that although the electrode demonstrates lower

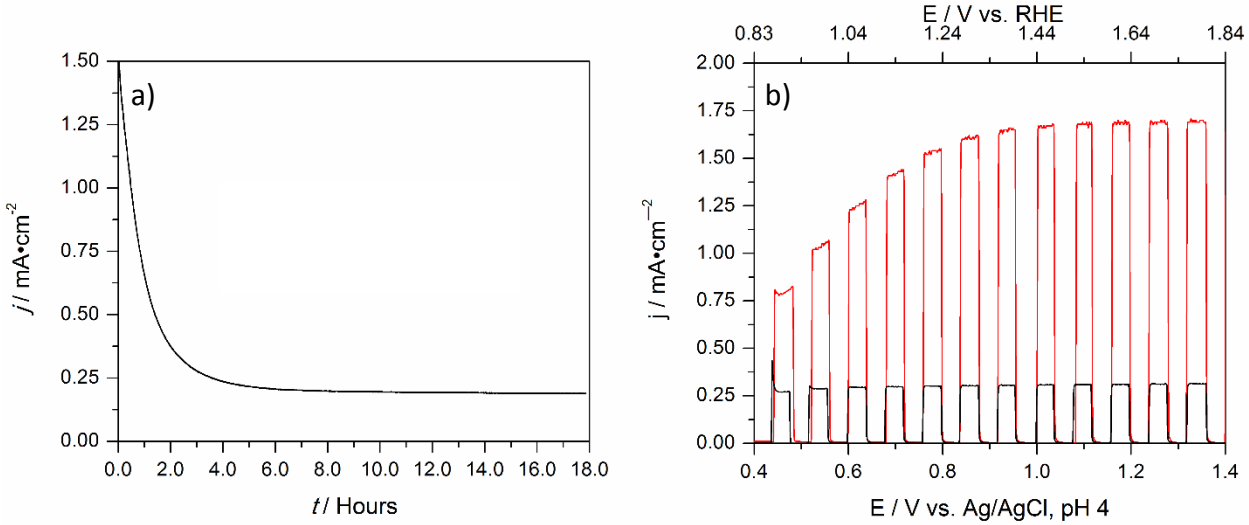

Figure 3.11: a) Controlled potential coulometry under 2-sun illumination of a WO_3 electrode in 0.1 *M* KP_i solution buffered to pH 4. The applied potential was 1.44 V vs. RHE. b) CL-LSVs of the same WO_3 film. The solution and illumination intensity were the same as that for the CPC experiment.

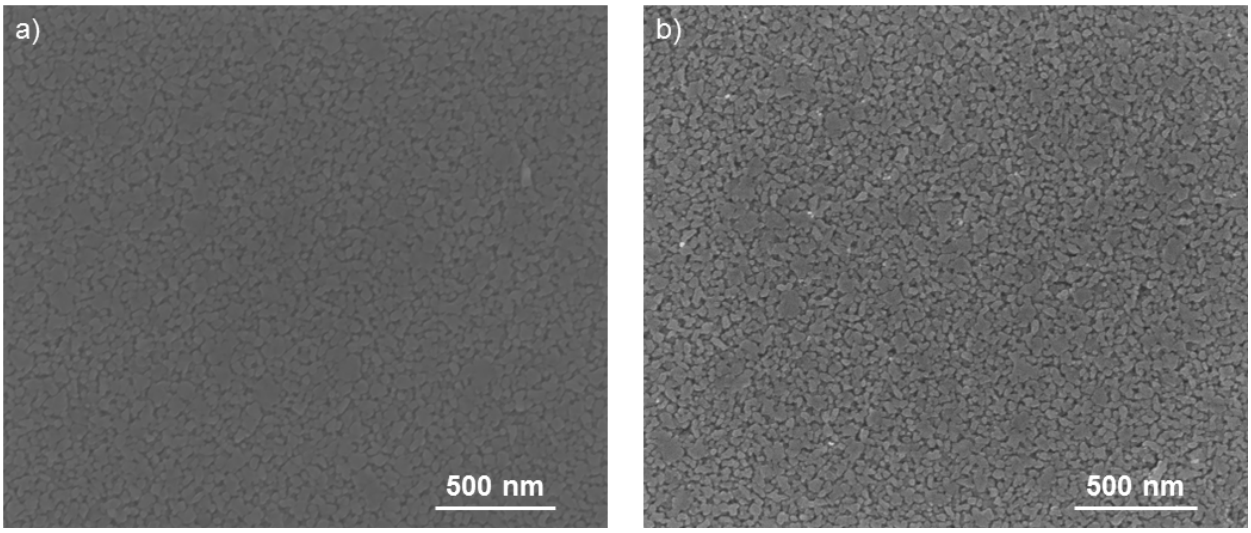

Figure 3.12: SEM images a) before and b) after an 18 hour CPC experiment under 2 suns illumination.

saturated photocurrent densities after the controlled potential coulometry experiment, it reaches these values at a much lower applied potential (< 0.4 V). Furthermore, the saturated photocurrent density measured in the CL-LSV matches exactly the final photocurrent measured in the controlled potential coulometry under illumination (~0.25 $mA \bullet cm^{-2}$). These results corroborate the notion that the observed decrease in photocurrent over time is not related to the destructive degradation of the electrode.

The change in the electrode morphology was also monitored by collecting SEM images before and after the CPC experiment. Figure 3.12 depicts demonstrates that after the 18 hour experiment there is no obvious difference in the electrode's morphology. These results suggest that the electrode itself is not degrading and indicate that processes that result in the observed photocurrent loss over time are primarily non-destructive.

These experiments all suggest an electrode driven process whereby the electrode material is undergoing some type of oxidation process. Given the electrochromic nature of WO_3, it is possible that the observed anodic photocurrent is due to the re-oxidation of the WO_3 with consequent H^+ cation deintercalation (Eqn. 3.7).

3.6 Discussion

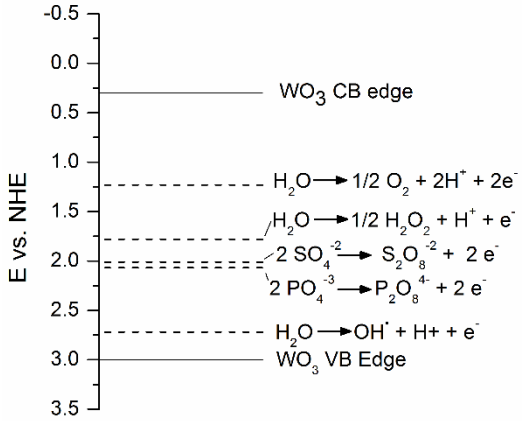

Figure 3.13: Band diagram of WO_3 depicting the valence band and conduction band edges vs. the NHE reference. Overlaid are the potentials of a variety of possible oxidation reactions that may be driven photochemically on WO_3.

WO_3 electrodes have demonstrated low Faradaic efficiencies for oxygen evolution from water under photoelectrochemical conditions. Furthermore, the photocurrents of WO_3 thin films were observed to decay in pH 4 KP_i buffered solutions. This latter result was unusual given WO_3's predicted stability under these conditions. To probe this matter further thin films of WO_3 were grown onto Pt disks using spray pyrolysis and the resulting electrodes were used in a rotating ring disk photoelectrode.

It was hypothesized that H_2O_2 could potentially be formed on WO_3. This, in turn, could lead to the degradation of WO_3 since H_2O_2 is known to react with WO_3 to form water soluble peroxy-tungstic acid species.[1,2] Figure 3.13 depicts a band diagram of WO_3. Upon illumination, a hole is produced in the valence band while an electron is promoted to the conduction band. The resulting hole can then carry out oxidative chemistry on the electrode surface. Of particular importance is the energy of the valence band. Because it sits at 3V vs. NHE, this means that WO_3 is capable of oxidizing a wide variety of substrates. Indeed, it has been demonstrated in the literature that WO_3 will readily oxidize the most kinetically accessible species in solution, as long as the species in question has a reduction potential < 3V vs. NHE.[2,3,17] Thus, this suggests that it is possible that WO_3 could oxidize water to H_2O_2 instead of all the way to O_2.

To test for the presence of H_2O_2, RRDPE experiments were conducted by applying a fixed electrical bias of 1.24 V at both the WO_3 thin film disk and the outer Pt ring. Under these conditions, if any H_2O_2 was formed, it could be detected via its *oxidation* which is the kinetically

favored reaction under these conditions.[5] It was observed that in both 1N H_2SO_4 and 1N H_3PO_4 no oxidative ring currents are detected during these experiments despite control experiments indicating that H_2O_2 should be oxidized under these conditions (Appendix B.4). Furthermore, the observed ring currents are *cathodic* in nature. These results suggest that under these conditions either no peroxide is formed, or it is formed at such low concentrations that it cannot be detected. Furthermore, the *cathodic* nature of the observed ring currents reveal the formation of highly oxidizing species on the WO_3 thin film. When considering the energy of the valence band, it is observed that photoexcited WO_3 electrode could potentially oxidize PO_4^{3-} and SO_4^{2-} anions in the following reactions:

(Eqn. 3.12) $2\ PO_4^{3-} \rightarrow P_2O_8^{4-} + 2\ e^-$ $E^o = 2.07$ V vs. NHE

(Eqn. 3.13) $2\ SO_4^{2-} \rightarrow S_2O_8^{2-} + 2\ e^-$ $E^o = 2.01$ V vs. NHE

Indeed, the detection of persulfate after performing photoelectrolysis in a solution of H_2SO_4 using a WO_3 electrode has been reported.[3] Furthermore, since the potential of peroxo formation is near that of persulfate formation, it is possible that peroxophosphate is formed under similar conditions in 1 N H_3PO_4 and would explain the observed *cathodic* currents at the ring.

However, the magnitude of the observed ring currents (on the order of μA) alone is unable to account for the large discrepancy in Faradaic efficiency for OER observed on WO_3. Indeed, about 73% of the photocurrent produced by sol-gel WO_3 electrodes in pH 4 KP_i is *not* derived from OER and the small amount of persulfate or peroxophosphate species detected using the RRDPE is unable to account for this large amount of current.[1]

Furthermore, the decrease of photocurrent over time during consecutive RRDPE experiments with the eventual stabilization of the photocurrent suggests an electrode centered "discharge" process. This process may not be related to electrode degradation since SEM images reveal no obvious destruction of the electrode post electrolysis. Additionally, under the conditions employed, WO_3 is predicted to be thermodynamically stable.

Because the current decreases over time until it reaches a stable value, this suggests that the process related to the observed current degradation relies on the consumption of a finite substrate. When considering the CL-LSVs of the WO_3:Pt RRDPE, a noticeable oxidation peak is observed at 1.28 V vs. RHE (Figure 3.5). This type of behavior demonstrates the depletion of a

reagent as the electrode potential is swept. As a result, this behavior is not attributable to OER since the OER should always be under kinetic control due to the aqueous nature of the employed solvents. If OER were the only electrode reaction taking place, then the current in the CL-LSV should attain a maximal value and remain constant until the onset potential for dark electrolysis of water is attained, at which point the current will continue to increase exponentially.

These results combined suggest that during the course of electrolysis, WO_3 undergoes a type of "discharge." Because WO_3 is an electrochromic material, it is possible that the films might discharge according to Equation 3.5. This reaction would explain why the current decreases until it eventually reaches a steady state value. At the steady state, once the electrode is fully "discharged" the only process that could occur will be OER or anion oxidation since those are the only species in solution.

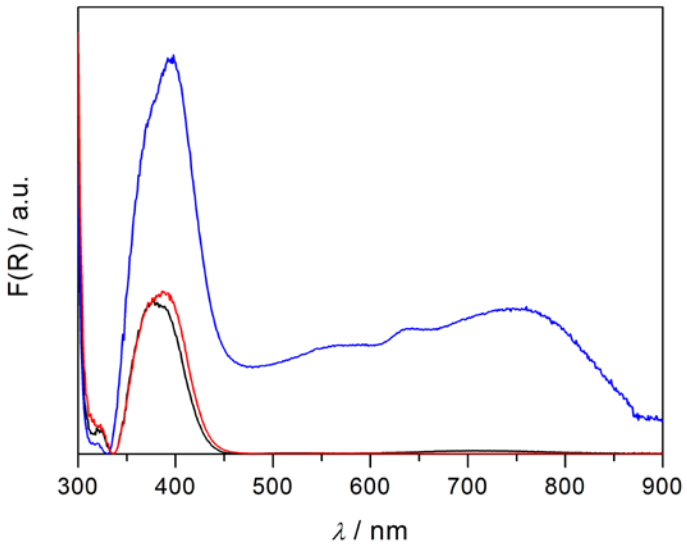

Figure 3.14: Absorption spectrum of spray pyrolyzed WO_3 thin films. (blue) is an air annealed film immediately after synthesis and (red) is the same film after an overnight bulk electrolysis under illumination. (black) is a freshly synthesized WO_3 thin film that was annealed under an atmosphere of pure O_2. This data is courtesy of Andrew Breuhaus-Alvarez.

This hypothesis does introduce the question of how the WO_3 electrode would contain reduced W impurities within it in the first place and if they do at all. It is possible that the synthesis employed is responsible for producing reduced HWO_3 impurities which contribute to the film's n-type characteristics. Because these electrodes were synthesized using large amounts of polyethylene glycol-300, there is reason to suspect that the carbon in the synthesis might reduce the WO_3 which in turn could form HWO_3 impurities in the following fashion:

(Eqn. 3.14) $$1202\ WO_3 + H(OCH_2CH_2)_{300}OH + 449.5\ O_2 \rightarrow 1202\ HWO_3 + 600\ CO_2$$

This hypothesis is supported by UV-Vis absorption data (Figure 3.14) which reveal the appearance of a broad absorption band between 600-850 nm for spray pyrolyzed WO_3 electrodes that were annealed in air. This band is consistent with that previously reported in the literature for reduced W impurities in electrochromic WO_3 thin films.[10,11,14] Furthermore, it was demonstrated that if these films are instead annealed under an atmosphere of pure O_2, this absorption band is completely absent. This effect is possibly due to the O_2 re-oxidizing any HWO_3 impurities (Eqn. 3.15) that are formed or due to the O_2 directly reacting with the PEG-300 (Eqn. 3.16) to completely convert it to CO_2 and H_2O. The chemical reactions describing these processes are as follow:

(Eqn. 3.15) $O_2 + 4\ HWO_3 \rightarrow 4\ WO_3 + 2\ H_2O$

(Eqn. 3.16) $750\ O_2 + H(OCH_2CH_2)_{300}OH \rightarrow 600\ CO_2 + 601\ H_2O$

Additionally, the films annealed in pure O_2 display almost identical absorbance spectra to the air annealed films that have been electrolyzed under anodic photoelectrochemical conditions. This supports the notion that the observed decrease in photocurrent during the course of the electrolysis is from the re-oxidation of the reduced W impurities present in the film.

Thus the observed photocurrent decrease during photoelectrolysis may be a result of WO_3's electrochromism. WO_3 has been used extensively as a material for smart windows since its color can be easily changed by varying the applied potential across a WO_3 electrode.[10,11,14] If a cathodic potential is applied to a WO_3 electrode, the W^{6+} may be reduced with concurrent cation intercalation. Depending on the concentration of reduced W, the color of the resulting electrode will range from yellow to blue for the more highly reduced forms. In the case of the previous experiments, there is no cathodic potential step applied prior to any experiments so it is unlikely that reduced W would be formed during the electrochemical experiments and again highlights the fact that reduced W is most likely formed during the electrode synthesis.

We hypothesize that the spray pyrolyzed and sol-gel processed WO_3 electrodes might be chemically reduced by the carbon present in the precursor solutions. This is supported by the absorption band between 600-850 nm in the UV-vis of the spray pyrolyzed WO_3.[11,14,18,19] The reduced W sites can then be re-oxidized during the course of photoelectrolysis. However, due to their finite concentration, the current derived from this oxidation process would decrease over time as the reduced W is consumed. Furthermore, since this is a bulk process that also involves de-

intercalation of cations, it is expected to be slow.[19] This type of behavior is what is observed during the electrolysis of a WO_3 thin film. The current slowly decreases over time and eventually reaches a stable value which supports the consumption of a finite electrode based substrate, notably, reduced W. Thus it is hypothesized the finite oxidation of reduced W impurities that are introduced during the synthesis of the WO_3 electrodes is responsible for the observed current decay over time during photoelectrolysis in aqueous solution.

3.7 Conclusions

In conclusion, in this chapter we have explored the nature of the photocurrent decrease over time that is observed on WO_3 electrodes during the photoelectrolysis of water. To this effect, rotating ring disk photoelectrode experiments were conducted under illumination from a 150 W xenon light source. In both 1 N H_2SO_4 and 1 N H_3PO_4 no H_2O_2 is detected which indicates that the formation of this species is not responsible for the large discrepancy in F.E. for OER on WO_3. However, we do observe the formation of highly oxidizing species such as persulfate and peroxo phosphate, although the magnitude of the currents produced by the reduction of these species at the Pt ring used for detection indicate that they are formed in small amounts. Thus, anion oxidation alone is unable to account for the 70% of oxidative current that is observed on WO_3 that is not accounted for by OER.

To probe whether or not this current was derived from electrode degradation, SEM images were collected after an 18h controlled potential coulometry experiment. These images reveal that the electrode is not degrading during the duration of bulk electrolysis. Furthermore, after 16 hours the photocurrent on WO_3 stabilizes which also suggests that electrode degradation is not occurring.

As a result we hypothesize that the bulk of the observed current loss is due to electrode oxidation. It is possible that reduced W sites may be introduced during the synthesis of the WO_3 electrodes where the carbon present in the PEG-300 may serve as a reductant. These reduced W sites in turn can then be re-oxidized in a sort of reverse electrochromic effect but this process is not everlasting and decreases gradually as the reduced W present in the WO_3 is consumed.

3.8 Experimental

Materials. Phosphoric Acid (HCl, 36.5-38%) was purchased from VWR. Ammonium metatungstate, potassium hydrogen phosphate (K_2HPO_4, 98.0% min., Alfa Aesar),

potassium dihydrogen phosphate (KH_2PO_4, 99.0% min., Alfa Aesar), potassium hydroxide (KOH pellets, ≥85.0%, Fisher Chemical). All reagents were used as purchased without further purification. Solutions were prepared using high purity water (Millipore Milli-Q purification system, resistivity > 18.2 MΩ).

Synthesis of WO_3 Electrodes.

Spray Pyrolysis of WO_3. The WO_3 electrodes used in this work were prepared via a spray pyrolysis procedure. 10 mmol Ammonium metatungstate (AMT, $(NH_4)_6H_2W_{12}O_{40}•xH_2O$) was added to a 100 mL volumetric flask. About 50 mL of Millipore water was added to dissolve the solid. Then, 1.1g PEG-300 was added. Finally, the mixture was diluted to 100 mL to obtain a concentration of 0.1 M in W. This precursor was then deposited onto FTO coated glass substrates or a Pt disk that were cleaned by sonicating for 10 minutes in acetone/ethanol/Millipore water/0.5M H_2SO_4. The precursor was sprayed onto the substrate in pulses, with a 1s deposition pulse followed by a 5s resting pulse to allow the solvent to evaporate. The total number of deposition pulses was 100 so the deposition took place over the course of 10 minutes. During deposition the substrate was heated to 205°C using a hotplate. After the 200 spray cycles the electrode was annealed at 500°C for 30 minutes by placing the substrate into an oven that was preheated to the desired temperature. The spray deposition followed by the annealing was repeated a total of 5 times to obtain films of sufficient thickness and conformal coverage across the Pt of FTO coated glass substrates.
Sol-Gel Deposition of WO_3. The sol-gel process used was the same one that was described in chapter 2.

Materials Characterization. X-ray diffraction was recorded on a Bruker D8 Advance diffractometer equipped with a graphite monochromator, a Lynx-Eye detector, and parallel beam optics using Cu Kα radiation (λ = 1.541 84 Å). Patterns were collected using a 0.6 mm incidence slit, with a step size and scan rate of 0.04 °/step and 0.5 s/step, respectively. The WO_3 phase was identified as WO_3 (JCPDF 72-0677) using MDI Jade version 5.0.

UV−vis spectra were recorded using a Cary 5000 spectrophotometer (Agilent) equipped with an external diffuse reflectance accessory. Spectra were recorded in reflectance mode and transformed mathematically into the Kubelka-Munk function, F(R).

Scanning electron microscopy (SEM) images were collected using an FEI Nova Nanolab SEM/focused ion beam (FIB) instrument with an accelerating voltage of 10 kV, WD of 5 mm and beam current of 0.54 nA. For cross-sectional images, the WO_3 electrodes were sputter coated with Au for 10 s to dissipate surface charging and ease the imaging process.

Photoelectrochemistry of WO_3 Films Grown on FTO coated glass. Photoelectrochemistry was performed using a CH Instruments 760 E electrochemical workstation. All PEC measurements were performed in custom-built cells with quartz viewing windows. Three-electrode voltammetry experiments were performed using the working WO_3 thin-film photoanode, a Ag/AgCl (saturated KCl) reference electrode, and a Pt wire counter electrode. The supporting electrolyte in the PEC experiments was 0.1 M KP_i at pH 4. Unless specified otherwise, a 1 cm^2 area of the working electrode from the back side (glass side) was irradiated through a quartz window. The light source was a Newport-Oriel 150W Xe arc lamp fitted with an AM1.5G simulating solar filter (Newport). The lamp power was adjusted to 200 $mW \cdot cm^{-2}$ (except for O_2 detection experiments described below) using an optical power meter (Newport 1918-R) equipped with a thermopile detector (Newport 818P-015-19).

Rotating Ring Disk Photoelectrochemistry. Rotating ring disk photoelectrochemical experiments were conducted using a spray pyrolyzed WO_3 thin film grown on a Pt substrate. A CHI 760e was used as the bipotentiostat and the RRDE apparatus was the model RRDE-3A from ALS. Thin films of WO_3 were grown on the surface of the removable disk using the previously described spray pyrolysis procedure. For the RRDPE experiments, the WO_3:Pt disk electrodes were poised at a potential of 1.24V vs. RHE. Prior to collecting any measurements, the ring was poised at the desired detection potential (0.36V vs RHE for O_2 detection and 1.24V vs RHE for H_2O_2 detection) for 30 minutes to either reduce any Pt-O that might have been present or fully oxidize the Pt surface to yield

a thin film of Pt-O. These pre-electrolysis experiments ensured that the observed chemistry during the detection experiments would only stem from chemical reactions that would result from photogenerated species reacting at the ring. Furthermore, the electrodes were left in the dark for the first 100 seconds of each experiment to allow the disk and ring currents to equilibrate prior to illumination. It was observed that the ring current typically reached a steady value after about 100s of equilibration in the dark. After 100s, the electrode would be illuminated using a Newport-Oriel 150W Xe arc lamp with no filters attached. The light was redirected using a 45 degree mirror purchased from Thor Scientific. The cell employed for these measurements was a custom built pyrex unit that had a quartz window in the bottom. This cell also had a water cooled jacket that ensured a constant temperature of 22°C during the course of all the electrochemical measurements.

3.9 References

(1) Lhermitte, C. R.; Verwer, J. G.; Bartlett, B. M. *J. Mater. Chem. A* **2016**, *4*, 2960.
(2) Hill, J. C.; Choi, K. *J. Phys. Chem. C* **2012**, *116* (14), 7612.
(3) Mi, Q.; Zhanaidarova, A.; Brunschwig, B. S.; Gray, H. B.; Lewis, N. S. *Energy Environ. Sci.* **2012**, *5* (2), 5694.
(4) Mi, Q.; Coridan, R. H.; Brunschwig, B. S.; Gray, H. B.; Lewis, N. S. *Energy Environ. Sci.* **2013**, *6* (9), 2646.
(5) Salvador, P.; Decker, F. *J. Phys. Chem.* **1984**, *88* (25), 6116.
(6) Paulus, U. A.; Schmidt, T. J.; Gasteiger, H. A.; Behm, R. J. *J. Electroanal. Chem.* **2001**, *495* (2), 134.
(7) Kozhukharov, S.; Tchaoushev, S. J. Chem. Tech. Met. **2013**, 48 (1), 111.
(8) Dare-Edwards, M. P.; Goodenough, J. B.; Hamnett, A.; Trevellick, P. R. *J. Chem. Soc. Faraday Trans.* **1983**, *79* (9), 2027.
(9) Bard, A. J.; Faulkner, L. R. *Electrochemical Methods Fundamentals and Applications*, 2nd ed.; John Wiley & Sons Inc., 2001.
(10) Kadam, P. M.; Tarwal, N. L.; Shinde, P. S.; Patil, R. S.; Deshmukh, H. P.; Patil, P. S. *Appl. Phys. A* **2009**, *97* (2), 323.
(11) Khoo, E.; Lee, P. S.; Ma, J. *J. Eur. Ceram. Soc.* **2010**, *30* (5), 1139.
(12) Santato, C.; Odziemkowski, M.; Ulmann, M.; Augustynski, J. *J. Am. Chem. Soc.* **2001**, *123* (43), 10639.
(13) Kuiken, H. K.; Bakkers, E. P. a. M.; Ligthart, H.; Kelly, J. J. *J. Electrochem. Soc.* **2000**, *147* (3), 1110.
(14) Nishio, K.; Tsuchiya, T. **2001**, *68*, 279.
(15) Seabold, J. A.; Choi, K. *Chem. Mater.* **2011**, *23* (5), 1105.
(16) Rajeshwar, K. "Fundamentals of Semiconductor Electrochemistry and Photoelectrochemistry." Encyclopedia of Electrochemistry. **2007**. Online. Accessed Dec. 23. 2016.
(17) Reyes-Gil, K. R.; Wiggenhorn, C.; Brunschwig, B. S.; Lewis, N. S. *J. Phys. Chem. C* **2013**, *117*, 14947.
(18) Bechinger, C.; Oefinger, G.; Herminghaus, S.; Leiderer, P. *J. Appl. Phys.* **1993**, *74* (7), 4527.
(19) Bard, A. J.; Reichman, B. *J. Electrochem. Soc.* **1979**, *126* (12), 2133.

Chapter 4

Chemical Kinetics of $CuWO_4$ and the Effects of Co incorporation into $CuWO_4$ to Form Thin Film Solid Solutions of $Cu_{1-x}Co_xWO_4$

Portions of this chapter have been published:
C. R. Lhermitte, B. M. Bartlett, *Acc. Chem. Res.* **2016**, 49 (6), pp 1121. Reproduced by permission of the American Chemical Society.

4.1 Introduction

The primary focus of this thesis work is to obtain a better understanding of how metal oxides catalyze water oxidation using solar energy. Furthermore, we desired to use this information to guide the synthesis of new compositions of metal oxides that demonstrate improved photocatalysis using visible light (higher solar to fuels conversion efficiency). The previous chapters of this thesis focused on the binary metal oxide, WO_3. This material was ideal for study since it is a simple metal oxide, containing only a single d^0 metal, is chemically stable in low pH regimes (pH >5), and has a small band gap (2.7 eV) which allows it to absorb visible light. However, we sought to investigate even smaller band gap materials which could use lower energy irradiation to drive the same types of chemical reactions using longer wavelengths of light. Furthermore, we specifically sought materials that demonstrate a high degree of selectivity for water oxidation in the presence of more kinetically accessible anions such as Cl^-, in addition to improved stability at higher pH values (pH <5).

Over the last few years, our group has accelerated efforts in $CuWO_4$ as a candidate for PEC OER chemistry. Its small band gap of 2.3 eV allows for using visible light to drive OER, and the reaction proceeds with a high degree of chemoselectivity, even in the presence of more kinetically accessible anions such as chloride, common to seawater.[1] Furthermore, $CuWO_4$ is a chemically robust material when subjected to the highly oxidizing conditions of PEC OER.[2] Next steps for accelerating research using this, and other, ternary phase oxide materials, is to move beyond

reporting the basic photoelectrochemical measurements to understanding fundamental chemical reaction mechanisms operative in PEC OER on semiconductor surfaces.

In this chapter, the process for PEC OER on $CuWO_4$ thin films is outlined with emphasis on the chemistry of this reaction—the reaction rate and selectivity (determined by controlled-potential coulometry and oxygen-detection experiments). Key challenges are discussed with $CuWO_4$ such as slow kinetics and the presence of an OER-mediating mid-gap state, probed by electrochemical impedance spectroscopy. We propose that this mid-gap state imparts the observed chemoselectivity of OER on $CuWO_4$. Insights into the chemical mechanism of PEC OER on $CuWO_4$ are introduced using Tafel analysis of electrochemical polarization. We measure Tafel slopes of ~161 mV/dec, showing that PEC OER proceeds at a slower rate on $CuWO_4$ than on common electrocatalysts for this reaction. Moreover, the observed photocurrent is independent of the borate buffer concentration, signaling that the buffer plays no role in the rate-determining elementary step of the reaction. Finally, some recent developments are explored such as doping this material with Co (a known electrocatalytically active metal) and coupling it with a transparent manganese phosphate (MnPO) electrocatalyst. We find that introducing Co into the wolframite structure leads to severe recombination of photogenerated charge carriers. However, coupling $CuWO_4$ with MnPO increases the photocurrent density. Despite some of these challenges $CuWO_4$ proves to be a robust, visible light absorbing photoanode that can oxidize water with a high degree of selectivity, and is therefore worthy of further exploration. Even if new compositions emerge that show better reactivity, this material serves as an excellent proving ground for the common challenges in developing ternary-phase, and other compositionally complex materials.

4.2 Light Absorption and Band Structure in $CuWO_4$

In order for a material to effectively function as a visible-light photoanode in a water-splitting PEC cell, it must be able to absorb in the visible region, where the photon flux is highest.[3] Figure 4.1a depicts the absorption spectra of $CuWO_4$ and WO_3 thin films. The absorption onset for $CuWO_4$ is ~550 nm, which corresponds to a band gap of 2.3 eV.

In addition to the band gap energy, the band gap type matters. $CuWO_4$, like most oxides, possesses an indirect band gap, noted by the lack of a sharp absorption, which decreases its light harvesting efficiency. Indeed, the absorptivity coefficient, α, is 6600 cm^{-1} at 400 nm, but decreases to only 1715 cm^{-1} at 500 nm.[2] Although indirect band gap materials may be considered detrimental

for OER, they may still yield high activity photoanodes in nanowires or nanoplatelet morphologies.[4,5] This strategy has worked with reasonable success for α-Fe_2O_3; photoanodes have been produced that are able to yield saturated photocurrent densities on the order of 6.6 mA•cm^{-2}.[4]

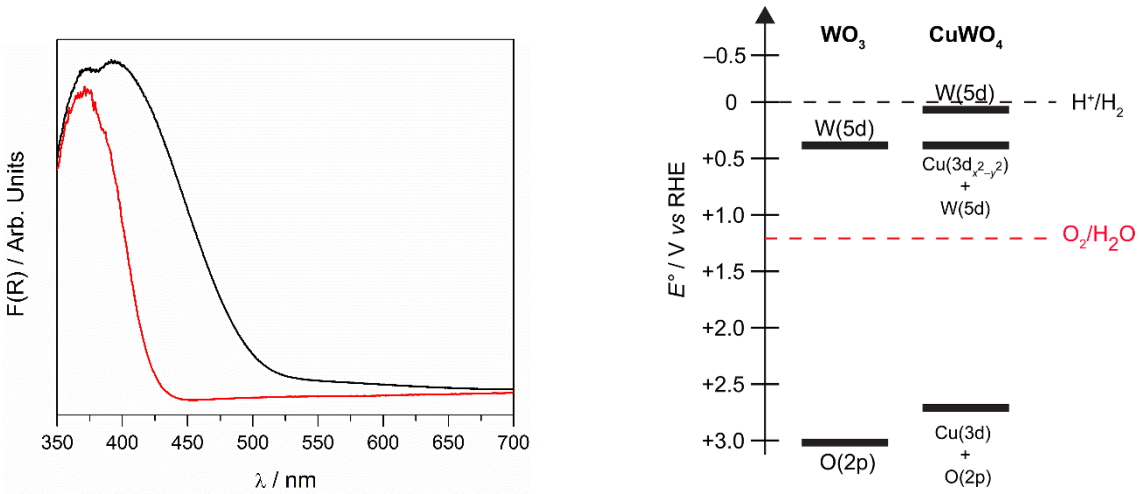

Figure 4.1: a) F(R) plots for a spray pyrolyzed $CuWO_4$ (black) and sol-gel WO_3 (red) thin films deposited onto a FTO coated glass substrate. b) Electronic structures of $CuWO_4$ and WO_3. Band edge potentials are referenced to the reversible hydrogen electrode, RHE.

Upon illumination, electrons are excited from the valence band (VB) to the conduction band (CB). $CuWO_4$ is an n-type semiconductor, so under an anodic bias, the holes left behind in the VB migrate to the surface to carry out oxidation chemistry. In order for OER to occur at low overpotential, the VB holes should lie near the equilibrium potential for the reaction, 1.23 V vs. NHE. Figure 4.1b compares the band edges of $CuWO_4$ and WO_3 with respect to the electrode potentials for OER and HER.

For most metal oxides, the VB is primarily composed of O(2p) levels that lie at ~2.5 – 3 V vs. NHE. Since the VB of most d^0 metal oxides is O(2p) in character, this maximum does not shift significantly between a chemically diverse series of metal oxides. However, there are slight differences in the specific energy of the top of valence bands that arise due to orbital mixing between O(2p) states and metal orbitals. In the case of $CuWO_4$, the VB is shifted upward, rationalized by mixing between Cu(3d) and O(2p) states[2,6] which presents a significant advantage by decreasing the band gap which increases the range of visible light absorption.

The composition of the CB of $CuWO_4$ is hotly debated. Earlier reports relying on first principle calculations[7,8] suggested that the VB was primarily composed of O(2p) states with some

Synthesis method	Film thickness / μm	j_{photo} / mA•cm^{-2} [a]	Electrolyte	Ref.
Electrochemical Deposition	2-3	0.2	0.1 M KPi, pH 7	2
Electrochemical Deposition	0.250 ± 0.050	0.1	0.1 M KPi, pH 7	34
Spin Casting	0.2	0.15	0.1 M KPi, pH 7	1
Spin Casting	0.2	0.3	0.1 M KPi, pH 7.4, 0.14 M NaCl	13
RF Magnetron sputtering	2	~0.19	0.33 M H_3PO_4	14
Spray Pyrolysis	2	0.15	pH 10 Hydrion buffer	15
Spray Pyrolysis	1.5-2	0.19	0.1 M KPi, pH 7	16

a – measured at 1.23V vs. RHE ($E_{RHE} = E_{NHE} + 0.0591$ V • pH)

Table 4.1: PEC metrics for $CuWO_4$ thin films prepared by various methods.

contribution from Cu(3d). This model also proposed a CB dominated by W(5d) states. However, a more recent computational study[9] suggests that Cu(3d) states may also contribute to the bottom of the CB in addition to the top of the valence band. Furthermore, recent experimental evidence indicates that the CB is shifted relative to that of WO_3, which the authors of that work attribute to incorporating Cu(3d) states into the CB.[10] Although the precise contribution of Cu(3d) states to the CB is not fully understood, evidence supporting the VB contribution of Cu(3d) states is compelling.

In Figure 4.1a, the absorption features of $CuWO_4$ below 550 nm (shoulder at 460 nm) suggest two bands—one that has Cu(3d) to W(5d) character, and on that has Cu(3d) to Cu(3d) character.[11] Mott Schottky analysis of electrochemical impedance spectroscopy (EIS) data reveal the two distinct energy levels from which charge transfer to solution occurs, and represents the taking off point for additional electronic structure / chemical reactivity experiments described below.

4.3 Synthesis and Electrochemical Characterization of $CuWO_4$ Thin films for OER

A wide range of syntheses have been developed to yield powders and thin films of $CuWO_4$. Precipitation, solid state synthesis, spray pyrolysis, electrochemical deposition and sol-gel processing have been reported in the literature.[1,2,12–17] Table 1 summarizes key data for PEC OER on $CuWO_4$ thin films prepared by these common techniques. Readers are referred to the original publications for full syntheses. Of these methods, spray pyrolysis is highlighted due to its simplicity and its ease of compositional control.

Spray pyrolysis is an attractive, low-cost means of synthesizing compositionally complex metal-oxide thin films. For this thesis work an automated spray pyrolyzer was constructed to

deposit metal oxide thin films. To grow thin films of $CuWO_4$, first an aqueous precursor of $CuCl_2$ and ammonium metatungstate (AMT) is prepared with equimolar concentrations of Cu^{2+}

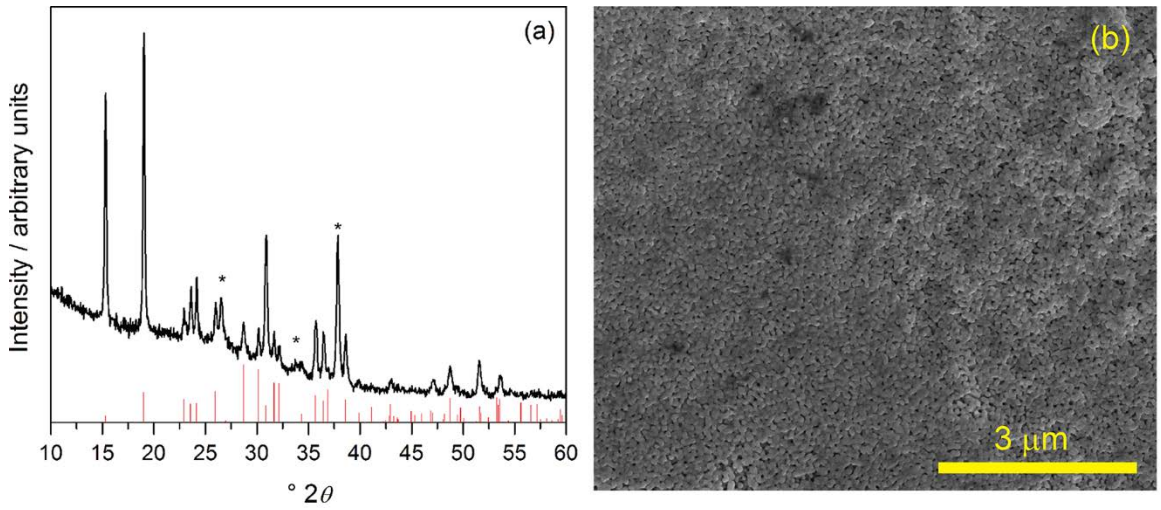

Figure 4.2: a) X-ray diffraction pattern of a $CuWO_4$ film grown via spray pyrolysis on FTO coated glass. * denotes peaks from the FTO substrate. b) Top-down SEM image of a spray pyrolyzed $CuWO_4$ thin film.

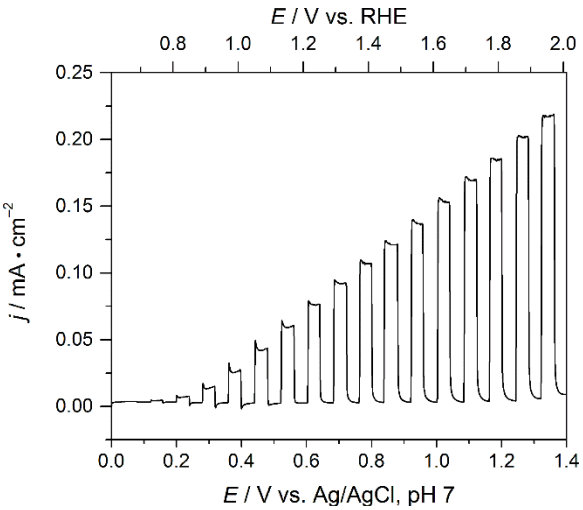

Figure 4.3: CL-LSV for a $CuWO_4$ thin film. 1 sun illumination, 0.1M KB_i, pH 7.

and W^{6+} (0.01 M). Then, an FTO coated glass substrate is placed on a hot plate, and heated to 275°C. Finally, the precursor solution is sprayed onto the heated substrate via a glass nozzle using a deposition pulse of 1 s and a resting pulse of 5 s. During the deposition, the nozzle sweeps from left to right to ensure full and even coverage on the substrate. The 5 s delay between each spray allows the solvent to evaporate between deposition cycles. The following chemical reaction is hypothesized to occur during the course of the deposition:

(Eqn. 4.1) $$12\ CuCl_2(aq) + (NH_4)_6H_2W_{12}O_{40}(aq) + 8\ H_2O(l) \rightarrow 12\ CuWO_4(s) + 6NH_3(g) + 24\ HCl(g)$$

After 100 deposition cycles, an amorphous film is deposited, which is then crystallized upon annealing in a muffle furnace for 1 hour at 550°C. Figure 4.2 depicts the XRD pattern and a top-down SEM image of an annealed $CuWO_4$ film, demonstrating that spray pyrolysis yields phase-pure thin films of $CuWO_4$. Furthermore, these electrodes demonstrate photocurrent densities of 0.06-0.1 mA•cm^{-2} at 1.23 V vs. RHE in a pH 7 0.1 M potassium borate (KB_i) solution, shown in the chopped-light linear sweep voltamogram (CL-LSV) of Figure 4.3.

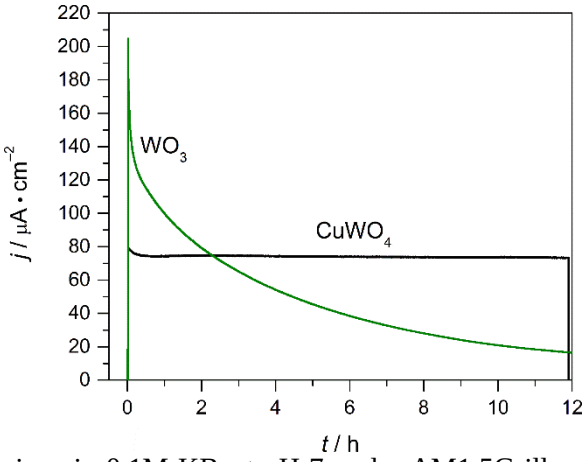

Figure 4.4: j-t curve comparison in 0.1M KB_i at pH 7 under AM1.5G illumination at 100 mW•cm^{-2} for WO_3 (green) and $CuWO_4$ (black). Adapted with permission from ref. 1. Copyright 2013 American Chemical Society.

4.4 Stability and Selectivity for OER in Aqueous Solution

One of the primary requirements for water splitting photoelectrodes is that they be chemically stable during the reaction. $CuWO_4$ demonstrates excellent stability in aqueous solutions with pH 7. Figure 4.4 depicts chronoamperometry (j-t) curves of a $CuWO_4$ photoanode in KB_i buffered water versus WO_3 under 1-sun illumination poised at 1.23 V RHE. We surmise that the improved stability stems from the increase in covalency in the copper oxygen bonds, inhibiting the known acid-base reaction in WO_3 at pH > 5[2,18,19]:

(Eqn. 4.2) $$WO_3\,(s) + H_2O\,(l) \rightarrow 2H^+\,(aq) + WO_4^{2-}\,(aq)$$

$CuWO_4$ electrodes are robust at pH 7, indicating a decrease in Arrhenius acidity. Furthermore, this stability is retained during PEC OER. This behavior is in contrast to WO_3, which is thought to produce peroxo- intermediates during the course of the reaction, which accelerates its degradation.[19–22]

Ideal photoanodes for water oxidation must be selective for OER, especially in the presence of oxidizable chloride (Cl^-) anions since the most abundant source of water is the sea, which is 1.9 wt% chloride.[23] For metal oxides, selectivity for OER can be poor due to the highly oxidizing nature of the O(2p) VB holes, noted by a preference for oxidizing anions from the electrolyte. This effect is particularly pronounced with WO_3.[19,20,22] Indeed, WO_3 demonstrates Faradaic efficiencies as low as 27% depending on the electrolyte used[19], whereas $CuWO_4$ yields near 100% selectivity for OER in the presence of chloride.[1]

4.5 Rates of Hole Transfer to Solution

We have also investigated hole transfer from $CuWO_4$ to solution to better understand how this material functions as an OER catalyst. To probe this matter, Tafel data was collected using steady-state current density measurements under illumination in a pH 7 0.1 M potassium borate (KB_i) solution. A borate solution was selected due to $CuWO_4$'s robust stability in this solution.[1] This data provides a means of assessing the catalytic activity of the electrode surface. By plotting log(j) of measured steady-state current density versus overpotential (η), a straight line is produced that may be modeled by the Tafel equation:

(Eqn. 4.3) $$\eta = \frac{2.3RT}{\alpha n F} \log \frac{j}{j_o}$$

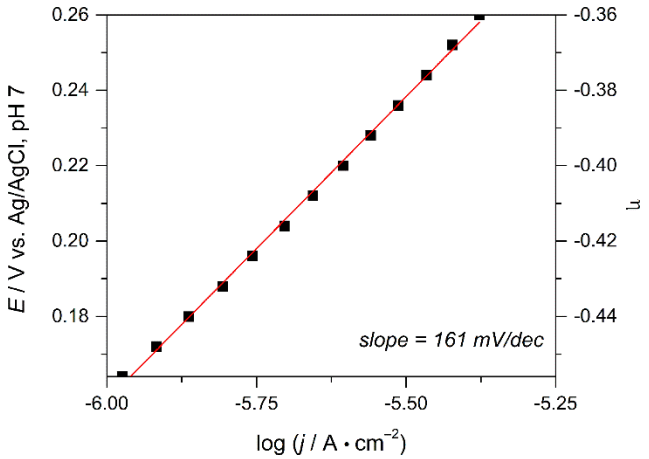

Figure 4.5: Tafel plot with linear fit of $CuWO_4$ under 1-sun illumination in a 0.1 M KB_i, 0.1 M KNO_3 solution at pH 7.

where η is the overpotential ($E_{applied} - E_o$), R is the universal gas constant, T is the absolute temperature (298 K), α the transfer coefficient, n the number of electrons transferred in the rate determining step and F is Faraday's constant. j represents the measured current density and j_o is

the exchange current density. A lower slope indicates a faster reaction rate, with typical electrocatalysts for OER yielding slopes ≤120 mV/dec.[24]

Figure 4.5 shows the Tafel plot for a $CuWO_4$ electrode, first we observe an $\eta < 0$ which is consistent with the behavior exhibited by an n-type photoanode. Because this is a photoanode, the photopotential generated within the semiconductor under illumination allows for water oxidation to take place at applied biases that are lower than the E^o for this reaction.[25] Additionally, because the slope of the Tafel line is >120 mV/dec, it is difficult to precisely define the values of α and n.[25] However, the large Tafel slope (~161 mV/dec) indicates that OER proceeds at a slower rate on $CuWO_4$ than typical electrocatalysts. Furthermore, the photocurrent onset for $CuWO_4$ (see Figure 4.3) takes place at a larger overpotential (~0.7 V RHE) relative to its flat band potential (+0.4 V RHE). Together, these data point to sluggish hole transfer from $CuWO_4$ to the solution. This type of behavior may arise from slow kinetics on the surface, trap states, high resistance within the film or a low concentration of photogenerated holes arriving to the surface. Recent publications indicate that kinetics and poor electron transport through the films may be limiting OER current.[13,15] In addition, we have previously demonstrated in chopped light linear sweep voltammograms of 10% MeOH solutions that the onset of oxidative current takes place at much lower potentials than that of water oxidation.[2] Furthermore, other reports have also demonstrated that improving electron transport through thin films can also provide improvements in photocurrent.[13,15]

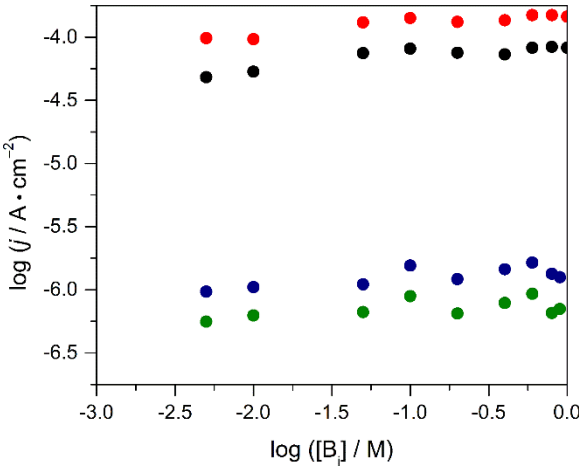

Figure 4.6: log(*j*) vs. log(B_i) plot demonstrating the B_i concentration dependence of photocurrent under 100 mW/cm^2 AM.15G illumination at 1 V (red), 0.6 V (black), 0.22 V (blue) and 0.18 V (green) vs Ag/AgCl. Solutions were all kept at pH 7 and contained 1M $NaNO_3$ to improve solution conductivity.

In addition to hole-transfer rate to solution, we have also investigated the effects of the concentration of borate anion (B_i) in solution on the photocurrent to obtain a reaction order in B_i.

To conduct this experiment, steady-state current densities were measured at different applied potentials under 1-sun illumination in solutions with different concentrations of B_i at pH 7. To improve solution conductivity, all solutions contained 1 M $NaNO_3$. Na-salts were used due to the limited solubility of K-salts at such high concentrations. Additionally, the solution resistance between the working and reference electrode was measured prior to collecting the i-t curves using the iR test function on a CHI 760e bipotentiostat and the variance across solutions was minor (±0.68 Ω). From these experiments summarized in Figure 4.6, we observe a zero-order dependence on B_i concentration at four different applied potentials in the Tafel region and at applied biases under diffusion control. These result indicates that B_i anions do not actively participate in the rate-determining step of OER at pH 7 on $CuWO_4$.

4.6 Mid-Gap State Mediated OER

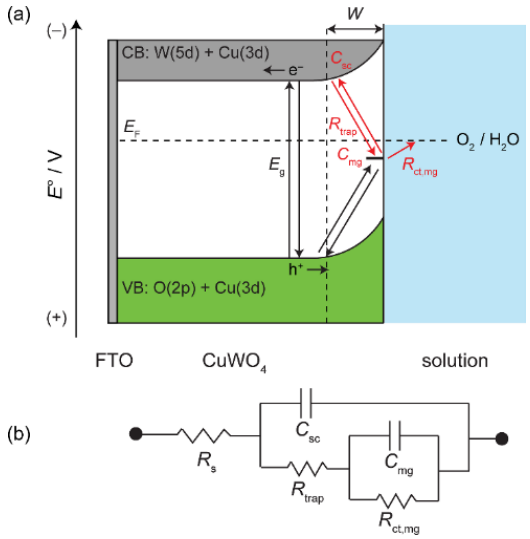

Figure 4.7: a) Proposed physical model for charge-carrier pathways in $CuWO_4$: excitation, mid-gap state trapping, and charge-transfer reactions to solution. W represents the depletion width, and the red arrows correspond to the charge-transfer processes measured by EIS. b) Equivalent circuit model of water oxidation through the mid-gap state. Reproduced with permission from ref. 26. Copyright 2013 the American Chemical Society.

Recently, our group demonstrated that photoelectrochemical water oxidation occurs from a mid-gap electronic state.[26] Electrochemical impedance spectra collected in the dark and under illumination show that the mid gap state is a dark permanent state, not a light induced one. We hypothesize that this state is derived from the Cu($3d_{x2-y2}$) orbital resulting from Jahn-Teller distortion of Cu^{2+}. Cu(3d) states would be strongly localized, and would result in poor carrier transport kinetics which would limit the reaction rate.[27] Unfortunately, due to the limits of EIS

analysis the precise energy of this mid-gap state is not identifiable although data suggests that it lies at a potential >0.801 V vs. RHE.

Furthermore, the mid-gap state may also be responsible for selective water oxidation in the presence of chloride. Because the valence band of $CuWO_4$ lies at a potential of +2.7 V vs. NHE, a photogenerated hole should have sufficient energy to drive a wide variety of oxidation reactions. However, it is possible that during photoexcitation, the presence of mid-gap surface states produces localized holes that are incapable of photooxidizing the chloride anion. Figure 4.7 depicts our proposed physical model for charge carrier pathways in $CuWO_4$. It is observed that if electron transfer occurs from the solution to the mid gap state then the thermodynamic potential of the latter will determine what reactions are thermodynamically favorable to occur on the surface. This hypothesis may explain our observations that even in solutions of 0.1 M NaCl, $CuWO_4$ demonstrates a Faradaic efficiency of near unity for OER.[1] In comparison, WO_3—which possesses an energetically similar valence band but that is only O(2p) in character—demonstrates 0% Faradaic efficiency for OER in a NaCl containing solution.[1,22] This juxtaposition between these two semiconducting photoanodes is unusual; because water is a four electron four proton generating process this makes it a kinetically challenging reaction to perform. By comparison, other anion oxidations such as Cl^- oxidation—which is a two electron process—should be more kinetically accessible reactions. This property makes $CuWO_4$ a particularly attractive candidate as a photoanode for water oxidation.

4.7 Effects of Secondary Phase Co-catalysts on the rate of OER on $CuWO_4$

Although adding co-catalysts has been a successful strategy for improving photocurrent density on WO_3, Fe_2O_3 and $BiVO_4$,[19,28] there is only one report on successfully coupling an OER electrocatalyst with $CuWO_4$:WO_3 composite photoanodes. Adding a solid-state Mn-phosphate (MnPO) co-catalyst improves the photocurrent density of a $CuWO_4$:WO_3 composite electrodes by a factor of 1.5.[29] The authors attribute this increase to the MnPO catalyst facilitating OER on the electrode surface. Interestingly, the MnPO co-catalyst does not absorb visible light which makes it ideal for use with a photoanode. Unfortunately, no data was reported on MnPO loaded onto single-phase $CuWO_4$ electrodes to assess its inherent reactivity.

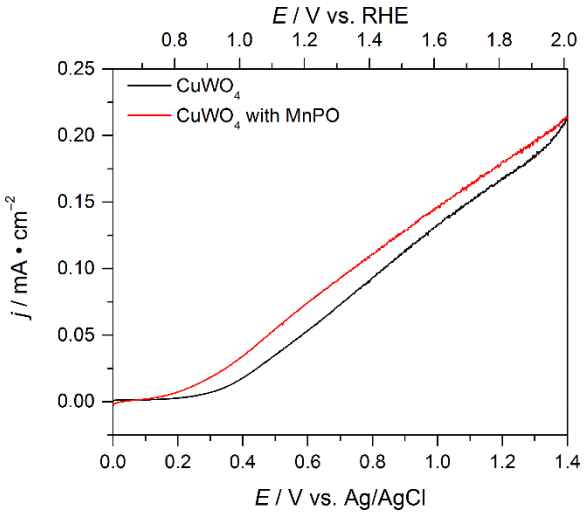

Figure 4.8: LSVs recorded under 100 mW/cm^2 AM1.5G illumination in a pH 7 0.1M KP_i solution for $CuWO_4$ before (black) and after (red) depositing a MnPO catalyst.

To probe the effects of the OER electrocatalyst, we deposited MnPO onto $CuWO_4$ prepared by spray pyrolysis using the reported literature procedures.[29] Figure 4.8 presents LSV traces of a representative electrode under illumination before and after loading the co-catalyst. Notable is that the onset potential for water oxidation is shifted cathodically by ~100 mV. Furthermore, we see a mild increase in photocurrent density upon adding the MnPO electrocatalyst, particularly at low applied bias. Although the shift in onset potential is similar to what has been reported for composite electrodes, the photocurrent enhancement is not improved by 50%. These data suggests that it is the WO_3 that is doing the heavy lifting in the published report, but that adding co-catalysts may be an effective strategy to improve the turnover frequency for water oxidation on $CuWO_4$.

4.8 Synthesis of $Cu_{1-x}Co_xWO_4$

There is one successful report on doping spray-pyrolyzed $CuWO_4$ thin films with iron to improve the photocurrent density in aqueous solution.[16] The iron loading in the $CuWO_4$ film was controlled by varying the concentration of $FeSO_4$ in the precursor solution, and the materials generated in this fashion contain impurities indicating that they are $CuWO_4$:WO_3 composites. The films doped with 0.3 atomic-% Fe demonstrated improved photocurrent density in aqueous solution (from ~0.19 to ~0.25 mA•cm^{-2} at 1.23 V vs. RHE). The authors propose that the improvement in photocurrent is due to an increase in bulk conductivity. In addition to Fe, the

authors propose Mn, Co, Ni and Zn as promising dopant candidates due to their isovalency with Cu. However, we find that adding Zn does not improve photocurrent densities.[30]

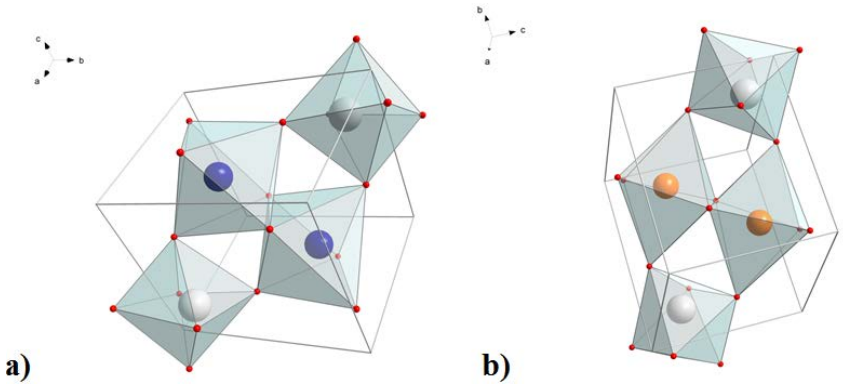

Figure 4.9: a) $CoWO_4$ and b) $CuWO_4$ viewed along the (111) plane. Blue sphere represent Co, Orange are Cu, red are O and white are W.

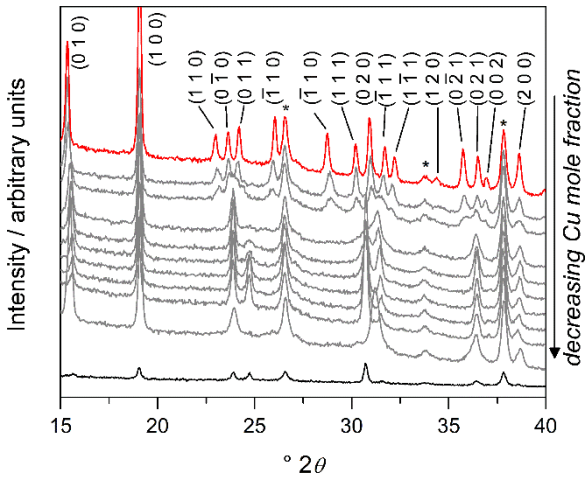

Figure 4.10: XRD patterns for the $Cu_{1-x}Co_xWO_4$ series. From top to bottom: x = 0 (red, pure $CuWO_4$), 0.1, 0.2, 0.3, 0.4, 0.5, 0.6, 0.7, 0.8, 0.9, 1 (black, pure $CoWO_4$). * indicates reflections from the FTO substrate.

To probe the effects that incorporating other transition metals have on the photoelectrochemical behavior of $CuWO_4$, we prepared $Cu_{1-x}Co_xWO_4$ thin films. Co was selected due to the ease of incorporation of Co to form wolframite-phase solid solutions with $CuWO_4$[31] and due to the fact that Co-based oxides and tungstates often demonstrate high catalytic activity towards OER.[32] Because $CoWO_4$ and $CuWO_4$ possess similar crystal structures in addition to similar coordination environments in the solid state (Figure 4.9), it was hypothesized that solid solutions of these materials could be readily formed.

We prepared $Cu_{1-x}Co_xWO_4$ thin films by a spray pyrolysis approach; $Cu(OAc)_2$, $Co(OAc)_2$ and $(NH_4)_6H_2W_{12}O_{40}$ (ammonium metatungstate, AMT) precursors were dissolved in aqueous solution to obtain the desired stoichiometric ratios in Cu:Co:W ([1–x]:x:1). The combined

concentration of Cu^{2+} and Co^{2+} was kept at 10 mM and the concentration of AMT was adjusted to obtain a concentration of 10 mM in W. The Co^{2+}/Cu^{2+} ratios in the precursor solutions determined the Co^{2+}/Cu^{2+} ratios in the resulting thin films. By spraying these solutions onto FTO heated to 275°C and annealing the films at 550°C for 1 hour as previously described, wolframite $Cu_{1-x}Co_xWO_4$ electrodes were obtained; XRD patterns in Figure 4.10 collected on films with a wide range of compositions ($0 \leq x \leq 1$) agree with previous reports in the literature.[31]

Pure $CoWO_4$ electrodes demonstrate significantly higher dark OER activity than $CuWO_4$ electrodes. This behavior is reflected by their low Tafel slopes (~126 mV/dec) and lower overpotential for the electrolysis of water in the dark (Figure 4.11, η_{OER} for $CoWO_4$ is ~300 mV

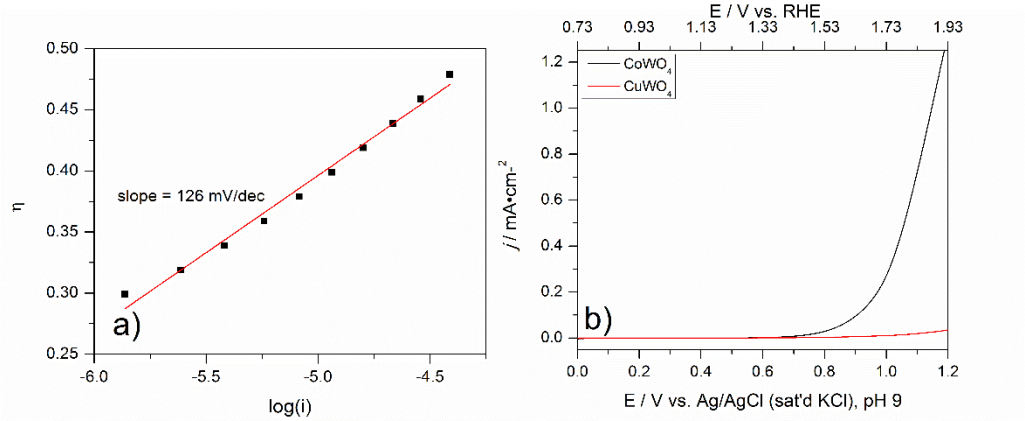

Figure 4.11: a) Tafel plot of a $CoWO_4$ electrode in pH 9 0.1M KB_i aqueous solution. b) Linear sweep voltammograms of $CoWO_4$ and $CuWO_4$ in pH 9 KB_i aqueous solution.

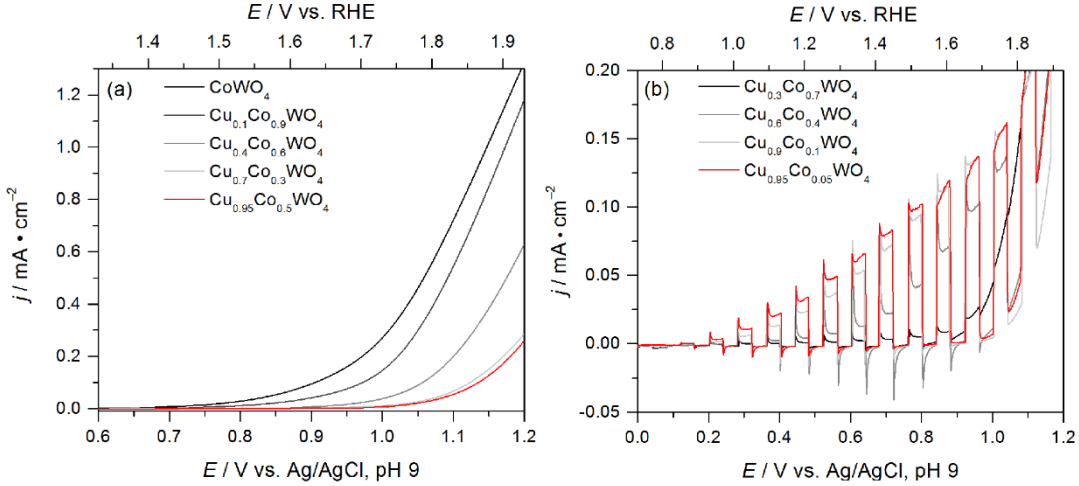

Figure 4.12: a) Dark LSVs of $Cu_{1-x}Co_xWO_4$ series in 0.1M pH 9 KB_i, b) CL-LSVs for select electrodes from $Cu_{1-x}Co_xWO_4$ series under 1-sun illumination.

less than that for $CuWO_4$). These results reflect the much higher dark catalytic activity of $CoWO_4$ versus its Cu counterpart.

Adding Co to form $Cu_{1-x}Co_xWO_4$ films shows three significant effects on the observed photoelectrochemistry in Figure 4.12. First, the onset of electrocatalyzed water oxidation in the dark shifts to lower overpotential with increasing Co concentration (Figure 4.12a). This is not unusual given that $CoWO_4$ has been reported to function as an electrocatalyst for water oxidation.[32] Second, with increasing Co loading, there is a decrease in photocurrent under CL-LSV traces (Figure 4.12b). Finally, there is a significant increase in magnitude of photocurrent transients with increasing Co content as well, in addition to a growth in cathodic photocurrent at lower potentials.

These results suggest that Co behaves as a recombination center, possibly by introducing new trap states, as evidenced by the dramatic increase in photocurrent transients that are observed.

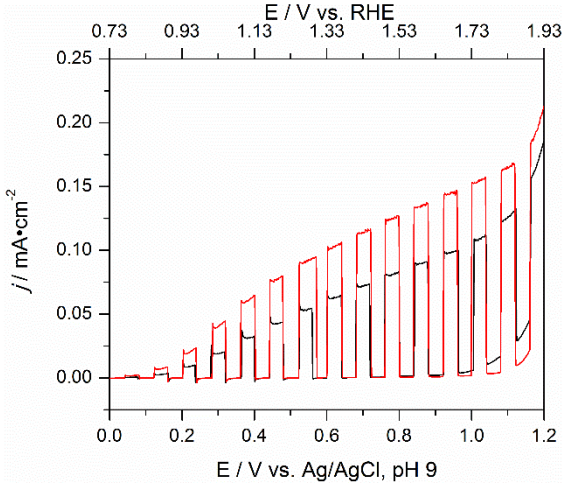

Figure 4.13: CL-LSVs for a $CuWO_4$ electrode before (red) and after (black) depositing a layer of $CoWO_4$ on the surface.

This type of behavior indicates recombination via surface species[33] and/or a decrease in the material's ability to produce delocalized electron-hole pairs. Although photoelectrons are generated, which is observed with the transient spike, they quickly recombine and are unable to be collected to perform useful chemical work.

Finally, the effects of growing $CoWO_4$ directly onto $CuWO_4$ was also investigated. By growing a layer of p-type $CoWO_4$ onto the surface of a $CuWO_4$ thin film, a p-n heterojunction is formed. By placing the p type $CoWO_4$ on the surface,[31] the junction is optimized for electron transfer from solution through the semiconductors and finally to the back contact. We

hypothesized that the electric field generated at the $CuWO_4/CoWO_4$ junction would improve charge separation. Furthermore, the faster OER kinetics on the $CoWO_4$ electrode was predicted to improve overall photocurrent densities by increasing the turnover frequency for OER.

Spray pyrolysis was again employed to produce $CuWO_4/CoWO_4$ layered electrodes. To test the electrochemical behavior of the resulting film, chopped light linear sweep voltammograms were collected on the same $CuWO_4$ electrode before and after growing the $CoWO_4$ on the surface. The CL-LSV data (figure 4.13) reveals that the $CoWO_4$ on the surface effectively reduces the observed photocurrent by 40% at 1.23V vs. RHE from ~100 $\mu A \cdot cm^{-2}$ to ~60 $\mu A \cdot cm^{-2}$. Additionally, an increase in dark current from OER is observed in the layered electrode which confirms the presence of the $CoWO_4$ electrocatalyst on the surface. These data suggest that the $CuWO_4/CoWO_4$ junction effectively behaves as a recombination center and thus probably does not improve charge

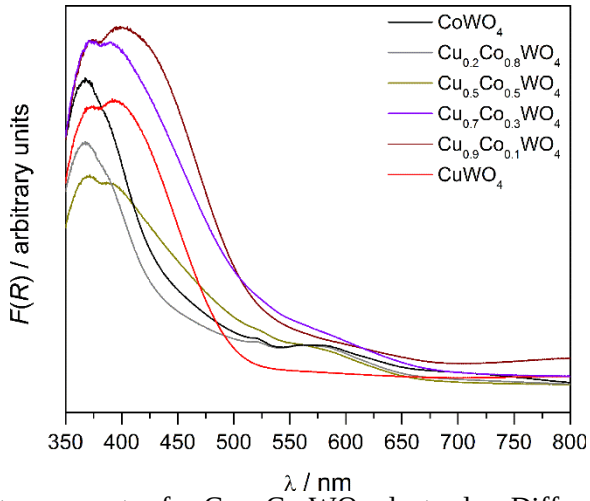

Figure 4.14: Diffuse reflectance spectra for $Cu_{1-x}Co_xWO_4$ electrodes. Differences in absorbance maxima are due to slight differences in film thickness between electrodes.

separation. These effects could result from a mismatch in the semiconductors' band energies or from charge trapping on the Co.

This behavior highlights the need to select dopants carefully for $CuWO_4$. Adding Co into $CuWO_4$ may introduce additional mid-gap 3d states that are highly localized. This proposition is supported by the growth of a d-d transition in the UV-Vis spectra of $Cu_{1-x}Co_xWO_4$ films with increasing Co content, shown in Figure 4.14. These impurity states explain why the photocurrent density decreases with increasing Co loading.

4.9 Conclusions

In this chapter our lab's recent advances in developing $CuWO_4$ photoanodes for PEC OER were discussed. $CuWO_4$ is promising for this application due to its chemical stability at pH 7, small band gap, and high selectivity for water oxidation. However, a few key challenges must be addressed in order to make significant progress with this material: First, Tafel experiments with slopes of ~160 mV/dec collected in aqueous B_i buffered solutions at pH 7 and LSVs collected in aqueous methanol suggest that hole transfer to solution is slow during OER. However, we have also demonstrated that it is possible to improve the kinetics at the electrode surface by incorporating a MnPO co-catalyst. Furthermore, we have demonstrated that in the case of B_i electrolyte solutions at pH 7, B_i plays no active role in the rate-determining step. This data further supports the notion that major improvements in kinetics for OER will stem from surface modifications.

Second, $CuWO_4$ possesses a mid-gap state that dictates hole-transfer rates to water, and may play a crucial role in imparting the excellent observed chemoselectivity for OER over chloride oxidation. This result presents a significant advantage for this material since the most abundant source of water is the sea. Inhibiting chloride oxidation is a critical requirement for any material being considered as a photoanode for an economically viable water splitting PEC cell. Current efforts include exploiting this mid-gap state to probe the chemoselectivity of other oxidation reactions on $CuWO_4$.

Third, we describe incorporating cobalt as a catalyst to improve photocurrent. We observe an increase in charge recombination in $Cu_{1-x}Co_xWO_4$ wolframite solid solutions. Although there is a report on improving the rate of PEC OER through Fe doping,[16] those films contained WO_3 impurities, making it difficult to ascertain how a pure doped $CuWO_4$ electrode would behave. We note that the concentration of Fe used in that case was lower (0.3 at.-%) than the compositions we explored with Co, but we hypothesize that introducing first-row transition metals to $CuWO_4$ may not be a fruitful approach, particularly at concentrations > 5 at.-% because transition metals with partially filled d-shells, such as Co introduce trap states. We have found that even when the d-shell is completely filled as in $Zn_{1-x}Cu_xWO_4$, we still observe decreased performance relative to $CuWO_4$.[30]

To date, the highest performing pure $CuWO_4$ photoanodes demonstrate photocurrent densities of 0.3 mA•cm^{-2} (1.23 V vs. RHE). This value can be increased by incorporating Ag nanowires, resulting in current densities > 1 mA•cm^{-2} (1.5 V vs. RHE).[13] Regardless, this value represents a fraction of the theoretical current densities that $CuWO_4$ can generate based on its absorption spectrum. We predict that future improvements will rely on improving the kinetics at the electrode surface. We have demonstrated that hole transfer to the solution is sluggish, but that it may be improved by adding an appropriate co-catalyst such as MnPO. However, EIS experiments indicate that OER proceeds through a mid-gap state. Consequently, selecting a co-catalyst whose activation potential is compatible with the energy of the mid-gap state will be critical. Future work will need to include a battery of photoelectron spectroscopy measurements to determine the energy of this all-important mid-gap state.

Despite these challenges, significant progress has been made and will continue. Research on $CuWO_4$ for OER is still in its infancy; by comparison, α-Fe_2O_3, another photoanode, took almost a decade to develop. Thus we believe that there is a bright future ahead for $CuWO_4$, and that it can teach us how to think about other complex compositions for PEC OER.

4.10 Experimental

Materials. Boric acid (≥99.5%, Aldrich), cupric acetate (98%, Aldrich), cupric chloride (98%, Aldrich) and cobalt acetate (98+%, Aldrich) were purchased from Sigma-Aldrich. Potassium hydrogen phosphate (K_2HPO_4, 98.0% min., Alfa Aesar), potassium dihydrogen phosphate (KH_2PO_4, 99.0% min., Alfa Aesar), potassium hydroxide (KOH pellets, ≥85.0%, Fisher Chemical) were purchased from Fisher. All reagents were used as purchased without further purification. Solutions were prepared using high purity water (Millipore Milli-Q purification system, resistivity > 18.2 MΩ).

Spray Pyrolysis of Metal Tungstate Electrodes.

$CuWO_4$. To synthesize $CuWO_4$ electrodes via spray pyrolysis, first an aqueous precursor of $CuCl_2$ and ammonium metatungstate (AMT) is prepared with equimolar concentrations of Cu^{2+} and W^{6+} (0.01 M). Then, an FTO coated glass substrate is placed on a hot plate, and heated to 275°C. Finally, the precursor solution is sprayed onto the heated substrate via a glass nozzle using a deposition pulse of 1 s and a resting pulse of 5 s. During the deposition, the nozzle sweeps from

left to right to ensure full and even coverage on the substrate. The 5 s delay between each spray allows the solvent to evaporate between deposition cycles. Finally the electrode is annealed in a muffle furnace at 550°C for 1 hour with a ramp rate and cool down rate of 9.16 °C/min (1 hour ramp up and 1 hour cool down time).

$Cu_{1-x}A_xWO_4$ doped electrodes. . To synthesize $Cu_{1-x}Co_xWO_4$ electrodes via spray pyrolysis, first an aqueous precursor of $Cu(OAc)_2$ + $Co(OAc)_2$ and ammonium metatungstate (AMT) is prepared with equimolar concentrations of (Cu^{2+} + Co^{2+}) and W^{6+} (0.01 M). Depending on the value of x, the concentrations of the Cu^{2+} and Co^{2+} acetate salts was adjusted such that the total concentration of Cu^{2+} + Co^{2+} was 0.01M. After the precursor solution is prepared, an FTO coated glass substrate is placed on a hot plate, and heated to 275°C. Finally, the precursor solution is sprayed onto the heated substrate via a glass nozzle using a deposition pulse of 1 s and a resting pulse of 5 s. During the deposition, the nozzle sweeps from left to right to ensure full and even coverage on the substrate. The 5 s delay between each spray allows the solvent to evaporate between deposition cycles. Finally the electrode is annealed in a muffle furnace at 550°C for 1 hour with a ramp rate and cool down rate of 9.16 °C/min (1 hour ramp up and 1 hour cool down time).

Materials Characterization. X-ray diffraction was recorded on a Bruker D8 Advance diffractometer equipped with a graphite monochromator, a Lynx-Eye detector, and parallel beam optics using Cu Kα radiation (λ = 1.541 84 Å). Patterns were collected using a 0.6 mm incidence slit, with a step size and scan rate of 0.04 °/step and 0.5 s/step, respectively. The $CuWO_4$ phase was identified as JCPDF 72-0616, and $CoWO_4$ was identified as JCPDF 15-0867. All synthesized materials were identified using MDI Jade version 5.0.

UV−vis spectra were recorded using a Cary 5000 spectrophotometer (Agilent) equipped with an external diffuse reflectance accessory. Spectra were recorded in reflectance mode and transformed mathematically into the Kubelka-Munk function, F(R).

Scanning electron microscopy (SEM) images were collected using an FEI Nova Nanolab SEM/focused ion beam (FIB) instrument with an accelerating voltage of 10 kV, WD of 5 mm and beam current of 0.54 nA.

Photoelectrochemistry. Photoelectrochemistry was performed using a CH Instruments 660 C electrochemical workstation. All PEC measurements were performed in custom-built

cells with quartz viewing windows. Three-electrode voltammetry experiments were performed using the working $Cu_{1-x}Co_xWO_4$ thin-film photoanode, a Ag/AgCl (saturated KCl) reference electrode, and a Pt wire counter electrode. The supporting electrolyte in the PEC experiments was either 0.1 M KB_i at pH 7 or 9, or 0.1M KP_i buffered to pH 7. Unless specified otherwise, a 1 cm^2 area of the working electrode from the back side (glass side) was irradiated through a quartz window. The light source was a Newport-Oriel 150W Xe arc lamp fitted with an AM1.5G simulating solar filter (Newport). The lamp power was adjusted to 100 $mW \cdot cm^{-2}$ (except for O_2 detection experiments described below) using an optical power meter (Newport 1918-R) equipped with a thermopile detector (Newport 818P-015-19).

Determination of Reaction Order in B_i Electrolyte. Steady-state current densities were measured at different applied potentials (0.18, 0.2, 0.62 and 1V vs sat'd Ag/AgCl reference) under 1-sun illumination in solutions with different concentrations of B_i at pH 7. The concentrations of B_i solutions employed spanned 3 orders of magnitude (0.001 to 1M NaB_i). The measurements were collected over 5 minutes and the last 200s of the measurement was averaged to obtain the steady state current. It was observed that during the last 200s of most measurements the current variation was no more than ~1 μA. To ensure steady state, all solutions were stirred at 700 RPM during the course of the experiment. To improve solution conductivity, all solutions contained 1 M $NaNO_3$. Na-salts were used due to the limited solubility of K-salts at such high concentrations. Additionally, the solution resistance between the working and reference electrode was measured prior to collecting the i-t curves using the iR test function on a CHI 760e bipotentiostat and the variance across solutions was minor (±0.68 Ω).

Tafel experiments Under Illumination. Tafel experiments were conducted under illumination to gauge the catalytic activity of $CuWO_4$ thin films. For all measurements the solution employed was 0.1M KB_i at pH 7 with 0.1M KNO_3 added to improve solution conductivity and reduce diffuse double layer effects. Data was collected by measuring the steady state photocurrent of $CuWO_4$ electrodes at various applied potentials under 1 sun illumination. All measurements were performed while stirring to ensure that a steady state was reached. Currents were measured over 20 minutes and steady state currents were

extracted by averaging the steady state current over the last 200s. In between controlled potential coulometry experiments the cell was left to equilibrate at OCP for 5 minutes.

Tafel experiments in the dark. Tafel experiments were conducted in the dark to gauge the catalytic activity of $CoWO_4$ thin films as electrocatalysts for OER. Data was collected by measuring the steady state current of $CoWO_4$ electrodes at various applied potentials. The solution employed for these measurements was 0.1M KB_i buffered at pH 9. All measurements were performed while stirring to ensure that a steady state was reached. Currents were measured over 20 minutes and steady state currents were extracted by averaging the steady state current over the last 200s. In between controlled potential coulometry experiments the cell was left to equilibrate at OCP for 5 minutes.

4.11 References

(1) Yourey, J. E.; Pyper, K. J.; Kurtz, J. B.; Bartlett, B. M. *J. Phys. Chem. C* **2013**, *117*, 8708.
(2) Yourey, J. E.; Bartlett, B. M. *J. Mater. Chem.* **2011**, *21* (21), 7651.
(3) NREL. Reference Solar Spectral Irradiance: ASTM G-173 http://rredc.nrel.gov/solar/spectra/am1.5/astmg173/astmg173.html (accessed Jan 23, 2016).
(4) Grätzel, M. *Nature* **2001**, *414*, 338.
(5) Sivula, K.; Le Formal, F.; Grätzel, M. *ChemSusChem* **2011**, *4* (4), 432.
(6) Kihlborg, L.; Gebert, E. *Acta Crystallogr. Sect. B Struct. Crystallogr. Cryst. Chem.* **1970**, *26*, 1020.
(7) Khyzhun, O. Y.; Strunskus, T.; Cramm, S.; Solonin, Y. M. *J. Alloys Compd.* **2005**, *389*, 14.
(8) Khyzhun, O. Y.; Bekenev, V. L.; Solonin, Y. M. *J. Alloys Compd.* **2009**, *480* (2), 184.
(9) Lalić, M. V.; Popović, Z. S.; Vukajlović, F. R. *Comput. Mater. Sci.* **2011**, *50* (3), 1179.
(10) Gaillard, N.; Chang, Y.; Braun, A.; DeAngelis, A. *Mater. Res. Soc. Symp. Proc.* **2012**, *1446*, 19.
(11) Dey, S.; Ricciardo, R. A.; Cuthbert, H. L.; Woodward, P. M. *Inorg. Chem.* **2014**, *53*, 4394.
(12) Hill, J. C.; Choi, K.-S. *J. Mater. Chem. A* **2013**, *1*, 5006.
(13) Zhang, H.; Yilmaz, P.; Ansari, J. O.; Khan, F. F.; Binions, R.; Krause, S.; Dunn, S. *J. Mater. Chem. A* **2015**, *3*, 9638.
(14) Chang, Y.; Braun, A.; Deangelis, A.; Kaneshiro, J.; Gaillard, N. *J. Phys. Chem. C* **2011**, *115*, 25490.
(15) Gaillard, N.; Chang, Y.; Deangelis, A.; Higgins, S.; Braun, A. *Int. J. Hydrogen Energy* **2013**, *38*, 3166.
(16) Bohra, D.; Smith, W. A. *Phys. Chem. Chem. Phys.* **2015**, *17* (15), 9857.
(17) Hill, J. C.; Ping, Y.; Galli, G. a.; Choi, K.-S. *Energy Environ. Sci.* **2013**, *6*, 2440.
(18) Heumann, T.; Stolica, N. *Electrochim. Acta* **1971**, *16*, 1635.
(19) Lhermitte, C. R.; Verwer, J. G.; Bartlett, B. M. *J. Mater. Chem. A* **2016**, *4*, 2960.
(20) Mi, Q.; Zhanaidarova, A.; Brunschwig, B. S.; Gray, H. B.; Lewis, N. S. *Energy Environ. Sci.* **2012**, *5* (2), 5694.
(21) Reyes-Gil, K. R.; Wiggenhorn, C.; Brunschwig, B. S.; Lewis, N. S. *J. Phys. Chem. C* **2013**, *117*, 14947.
(22) Hill, J. C.; Choi, K. *J. Phys. Chem. C* **2012**, *116* (14), 7612.
(23) Greenwood, N.; Earnshaw, A. *Chemistry of the Elements*; Butterworth-Heinemann: Boston, 1997.
(24) Bediako, D. K.; Surendranath, Y.; Nocera, D. G. *J. Am. Chem. Soc.* **2013**, *135* (9), 3662.

(25) Norio Sato. *Electrochemistry at Metal and Semiconductor Electrodes*, First Edit.; Elsevier: Amsterdam, 1998.
(26) Pyper, K. J.; Yourey, J. E.; Bartlett, B. M. *J. Phys. Chem. C* **2013**, *117*, 24726.
(27) Bharati, R.; Shanker, R.; Singh, R. A. *Pramana* **1980**, *14*, 449.
(28) Seabold, J. A.; Choi, K.-S. *J. Am. Chem. Soc.* **2012**, *134* (4), 2186.
(29) Nam, K. M.; Cheon, E. A.; Shin, W. J.; Bard, A. J. *Langmuir* **2015**, *31* (39), 10897.
(30) Yourey, J. E.; Kurtz, J. B.; Bartlett, B. M. *Inorg. Chem.* **2012**, *51*, 10394.
(31) Naik, S.; Salker, A. *Catal. Commun.* **2009**, *10* (6), 884.
(32) Jia, H.; Stark, J.; Zhou, L. Q.; Ling, C.; Sekito, T.; Markin, Z. *RSC Adv.* **2012**, *2* (29), 10874.
(33) Dotan, H.; Sivula, K.; Grätzel, M.; Rothschild, A.; Warren, S. C. *Energy Environ. Sci.* **2011**, *4* (3), 958.
(34) Hill, J. C.; Ping, Y.; Galli, G. A.; Choi, K.-S. *Energy Environ. Sci.* 2013, 6, 2440.

Chapter 5

Controlling the Growth of Thin Films of Ternary Metal Oxides $PbCrO_4$ and $BiVO_4$ Using Chelating Agents: Applications as Water Oxidation Photocatalysts

Portions of this chapter are in preparation for publication:
C. R. Lhermitte, J. E. Yourey, B. M. Bartlett, *Exploiting the Chelation Effect: Solubilizing Incompatible Metal Salts to Yield Thin Films of Ternary Phase Metal Oxides,* in preparation.

5.1 Introduction

The previous chapters of this thesis have dealt with obtaining a mechanistic understanding of how metal oxide materials can catalyze water oxidation. With WO_3, it has been demonstrated that the stability at pH ≥7 and selectivity for OER of acidic metal oxides can be dramatically improved with the growth of an appropriate co-catalyst on the electrode surface. However, in the case of WO_3, it still demonstrates limited visible light absorption due to its large bad gap of 2.7 eV. Because visible light absorption is one of the key metrics for developing an efficient solar energy powered photocatalyst, we sought to develop new, smaller band gap phases of metal oxides.

Ternary metal oxides have garnered significant attention for their applications as photocatalysts over the last few years. With $CuWO_4$, we have demonstrated that it is possible to develop new phases that demonstrate improved light absorption, chemical stability and selectivity towards OER versus their binary counterparts.[1,2] However, we have also demonstrated that the introduction of first row transition metals can be a double edged sword that can increase light absorption, but also increase photo generated charge carrier recombination, ultimately leading to decreased saturated photocurrent densities.[1] As a result, we sought to investigate new ternary phases that contained metal cations that had either completely full (d^{10}) or empty d-shells (d^0) to avoid the potential formation of trap states.

For the development of new materials we drew inspiration from $BiVO_4$ which has demonstrated significant promise as a visible light photocatalyst for OER. This material is comprised of Bi^{3+}, which has a full d-shell and V^{5+} which is a d^0 first row transition metal. Furthermore, it demonstrates high visible light absorption due to a direct band gap transition which yields an absorptivity coefficient of 10^5 cm^{-1} at 460 nm,[3] in addition to high catalytic activity for OER when loaded with the appropriate co-catalysts.[4] Using $BiVO_4$ as a model we sought to explore new phases that also contained a combination of d^{10} and d^0 transition metal oxides.

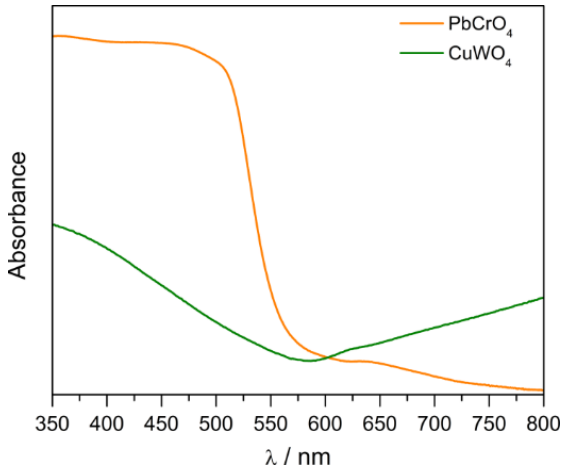

Figure 5.1: Absorbance spectra of $PbCrO_4$ (orange) and $CuWO_4$ (green). Despite having similar band gaps, the $PbCrO_4$ demonstrates a sharp onset of light absorption due to its direct band gap. Figure adapted with permission from ref. 8.

$PbCrO_4$ has emerged as a promising material for applications as a photocatalyst for OER. It possesses a direct band gap of 2.2 eV[5,6] and demonstrates a sharp absorption onset beginning at 560 nm with an absorption coefficient of 2400 cm^{-1} at 516 nm.[7] Figure. 5.1 depicts the absorption spectrum of $PbCrO_4$, a direct band gap material, versus $CuWO_4$, an indirect band gap semiconductor. Due to its direct band gap, $PbCrO_4$ demonstrates a sharp onset of light absorption in addition to a larger absorption maximum. Furthermore, because the top of its valence band is primarily composed of Pb 6s and O 2p orbitals, it lies at a thermodynamically favorable position to carry out water oxidation under illumination.[7] Finally, suspensions of $PbCrO_4$ powders in aqueous solution have demonstrated catalytic photo-oxidation of water in the presence of an IO_3^- electron acceptor.[8,9] However, to date, there have been no reports on synthesizing thin film photoelectrodes of this material.

Spray pyrolysis has emerged as a simple high throughput technique for the production of a wide variety of thin film materials[10]. It provides the benefits of low cost, simplicity and rapid

production of thin films[10]. However, this deposition technique requires precursor solutions that contain fully dissolved metal cations in order to obtain the respective metal oxide thin films. This chapter presents a novel synthetic route using the chelating agent, ethylenediaminetetraacetic acid (EDTA), to stabilize metal salt precursors. The resulting precursor solution can then be deposited onto a substrate using spray pyrolysis to yield a thin film metal oxide. The synthesis of $PbCrO_4$ thin films is highlighted as an example of a novel complex ternary oxide using this technique. Furthermore, this chapter also represents the first report on the electrochemistry and catalytic activity towards OER of thin film electrodes of $PbCrO_4$. Finally, the scope of this synthesis is further expanded by applying it towards the production of thin films $BiVO_4$ photoelectrodes to use as water oxidation catalysts.

5.2 Chelating Metal Cations to Stabilize Precursor Solutions for Spray Pyrolysis

Thin film deposition of ternary metal oxides remains challenging. While it is possible to yield powders of ternary metal oxides using co-precipitation or solid states methods,[8] these are often impractical or difficult to apply towards the production of thin films. The generation of thin films often necessitates the formation of stable precursor solutions. However, the mixing of many metal salt precursors will often initiate a salt metathesis reaction which produces an amorphous or crystalline powder from solution. The resulting mixture is often incompatible with many thin film techniques that require fully dissolved precursors such as spray pyrolysis and spin coating.

In the case of $PbCrO_4$, if a Pb^{2+} and $(CrO_4)^{2-}$ salt—such as $Pb(NO_3)_2$ and $(NH_4)_2CrO_4$—are mixed together they will react in the following manner:

(Eqn. 5.1) $$Pb(NO_3)_2\ (aq.) + (NH_4)_2CrO_4\ (aq.) \rightarrow PbCrO_4\ (s) + 2(NH_4)^+\ (aq.) + 2(NO_3)^-\ (aq.)$$

Because of this precipitation, a solution containing simple salts of the precursors is not compatible with spray pyrolysis. However, reacting $Pb(NO_3)_2$ with the ammonium salt of ethylenediamine tetra acetic acid (ammonium edetate, $(NH_4^+)_4EDTA$) prior to mixing the resulting Pb^{2+} solution with the $(CrO_4)^{2-}$ solution yielded the following reaction:

(Eqn. 5.2) $$(NH_4^+)_4EDTA\ (aq.) + Pb(NO_3)_2\ (aq.) \rightarrow (PbEDTA)(NH_4^+)_2\ (aq.) + 2\ NO_3^-\ (aq.) + 2\ NH_4^+\ (aq.)$$

We hypothesized that the strong chelation effect (binding constant of EDTA for Pb^{2+}, $\log(K_f) = 18$)[11] would prevent the release of chelated Pb^{2+} cations which would prohibit them from reacting with the CrO_4^{2-} once the two solutions are mixed. Indeed when a solution containing $Pb(NO_3)_2$ and EDTA was added to a solution containing $(NH_4)_2CrO_4$, no precipitate was formed. Furthermore, the resulting yellow precursor solution was translucent and no trace of precipitate was observed even after two weeks.

Once the clear yellow precursor solution was obtained, it was sprayed onto fluorinated tin oxide (FTO) coated glass substrates. The electrodes were sprayed using a custom built apparatus onto a substrate heated to 275°C using a 1 s spray pulse followed by a 10 s delay to allow the solvent to evaporate. After spraying, the electrodes were then annealed at 500°C for 2 hours.

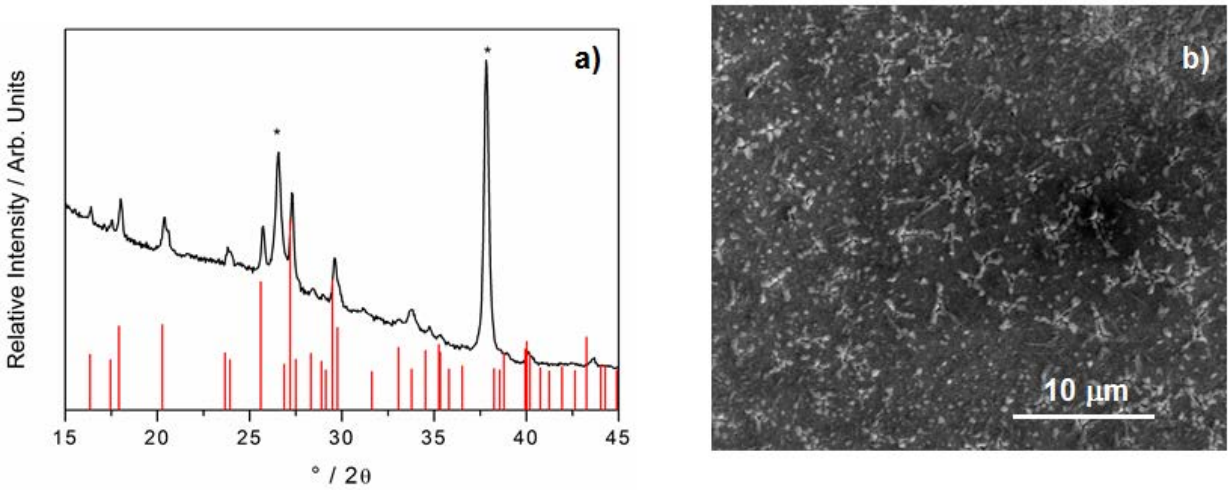

Figure 5.2: a) Powder X-ray diffraction pattern of a spray pyrolyzed $PbCrO_4$ thin film deposited onto FTO coated glass. * indicate reflections from the underlying FTO substrate. Red vertical lines indicate predicted reflection planes for $PbCrO_4$. b) Top down SEM image of a $PbCrO_4$ thin film grown on an FTO coated glass substrate.

Figure 5.2a depicts the powder X-ray diffraction (XRD) pattern of a $PbCrO_4$ thin film. The only reflection planes observed are those for $PbCrO_4$ and the underlying conductive fluorinated tin oxide (FTO) layer. Top down SEM images (Figure 5.2b) reveal a smooth and bumpy surface that is peppered with small holes. The holes in the film may have resulted from excess EDTA combusting or residual solvent boiling off of the film during annealing.

To elucidate the role of the EDTA, the concentration of EDTA was varied in the precursor solution and the stability of the resulting solution was observed. Changing the equivalents from 1 to 1.5 eq. of EDTA per metal (2 and 3 equivalents of EDTA total) did not affect the purity of the

films since no impurity phases were observed in the resulting XRD data (Figure C.1). Furthermore, in each case a stable precursor solution was formed and no precipitate was observed. However, the color of the amorphous films was different. The electrodes synthesized with greater equivalents of EDTA had a purplish hue while those with less EDTA were more whitish in appearance immediately after spraying at 275°C. We hypothesize that the purplish hue may result from the formation of Cr^{3+} in the form of $Cr(OH)_6(NO_3)_3$ or $H[Cr(C_{10}H_{12}N_2O_8)\text{-}(H_2O)]$ (EDTA bound Cr^{3+}).[12] This complex could result from the reduction of Cr^{6+} to Cr^{3+} via the oxidation of EDTA at higher temperatures. However, after annealing at 500°C all electrodes were converted to the yellow $PbCrO_4$ phase.

The effect of chelation of the different metal cations (Cr vs. Pb) on the stability of the resulting precursor solution was also evaluated. In these experiments EDTA was added to either only the Cr^{6+} solution or the Pb^{2+} solution. Solutions where EDTA was only added to the Pb^{2+} precursor solution prior to mixing resulted in stable mixtures once the Pb^{2+} solution was added to the CrO_4^{2-} solution. This was consistent when 1, 1.5 and 2 eq. of EDTA was added to the Pb^{2+} solution and indicates that the EDTA is effective at preventing the Pb^{2+} from reacting with the CrO_4^{2-} to precipitate $PbCrO_4$. Furthermore, if EDTA is only added to the Cr^{6+} containing vial and then the Pb^{2+} solution is mixed in a white precipitate forms initially but then rapidly dissolves to yield a translucent yellow solution. The observed precipitate is likely $PbO{\bullet}xH_2O$ since the pH of the solution is alkaline (pH ~9) due to the addition of NH_4OH to deprotonate the EDTA. To test if the increased pH can dissolve any $PbCrO_4$ that forms, $PbCrO_4$ was synthesized via co-precipitation from a mixture of $Pb(NO_3)_2$ and $(NH_4)_2(CrO_4)$. The pH of the suspension was then increased incrementally from 3.45 to 10. As the pH was increased, none of the solid dissolved and it turned a bright orange color which is a result of the conversion from $PbCrO_4$ to the basic Pb_2CrO_5. This indicates that the dissolution of the $PbCrO_4$ to form $[Pb(OH)_4]^{2-}$ and CrO_4^{2-} in the presence of excess OH^- anions does not take place at these pH values. However, it has been demonstrated in the literature that at higher pH values a hydrated lead oxide will precipitate from a lead salt solution.[13] Because a white solid is first formed then dissolved after the addition of the $Pb(NO_3)_2$ solution to the $(NH_4)_2CrO_4$ solution, we suspect that this solid is a hydrated lead oxide that can then be dissolved to form the EDTA bound and water soluble lead complex. In the solid phase, the hydrated Pb oxide cannot react rapidly with the CrO_4^{2-} in solution and will react preferentially with the EDTA in solution due to the latter's high binding affinity for Pb^{2+}.

5.3 Electrochemistry of $PbCrO_4$ Thin films and Mechanism of Surface Passivation

$PbCrO_4$ has been demonstrated to function as a powder photocatalyst for water oxidation.[8,9] Furthermore, $PbCrO_4$ is composed of metal cations that have either a full (Pb^{2+}, $d^{10}s^2$) or empty (Cr^{6+}, d^0) d shell which can reduce the probability of forming trap states within the band gap.[1] Ternary oxides possessing this type of electronic structure, such as $BiVO_4$, have recently emerged

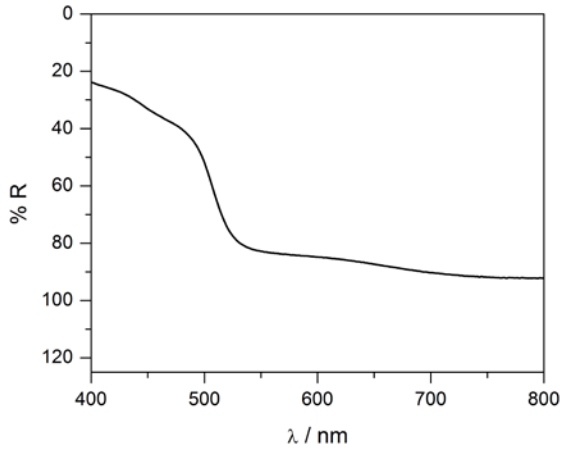

Figure 5.3: %R plot of a spray pyrolyzed $PbCrO_4$ thin film.

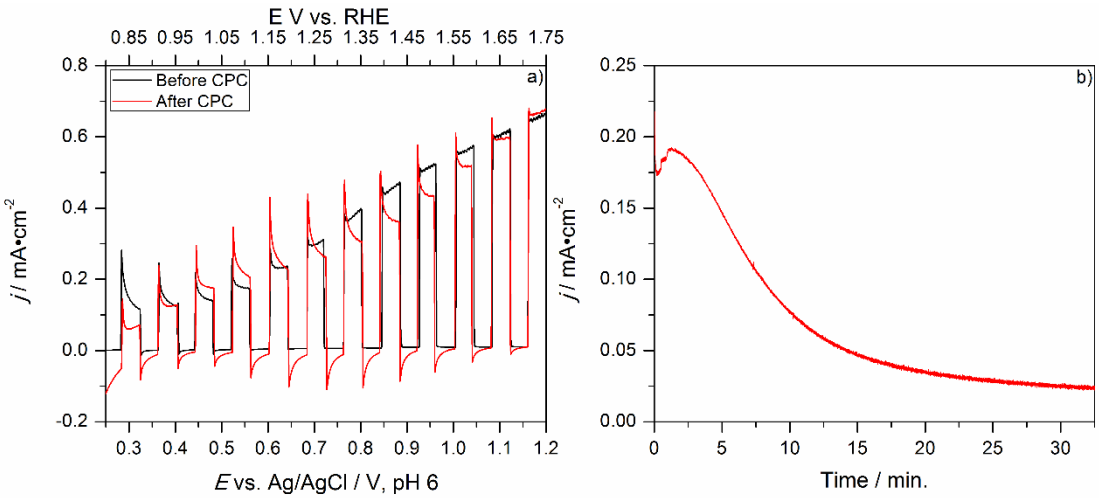

Figure 5.4: a) CL-LSVs under 1 sun illumination in pH 6 0.1M KP_i of a $PbCrO_4$ thin film before/after bulk electrolysis under 1 sun illumination. b) Bulk electrolysis of the same $PbCrO_4$ thin film in 0.1M KP_i, pH 6.

as promising candidates for water oxidation and these electrodes typically exhibit strong visible light absorption and large photocurrent densities.[2,14,15]

To date, there have been no reports on the synthesis of thin films of $PbCrO_4$ for application as a photoelectrode. To test the photoanode properties of $PbCrO_4$, electrodes were synthesized using spray pyrolysis and tested using a series of electrochemical and optical measurements. The

%R plot constructed from reflectance data (Figure 5.3) of the $PbCrO_4$ thin films displays a sharp absorption onset at ~550 nm which is reflective of this material's 2.2 eV band gap and reveals $PbCrO_4$'s high light absorption efficiency. Chopped light linear sweep voltammograms (CL-LSV) indicate that these electrodes produce an anodic photocurrent under illumination. Furthermore, changing the equivalents of EDTA used in the synthesis of the films does not significantly affect the maximal current densities beyond 2 equivalents of EDTA per metal. The resulting optimized electrodes demonstrate photocurrent densities of 0.3-0.5 $mA \cdot cm^{-2}$ at 1.23V vs. RHE in a pH 6 0.1M KP_i aqueous solution (Figure 5.4a).

To test the photoelectrochemical stability of the electrodes in aqueous solution, controlled potential coulometry (CPC) under illumination was performed (Figure 5.4b). These experiments reveal that the photocurrent decreases with time which may result from photodegradation or surface passivation of the film. CL-LSVs collected before and after the bulk electrolysis experiment indicate the presence of new photocurrent transients (Figure 5.4a). However, after prolonged bulk electrolysis the electrode material does not appear to be physically removed from the surface by eye. Thus we hypothesize that the decrease in photocurrent over time may result from the formation of a surface passivation layer.

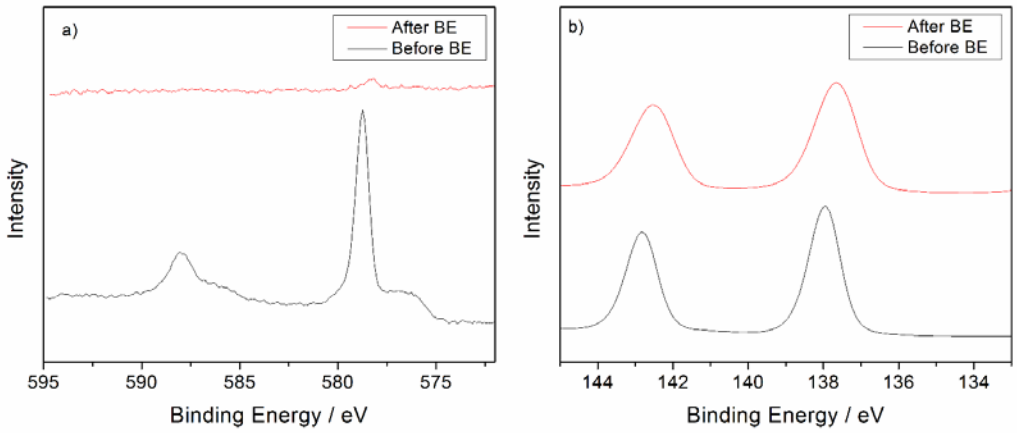

Figure 5.5: XPS spectra of a $PbCrO_4$ thin film before (black) and after (red) a bulk electrolysis experiment under 1 sun illumination in pH 6 0.1M KP_i. a) Cr 2p spectrum b) Pb 4f spectrum.

To probe this question further, XPS data were collected before and after bulk electrolysis under illumination. Figure 5.5 depicts the disappearance of the Cr 2p signal in addition to a broadening of the Pb 4f signal in the XPS after a controlled potential coulometry experiment under illumination. These results suggest that an internal process of the following form may take place:

(Eqn. 5.3) $PbCrO_4$ (s.) + 2 H_2O (l.) → PbO_2 (s.) + H_2CrO_4 (aq.) + $2e^-$

The absence of a Cr 2p signal post electrolysis reveals that Cr has most likely been stripped from the surface during the course of the experiment. Furthermore, the broadening of the Pb 4f signal to lower binding energies is consistent with previously reported spectra of PbO_2.[16,17] These results suggest that a Pb^{4+} passivation layer is forming with the concurrent yield of a water soluble CrO_4^{2-} species. Although XPS provides no information into the removed Cr species' oxidation state, predicted Pourbaix diagrams (Figure C.2) of this material suggest that at strongly anodic potentials Cr is released as CrO_4^{2-} in solution.[18]

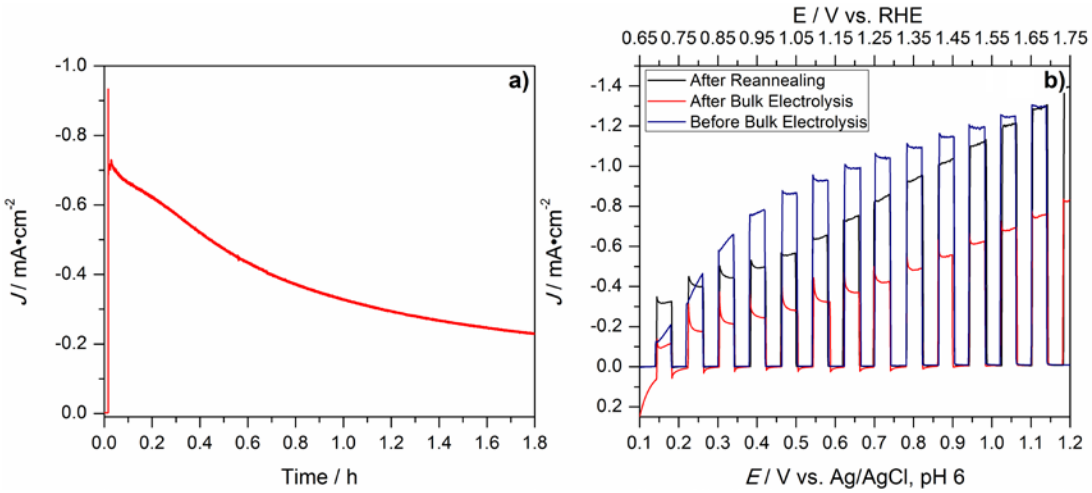

Figure 5.6: a) Bulk electrolysis of a $PbCrO_4$ electrode in a 10% MeOH v/v 0.1M KP_i (pH 6) solution under 1 sun illumination. b) CL-LSVs of the same $PbCrO_4$ electrode in the same solution before (blue) and after (red) the bulk electrolysis experiment. (black) trace demonstrates the chopped light response of the same electrode after reannealing at 500°C.

Due to the slow kinetics of water oxidation, the internal redox processes of the $PbCrO_4$ film—that is, CrO_4^{2-} release into solution and Pb^{2+} oxidation—may out-compete OER, which would result in the formation of a passivation layer on the surface. To test this hypothesis, controlled potential coulometry was performed under 1 sun illumination using a $PbCrO_4$ working electrode poised at 1.23V vs. RHE in a 10% (v/v) methanol aqueous solution (Figure 5.6a). An aqueous solution containing methanol was selected since methanol is a more effective hole scavenger than water[19,20] and thus methanol oxidation was suspected to be more kinetically competitive versus $PbCrO_4$'s self-oxidation. Under these conditions, the rate of photocurrent decay is drastically slower and the photocurrent appears to stabilize after 1.5 hours near a value of 200 µA•cm^{-2}. Additionally, although CL-LSVs in the same methanol solution reveal a loss in net photocurrent, some of the photocurrent can be recovered by re-annealing the electrode at 500°C

(Figure 5.6b). These results indicate that $PbCrO_4$ electrodes have potential as photoelectrodes for organic oxidation reactions.

5.4 Surface Stabilization of $PbCrO_4$ Thin Films Using Protective Layers

In an attempt to stabilize $PbCrO_4$ electrodes for photoelectrochemical OER a few different surface treatments were attempted. The first method involved the growth of the OER electrocatalyst Cobalt Phosphate (CoP_i). We and others have demonstrated that electrocatalysts can be used effectively to stabilize metal oxide surfaces in addition to improve their catalytic efficiency for OER.[4,21,22] As a result, we sought to deposit the CoP_i electrocatalyst on the surface of $PbCrO_4$. CoP_i was selected due to its stability and catalytic activity during the electrolysis of water. Furthermore, this material can be deposited anodically by oxidizing a 0.5 mM Co^{2+} containing KP_i solution at pH 7.[22] Finally CoP_i has been used to stabilize unstable semiconducting materials such as Si and WO_3 which allowed their prolonged use during the photooxidation of water.[22–24]

CoP_i was deposited onto $PbCrO_4$ thin film electrodes using a photoelectrochemical deposition. Briefly, the $PbCrO_4$ electrode was immersed in 0.1M KP_i solution buffered to pH 7 that also contained 0.5 mM $Co(NO_3)_2$. The electrode was poised at 0.862 V vs. RHE and illuminated with 1 sun for one hour. CL-LSVs in a fresh solution of 0.1M pH 6 KP_i are shown in Figure 5.7a. The current voltage profile of the $PbCrO_4$-CoP_i electrode demonstrates a noticeable increase in cathodic and anodic photocurrent transients upon chopped illumination with magnitudes on the order of 0.1-0.2 $mA \cdot cm^{-2}$. This effects is noticeably different than what has been previously reported when coupling CoP_i with WO_3 electrodes.[22] In the latter case, there were no photocurrent transients observed and the maximum photocurrent density increased due to the increase in the rate of OER upon the growth of CoP_i on the surface. These results are similar to the

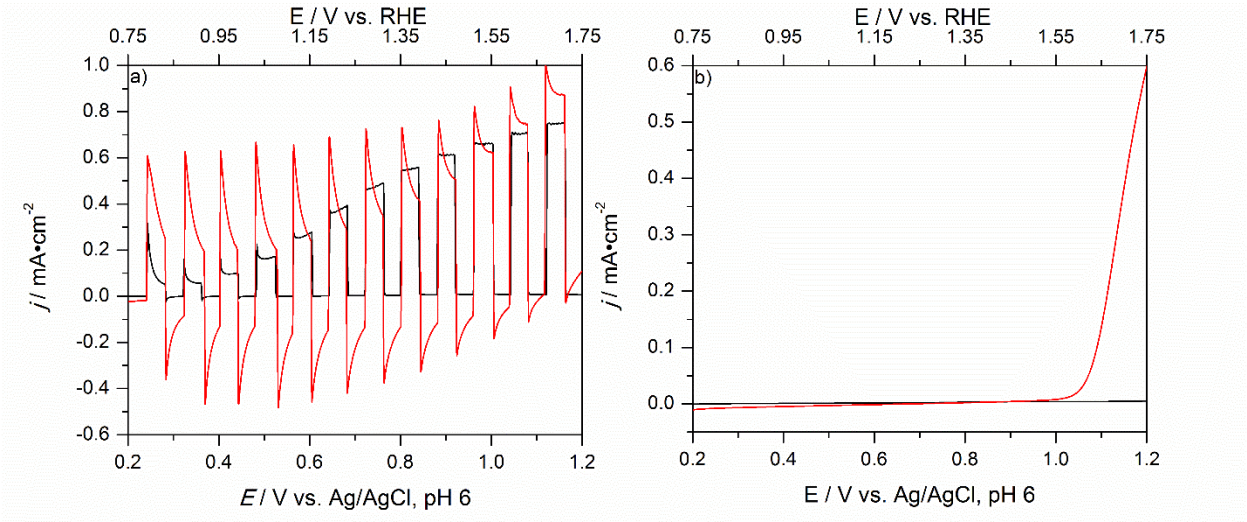

Figure 5.7: a) CL-LSV and b) dark LSV of a $PbCrO_4$ electrode before (black) and after (red) depositing a CoP_i electrocatalyst on the surface. For both experiments the electrolyte was pH 6 0.1M KP_i and the sweep rate was 20 mV/s. For the CL-LSV 100 mW•cm^{-2} was used.

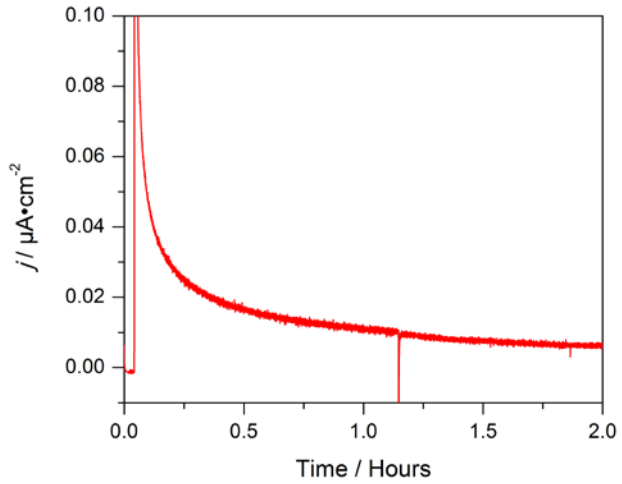

Figure 5.8: Controlled potential coulometry of a $PbCrO_4$-CoP_i electrode under 1 sun at 1.15V vs. RHE in a 0.1M KP_i pH 6 solution.

changes observed after performing controlled potential coulometry under illumination at an anodic applied bias with a $PbCrO_4$ (Figure 5.4a). This suggested that the $PbCrO_4$ may have degraded during the growth of CoP_i. However, we do still observe an increase in dark catalytic current in the LSV in the dark which is consistent with the growth of the CoP_i OER electrocatalyst (Figure 5.7 b).

To test the stability of the $PbCrO_4$-CoP_i electrode, controlled potential coulometry was conducted under 1 sun illumination. During the course of this experiment the photocurrent rapidly decayed by 80% over the course of 30 minutes (Figure 5.8). This photocurrent decay took place

over a shorter time than a similar $PbCrO_4$ electrode that did not have CoP_i. These results indicate that coating electrocatalyst on the surface of $PbCrO_4$ as means of passivating the electrode is not an effective strategy. Although CoP_i was deposited, it appears that during the course of the deposition, the $PbCrO_4$ electrode degraded. This is supported by the CPC data which depicts a more rapid photocurrent decay over time, possibly because the non-Faradaic degradation reaction had mostly already occurred during the CoP_i deposition.

5.5 Spray Pyrolysis of $BiVO_4$

To demonstrate the broad applicability of this synthesis we chose to synthesize $BiVO_4$ which is one of the most promising metal oxide photoanode materials to date.[2,15] It has been demonstrated to yield photocurrent densities as high as ~4 $mA \cdot cm^{-2}$ when coupled with a water oxidation co-catalyst[2] in addition to demonstrating good stability in neutral pH solutions. However, the synthesis of this material is still challenging and current spray pyrolysis methods require the use of highly acidic solutions to dissolve the Bi and V precursors.[25,26] Here we have produced stable precursor solutions using milder conditions by first chelating the metals with

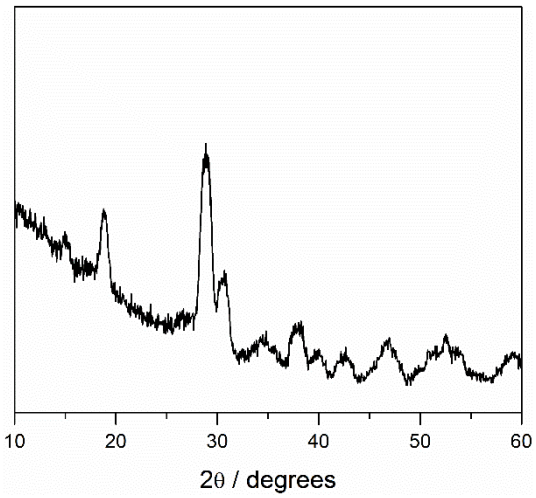

Figure 5.9: Powder X-ray diffraction pattern of a spray pyrolyzed $BiVO_4$ thin film deposited onto FTO coated glass.

EDTA. EDTA was selected as a chelator because it is hexadentate which occupies all the coordination sites around the chelated metal, and it displays a high binding affinity for Bi^{3+} and VO^{2+} ($\log(K_f)$ = 27.8, 18.7 respectively[11]). These two properties should increase EDTA's ability to bind the metals and prevent them from reacting with one another.

To prepare the precursor solution, first the Bi^{3+} (in the form of $Bi(NO_3)_3$) and VO^{2+} (in the form of $VO(acac)_2$) precursors were dissolved separately in aqueous solutions containing 1.2 equivalents of ammonium EDTA. The bismuth solution was a cloudy white color at first, however, after stirring for 2 hours at room temperature the white material was fully dissolved. For the V solution, the green $VO(acac)_2$ powder partially dissolved at first yielding a green solution. Over time the solution color changed from green to blue and the V fully dissolved. Once both the V and Bi precursors were dissolved in their respective solutions, they were mixed together and diluted with additional Millipore water to yield a final concentration of 0.01M in Bi and 0.01M in V. The resulting solution had a translucent blue color and no visible precipitate was formed. Furthermore, the solution was stable and no solids were formed even after a week of stirring at room temperature.

To produce $BiVO_4$ electrodes, the aforementioned precursor solution was sprayed onto FTO coated glass that was heated to 275°C. This yielded an amorphous brown film that was then annealed at 500°C to crystallize $BiVO_4$ as evidenced in the XRD pattern (Figure 5.9). Figure 5.10a demonstrates the photoelectrochemical response of these films with chopped light linear sweep voltammograms in pH 7 0.1M potassium phosphate (KP_i) buffered solutions. Photocurrent densities at 1.23 V vs. RHE were on the order of ~15 $\mu A \cdot cm^{-2}$.

To test the maximum current density under non kinetically limited conditions, 0.1M Na_2SO_3 was added to a solution of 0.1M KP_i at pH 7 to act as a hole scavenger. It has been reported that the slow kinetics of water oxidation on the surface of $BiVO_4$ can limit the photocurrent.[4]

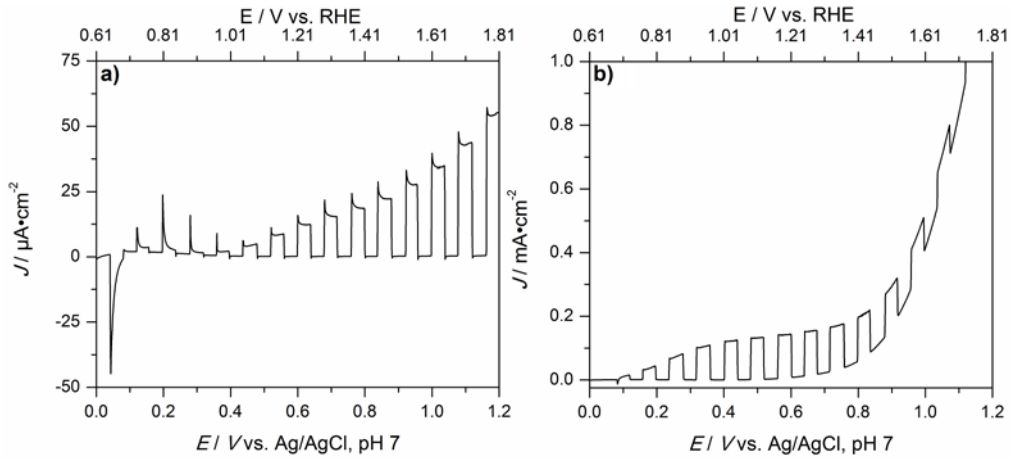

Figure 5.10: a) CL-LSV of a $BiVO_4$ thin film synthesized via spray pyrolysis. Solution is 0.1 KP_i, pH 7. b) CL-LSV of the same $BiVO_4$ thin film in 0.1M KP_i with 0.1M $NaSO_3$, pH 7. Illumination: 100 $mW \cdot cm^{-2}$ AM1.5G.

Adding efficient hole scavengers, such as Na_2SO_3, to the solution yields a better representation of the maximum current density that can be achieved. Furthermore, it has been demonstrated that these currents are comparable to that of hybrid systems that are composed of a metal oxide light absorber and a co-catalyst.[4] In the sulfite containing solution (Figure 5.10b), the photocurrent density at 1.23 V vs. RHE increases nearly tenfold from 15 $\mu A \cdot cm^{-2}$ to 130 $\mu A \cdot cm^{-2}$. These results demonstrate how chelating metal cations can result in stable precursor solutions of mild pH (~9) that can then be used to produce thin films of complex ternary metal oxides using spray pyrolysis.

5.6 Conclusion

We have demonstrated that a stable solution containing both Pb^{2+} and Cr^{6+} precursors can be formed by reacting the metal cations with a chelator such as EDTA prior to mixing. However, if no chelator was added to solution prior to mixing then solid $PbCrO_4$ crashes out of solution due to its limited solubility in aqueous solution at room temperature (solubility product, $Ks_0 = 6.4e^{-13}$).[27] We have also demonstrated that adding the EDTA to either solution will still yield a precipitate free precursor solution once the two are mixed which is most likely a result of EDTA's high binding affinity for Pb^{2+}.

Furthermore, $PbCrO_4$ has been previously reported to photocatalyze water oxidation in the presence of a sacrificial oxidant such as IO_3^-.[8] Using spray pyrolysis of the chelated precursors we successfully synthesized thin films of the ternary phase $PbCrO_4$ on fluorinated tin oxide coated glass. However, the resulting electrodes demonstrated poor stability under photoelectrochemical conditions in aqueous solutions. We hypothesize that this is a result of the formation of a PbO_2 passivation layer with concurrent release of CrO_4^{2-} into solution. This is supported by XPS data which reveal the absence of a Cr signal in addition to the broadening of the Pb signal. This behavior could be a result of the formation of a PbO_2 passivation film with concurrent dissolution of the CrO_4^{2-} species. Furthermore, we have observed that under photoelectrochemical conditions the degradation of the electrodes is particularly pronounced which suggests that this process is accelerated under illumination. Although the stability of this material is poor when oxidizing water photoelectrochemically, when thin films of $PbCrO_4$ were employed for MeOH oxidation they demonstrated much improved stability which indicates that $PbCrO_4$ electrodes could be employed as electrodes for organic oxidation reactions. Furthermore, we also demonstrated that a portion of the photocurrent can be recovered via reannealing a used electrode.

Finally, we have also explored electrode passivation using an electrochemically grown CoP_i electrocatalyst. For the growth of CoP_i we found that the photoelectrochemical growth conditions for the CoP_i still lead to the degradation of the $PbCrO_4$ as the degradation reaction appears to compete with Co^{2+} oxidation in that regime. As a result we hypothesize that using a more conformal growth technique, such as atomic layer deposition (ALD) to deposit a protective TiO_2 layer, would produce stable electrodes. Since ALD is low pressure growth technique that takes place in the absence of an applied electrical bias, we hypothesize that these growth conditions would mitigate any competition from the self-oxidation of $PbCrO_4$. In turn, ALD could yield conformal protective layers that would successfully stabilize the surface. This method has been applied with success to materials such as n-Si which allowed them to perform OER continuously without degrading.[28]

Finally, to demonstrate the broad applicability of this synthesis we sought to synthesize $BiVO_4$. This material has been demonstrated to function effectively as a water oxidation photoanode when coupled with appropriate co-catalysts. Although Bi and V precursors used for spray pyrolysis of this material typically are only soluble in highly acidic solutions,[25,26] we have demonstrated that by chelating the Bi^{3+} and VO^{2+} prior to mixing the two solutions a final precursor solution of intermediate pH can be formed. This solution can then be deposited onto a substrate using spray pyrolysis and finally annealed to obtain pure $BiVO_4$. Furthermore, the spray pyrolyzed $BiVO_4$ thin films yielded j_{max} values of 0.13 mA•cm^{-2} under 1 sun illumination in sulfite containing solution. We note that the electrodes produced using spray pyrolysis were not optimized for maximal photocurrent and thus we anticipate that with optimization this technique could afford a mild synthesis to yield high performing $BiVO_4$ electrodes.

5.7 Experimental

Materials. Potassium hydrogen phosphate (K_2HPO_4, 98.0% min., Alfa Aesar), potassium dihydrogen phosphate (KH_2PO_4, 99.0% min., Alfa Aesar), potassium hydroxide (KOH pellets, ≥85.0%, Fisher Chemical) were purchased from Fisher. (lead nitrate, EDTA, ammonium chromate) All reagents were used as purchased without further purification. Solutions were prepared using high purity water (Millipore Milli-Q purification system, resistivity > 18.2 MΩ).

Spray Pyrolysis of Metal Tungstate Electrodes.

$PbCrO_4$. To synthesize $PbCrO_4$ electrodes via spray pyrolysis, first two separate aqueous precursors of $Pb(NO_3)_2$ and $(NH_4)_2CrO_4$ were prepared. For the two solutions, 20 mL of Millipore was measured and dispensed into separate beakers. Then the desired equivalents of EDTA were added to each separate solution. The EDTA did not fully dissolve when added so 0.0017 mL/mg EDTA of concentrated NH_4OH was added to each beaker to fully dissolve the EDTA. After adding the NH_4OH 0.001 mol of $Pb(NO_3)_2$ was added to one flask and 0.001 mol of $(NH_4)_2CrO_4$ was added to the other. The separate solutions were left to stir for 30 minutes to give sufficient time for the EDTA to react. Dissolution of the $Pb(NO_3)_2$ was slow and sonication was employed to speed up the process. After the two solutions were fully dissolved, the Pb^{2+} containing solution was added to the CrO_4^{2-} solution and the resulting mixture was diluted to a total volume of 100mL with Millipore water. No precipitate was observed after mixing the two solutions.

After the precursor solution is prepared, an FTO coated glass substrate is placed on a hot plate, and heated to 275°C. Finally, the precursor solution is sprayed onto the heated substrate via a glass nozzle using a deposition pulse of 1 s and a resting pulse of 10 s. During the deposition, the nozzle sweeps from left to right to ensure full and even coverage on the substrate. The 10 s delay between each spray allows the solvent to evaporate between deposition cycles. Finally the electrode is annealed in a muffle furnace at 500°C for 1 hour with a ramp rate and cool down rate of 4.58 °C/min (2 hour ramp up and 2 hour cool down time).

$BiVO_4$. To synthesize $BiVO_4$ electrodes via spray pyrolysis, first two separate aqueous precursors of $Bi(NO_3)_3$ and $VO(acac)_2$ were prepared. For the two solutions, 20 mL of Millipore was measured and dispensed into separate beakers. Then 1.2 equivalents of EDTA were added to each separate solution. The EDTA did not fully dissolve when added so 0.0017 mL/mg EDTA of concentrated NH_4OH was added to each beaker to fully dissolve the EDTA. After adding the NH_4OH 0.001 mol of $Bi(NO_3)_3$ was added to one flask and 0.001 mol of $VO(acac)_2$ was added to the other. The separate solutions were left to stir for 30 minutes to give sufficient time for the EDTA to react. Dissolution of the $Bi(NO_3)_3$ was slow and sonication was employed to speed up the process. After the two solutions were fully dissolved, the Bi^{3+} containing solution was added

to the $VO(acac)_2$ solution and the resulting mixture was diluted to a total volume of 100mL with Millipore water. No precipitate was observed after mixing the two solutions.

After the precursor solution is prepared, an FTO coated glass substrate is placed on a hot plate, and heated to 275°C. Finally, the precursor solution is sprayed onto the heated substrate via a glass nozzle using a deposition pulse of 1 s and a resting pulse of 10 s. During the deposition, the nozzle sweeps from left to right to ensure full and even coverage on the substrate. The 10 s delay between each spray allows the solvent to evaporate between deposition cycles. Finally the electrode is annealed in a muffle furnace at 500°C for 1 hour with a ramp rate and cool down rate of 4.58 °C/min (2 hour ramp up and 2 hour cool down time).

Precipitation of $PbCrO_4$. To synthesize $PbCrO_4$ powders co-precipitation was employed. For this synthesis two separate solutions, one containing $(NH_4)_2CrO_4$ and the other $Pb(NO_3)_2$ were prepared by dissolving 0.001 mol of each compound in 50mL of Millipore water. After each salt was fully dissolved in its respective solution, the two were mixed together and solid $PbCrO_4$ crashed out of solution.

Materials Characterization. X-ray diffraction was recorded on a Bruker D8 Advance diffractometer equipped with a graphite monochromator, a Lynx-Eye detector, and parallel beam optics using Cu Kα radiation (λ = 1.541 84 Å). Patterns were collected using a 0.6 mm incidence slit, with a step size and scan rate of 0.04 °/step and 0.5 s/step, respectively. The $PbCrO_4$ and $BiVO_4$ phases were identified as #JCPDF 74-2304 and #JCPDF 14-0688, respectively. All synthesized materials were identified using MDI Jade version 5.0.

UV−vis spectra were recorded using a Cary 5000 spectrophotometer (Agilent) equipped with an external diffuse reflectance accessory. Spectra were recorded in reflectance mode and plotted as %R.

Scanning electron microscopy (SEM) images were collected using an FEI Nova Nanolab SEM/focused ion beam (FIB) instrument with an accelerating voltage of 10 kV, WD of 5 mm and beam current of 0.54 nA.

Photoelectrochemistry. Photoelectrochemistry was performed using a CH Instruments 660 C electrochemical workstation. All PEC measurements were performed in custom-built

cells with quartz viewing windows. Three-electrode voltammetry experiments were performed using the working $PbCrO_4$ or $BiVO_4$ thin-film photoanode, a Ag/AgCl (saturated KCl) reference electrode, and a Pt wire counter electrode. The supporting electrolyte in the PEC experiments was 0.1 M KP_i at pH 6 or 7. Unless specified otherwise, a 1 cm^2 area of the working electrode from the back side (glass side) was irradiated through a quartz window. The light source was a Newport-Oriel 150W Xe arc lamp fitted with an AM1.5G simulating solar filter (Newport). The lamp power was adjusted to 100 $mW \cdot cm^{-2}$ using an optical power meter (Newport 1918-R) equipped with a thermopile detector (Newport 818P-015-19).

5.8 References

(1) Lhermitte, C. R.; Bartlett, B. M. *Acc. Chem. Res.* **2016**, *49* (6), 1121.
(2) Park, Y.; McDonald, K. J.; Choi, K.-S. *Chem. Soc. Rev.* **2013**, 2321.
(3) Cooper, J. K.; Gul, S.; Toma, F. M.; Chen, L.; Liu, Y. S.; Guo, J.; Ager, J. W.; Yano, J.; Sharp, I. D. *J. Phys. Chem. C* **2015**, *119* (6), 2969.
(4) Seabold, J. A.; Choi, K.-S. *J. Am. Chem. Soc.* **2012**, *134* (4), 2186.
(5) Kudo, A.; Miseki, Y. *Chem. Soc. Rev.* **2009**, *38* (1), 253.
(6) Gómez-Quero, S.; Hernández-Mejía, C.; Hendrikx, R.; Rothenberg, G. *Dalton Trans.* **2012**, *41* (39), 12289.
(7) Errandonea, D.; Bandiello, E.; Segura, A.; Hamlin, J. J.; Maple, M. B.; Rodriguez-Hernandez, P.; Muñoz, A. *J. Alloys Compd.* **2014**, *587*, 14.
(8) Miseki, Y.; Kitao, O.; Sayama, K. *RSC Adv.* **2015**, *5*, 1452.
(9) Yourey, J. E. Photoelectrochemical and Photocatalytic Water Oxidation Using Metal Oxides, University of Michigan, 2014.
(10) Patil, P. S. **1999**, *Mat. Chem. Phys., 59, 185*.
(11) Harris, D. C. *Quantitative Chemical Analysis*, First.; Craig Bleyer: York, PA, 2007.
(12) Hamm, R. E. *J. Am. Chem. Soc.* **1953**, *75* (22), 5670.
(13) Garrett, A. B.; Vellenga, S.; Fontana, C. M. *J. Am. Chem. Soc.* **1939**, *61* (2), 367.
(14) McDonald, K. J.; Choi, K.-S. *Energy Environ. Sci.* **2012**, *5* (9), 8553.
(15) Martinez Suarez, C.; Hernández, S.; Russo, N. *Appl. Catal. A Gen.* **2015**, 504, 158.
(16) Hawaldar, R. R.; Sathaye, S. D.; Harle, A.; Gholap, R. S.; Patil, K. R. **2008**, 7557.
(17) Rondon, S.; Sherwood, P. M. A.; Rondon, S.; Sherwood, P. M. A. **2016**, *104*,1998.
(18) $PbCrO_4$ Pourbaix Diagram. https://materialsproject.org/#apps/pourbaixdiagram/%7B%22chemsys%22%3A[%22Pb%22%2C%22Cr%22]%7D (accessed Dec 23, 2016).
(19) Shen, M.; Henderson, M. A. *J. Phys. Chem. Lett.* **2011**, *2* (21), 2707.
(20) Yourey, J. E.; Bartlett, B. M. *J. Mater. Chem.* **2011**, *21* (21), 7651.
(21) Lhermitte, C. R.; Verwer, J. G.; Bartlett, B. M. *J. Mater. Chem. A* **2016**, *4*, 2960.
(22) Seabold, J. A.; Choi, K. *Chem. Mater.* **2011**, *23* (5), 1105.
(23) Nocera, D. G. *Acc. Chem. Res.* **2012**, *45* (5), 767.
(24) Reece, S. Y.; Hamel, J. A.; Sung, K.; Jarvi, T. D.; Esswein, A. J.; Pijpers, J. J. H.; Nocera, D. G. *Science.* **2011**, *334* (6056), 645.
(25) Dunkle, S. S.; Helmich, R. J.; Suslick, K. S. *J. Phys. Chem. C* **2009**, *113* (28), 11980.
(26) Abdi, F. F.; Firet, N.; vandeKrol, R. *ChemCatChem* **2013**, *5* (2), 490.

(27) Clever, H. L.; Johnston, F. J. *J. Phys. Chem. Ref. Data* **1980**, *9* (3), 751.
(28) Hu, S.; Shaner, M. R.; Beardslee, J. a; Lichterman, M.; Brunschwig, B. S.; Lewis, N. S. *Science* **2014**, *344* (6187), 1005.

Chapter 6

Conclusions and Outlook

6.1 Summary of the Presented Work

The focus of this thesis has been to obtain a more profound understanding of what chemical reactions occur on the surface of metal oxide electrodes during the course of photoelectrochemical water oxidation. In particular, understanding the effects of competing side reactions, such as electrode self-oxidation, electrode degradation, or anion oxidation is a central part of this work. Metal oxides were investigated as photoanodes to drive water oxidation photoelectrochemically due to their stability, visible light absorption, and appropriate band structure to drive OER thermodynamically. However, despite these attractive properties, a few key challenges associated with these materials remain.

First, not all metal oxides are stable in aqueous solution during photoelectrochemical water oxidation. Although many metal oxides demonstrate *chemical* stability in a wide range of pH values in aqueous solution—that is, they will not dissolve when soaked in an aqueous solution overnight—the work described in this thesis clearly demonstrates that this does not necessarily trend with stability under *photoelectrochemical* conditions. This effect is particularly prominent with the ternary phase metal oxide $PbCrO_4$. Although this material is chemically stable,—i.e., powders of this material do not appear to dissolve in a pH range of 3.45-10—under photoelectrochemical conditions, surface passivation via the formation of a PbO_2 layer dominates over OER.

Secondly, metal oxide materials can exhibit poor selectivity during, and turnover frequencies for, OER. This type of behavior suggests these types of heterogeneous surfaces are inefficient and slow at catalyzing OER on their surfaces. Furthermore, this type of behavior

indicates that the "all-in-one" approach of placing the burden of both light absorption *and* catalysis on a metal oxide is a poor strategy when attempting to produce electrodes that demonstrate high solar to O_2 conversion efficiencies. The work in this thesis largely suggests that attempting to dope materials or produce new ternary phase oxides may not be a fruitful approach to the production of photoelectrodes that demonstrate high turnover frequencies and Faradaic efficiencies for OER. Despite this conclusion, there are a few important and valuable lessons that have been learned along the way which will hopefully help guide the future directions for this work.

6.2 Ternary Phase Metal Oxide Design Principles

Chapter 4 described the effects of incorporating Co^{2+} into $CuWO_4$ electrodes to produce $Cu_{1-x}Co_xWO_4$ thin film solid solutions with a wide range of Co^{2+}/Cu^{2+} compositions. From a synthetic point of view, this work was a success since the resulting spray pyrolyzed electrodes demonstrated XRD patterns consistent with true solid solutions and not mixed $CuWO_4/CoWO_4$ phases. However, it was also observed that the incorporation of Co^{2+} led to an increase in photocurrent transients in addition to a decrease in the net photocurrent. These results suggest that the Co^{2+} in the materials behaved as a recombination center for photo-excited charges.

We hypothesize that this effect stems from Co^{2+}'s incomplete d-shell. Co^{2+} is a d^7 transition metal cation while Cu^{2+} is d^9. The introduction of additional partially filled d orbitals may contribute to the formation of new trap states where charges can recombine. Indeed, in the UV-Vis F(R) spectrum of the resulting thin film electrodes, a new, weak, absorption band between 500-600nm is observed (Fig 4.14). This suggests the introduction of new states below the bottom of the conduction band and that the optical transitions observed due to these states are related to LaPorte forbidden d-d transitions. Furthermore, because these grow with increasing Co^{2+} concentration in the thin films, this suggests that these new states are directly related to the Co^{2+}. This work demonstrates the importance of carefully selecting transitions metal dopants and further indicates that metal cations containing partially filled d-shells should be avoided.

Chapter 5 described the synthesis and photoelectrochemical behavior of the novel $PbCrO_4$ ternary oxide. This material was targeted due to the combination of d^{10} and d^0 metal cations present in its structure in the form of Pb^{2+} and Cr^{6+}. It was hypothesized that this combination of metal cations would yield a material that demonstrates a high absorption coefficient for light with energy

greater than the band gap. Indeed, it was observed that this material demonstrates a strong absorption for visible light with $\lambda \leq 550$ nm. Despite its visible light absorbing properties, $PbCrO_4$ was determined to be photoelectrochemically unstable during the course of PEC OER. It was demonstrated that this instability stems from surface passivation that arises due to the formation of a PbO_2 film with consequent stripping of Cr.

This work highlights the need to choose carefully the oxidation states of the metals in the resulting metal oxide. In the case of $PbCrO_4$, Pb is in the 2+ oxidation state. However, Pb is also known to adopt a stable 4+ oxidation state. This is problematic since Pb^{2+} can be oxidized to Pb^{4+} during the strongly oxidative conditions of PEC OER. Indeed, the data presented in chapter 5 reveals that this is the case. By comparison, a similar metal oxide, $BiVO_4$, is a much more stable material.[1] In this case, both metal cations are in their highest oxidation states, that is, Bi^{3+} and V^{5+}. With this configuration, neither cation can be further oxidized. I hypothesize that this improves the stability of this material under photoelectrochemical conditions in aqueous solutions. Thus this work demonstrates that selecting metal oxides that contain only metal cations in their highest stable oxidation state will most likely lead to photoelectrochemically stable materials.

6.3 Separating Light Absorption from Catalysis via the Synthesis of Binary Electrodes

In chapter 2, I presented my work on coupling WO_3 electrodes with the OER electrocatalyst, FeOOH. This electrode design served to improve electrode stability, turnover frequency for OER, and the Faradaic efficiency for OER. This strategy has proven to be effective for multiple types of light absorber/electrocatalyst combinations.[2–5] It has been demonstrated that if a conformal coating of the electrocatalyst can be obtained, then the chemical behavior of the resulting electrode is governed by the electrocatalyst on the surface.

This design strategy presents two main advantages. First, it removes the burden of catalysis from the light absorbing layer. This is important because many materials that demonstrate strong visible light absorption, such as $BiVO_4$, are pitiful OER photocatalysts in their own right. However, by loading an electrocatalyst on the surface of such electrodes, the turnover frequency for OER increases by orders of magnitude.[1,6,7] It is hypothesized that the more rapid kinetics of OER on the electrocatalysts is what causes the observed increases in photocurrent.[2,4,5,8] This is important because it reveals that the catalysis of the actual light absorbing material is not

particularly important and allows researchers to choose light absorbers from a wider class of materials since they no longer need to be limited to materials that can *both* absorb visible light effectively *in addition to* turning over OER at a high frequency.

Furthermore, these results also indicate that the electrocatalyst layer can also serve as a protective layer.[2,4] This trait is key since protecting the electrode allows its application in regimes in which it is not typically stable and thus extends the pH stability window, and ultimately the usefulness of the resulting electrode.

6.4 Summary and Concluding Remarks

With this thesis work I have demonstrated that competing side reactions can dominate on the surface of a photoelectrode during PEC OER conditions. However, it is possible to control and eliminate these side reactions from occurring by growing a conformal surface layer of a highly selective electrocatalyst. Furthermore, growing a surface layer can also dramatically improve the turnover frequency for OER as well which eliminates the need to select metal oxides that demonstrate good turnover frequencies for OER. This is key and suggests that future directions should focus on developing light absorbing metal oxides and electrocatalysts separately. Indeed, this type of architecture has demonstrated significant promise in the field.[2,4,5]

By separating the light absorption from the catalysis we allow for separate optimization of the visible light absorber and the actual catalyst. Although it may seem more difficult to have to produce two different materials, in reality this is the simpler solution. To date, no single material has demonstrated excellent light absorption in addition to high turnover frequencies for OER. However, some of the most promising electrode systems with the highest solar to H_2 conversion efficiencies are actually composed of binary electrodes.[1,9] This supports the notion that pursuing this type of design architecture may be the more fruitful approach to designing photoelectrodes that demonstrate higher solar to O_2 conversion efficiencies.

With this in mind, the next question becomes, where to next? Although researchers have demonstrated that this is an effective strategy, there currently lacks a fundamental understanding of charge transfer across the light absorber/electrocatalyst junction. In particular, it is not well understood how the chemistry on the surface of the electrocatalyst differs when it is loaded onto a

light absorbing metal oxide versus when it is employed as a simple electrode. In the former case the electrocatalyst can only be supplied with high energy holes from the valence band of the light absorbing metal oxide and for now there is no picture that can describe the surface processes that take place in that situation. This is an important question since these photogenerated holes could impact the surface chemistry, possibly making anion oxidation a more competitive process which, in turn, would affect the resulting Faradaic efficiencies.

Furthermore, it is still unclear as to whether it is actually improved kinetics on the surface or some other mechanism, such as improved carrier separation across a p-n heterojunction, which causes the observed improvements in the turnover frequency for OER. To probe these questions further it will be important to conduct kinetic measurements, such as Tafel plots, to observe how the behavior of the electrocatalyst changes when it is employed as a dark electrode versus when it is coupled as with a metal oxide light absorber to form a binary electrode system. Furthermore, it will be important to evaluate how the photocurrent of the metal oxide on its own in the presence of a hole scavenger such as H_2O_2 or $NaSO_3$, compares the photocurrent of the binary electrocatalyst/metal oxide electrode system. These experiments will inform us on how charge separation might be improved in the latter case.

In conclusion, it will be critical in the future to develop a deeper understanding of how the kinetics of OER differ when an electrocatalyst is employed on its own versus when it is coupled to an underlying metal oxide light absorber. From this, we could develop an understanding of which properties are most important to ensure effective charge separation and high turnover frequencies for OER on the electrode surface. Furthermore, it will also be important to further investigate ternary phase metal oxide materials as the light absorbers since these types of materials often exhibit smaller band gaps (~2.2 eV) which allows them to absorb a greater portion of the visible spectrum. From this thesis work, it appears that the most successful photoanode arrangement would be to couple an excellent light absorber along with an excellent electrocatalyst and thus I believe that in order to yield economically viable PEC materials, it will be crucial to investigate this type of architecture more thoroughly.

6.5 References

(1) Park, Y.; McDonald, K. J.; Choi, K.-S. *Chem. Soc. Rev.* **2013**, 2321.
(2) Seabold, J. A.; Choi, K. *Chem. Mater.* **2011**, *23* (5), 1105.

(3) Pilli, S. K.; Deutsch, T. G.; Furtak, T. E.; Turner, J. A.; Brown, L. D.; Herring, A. M. *Phys. Chem. Chem. Phys.* **2012**, *14* (19), 7032.
(4) Lhermitte, C. R.; Verwer, J. G.; Bartlett, B. M. *J. Mater. Chem. A* **2016**, *4* (2960–2968).
(5) Nocera, D. G. *Acc. Chem. Res.* **2012**, *45* (5), 767.
(6) Abdi, F. F.; Firet, N.; vandeKrol, R. *ChemCatChem* **2013**, *5* (2), 490.
(7) Ma, Y.; Pendlebury, S. R.; Reynal, A.; Le Formal, F.; Durrant, J. R. *Chem. Sci.* **2014**, *5* (8), 2964.
(8) Surendranath, Y.; Lutterman, D. A.; Liu, Y.; Nocera, D. G. *J. Am. Chem. Soc.* **2012**, *134* (14), 6326.
(9) Cesar, I.; Kay, A.; Martinez, A. G.; Gra, M. *J. Am. Chem. Soc. Comun.* **2006**, *128* (14), 4582.

Appendix A

Supporting Information for Chapter 2

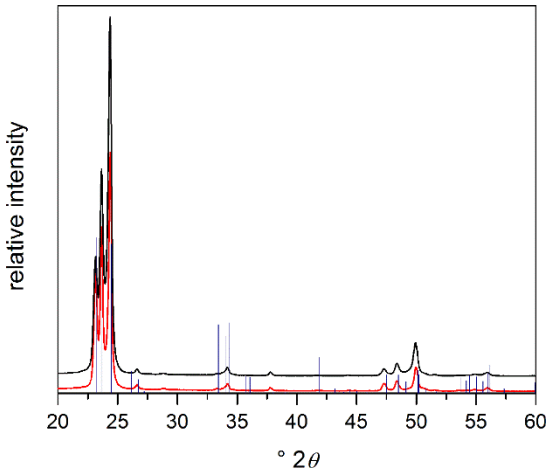

Figure A.1: Powder XRD pattern of WO_3 (black) and WO_3-FeOOH (red). Blue vertical lines represent indexed Bragg reflections for monoclinic WO_3.

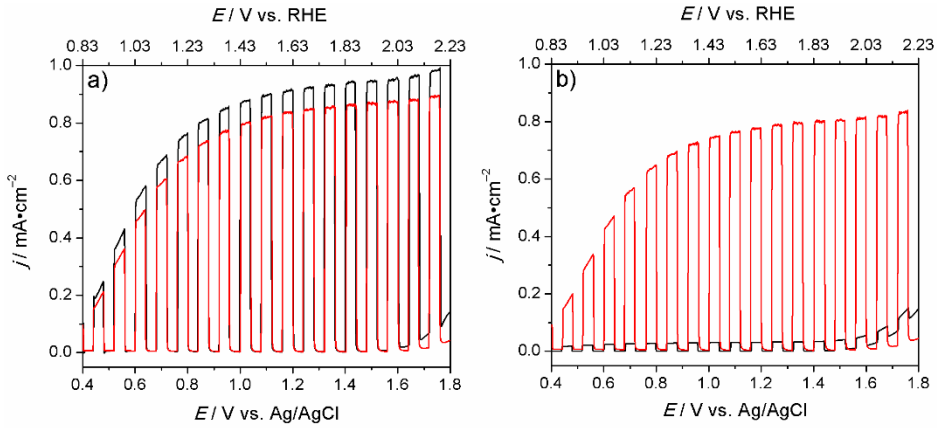

Figure A.2: CL-LSVs of WO_3 recorded before (red) and after (black) soaking 0.1 M KP_i buffer at a) pH 4; and b) pH 7.

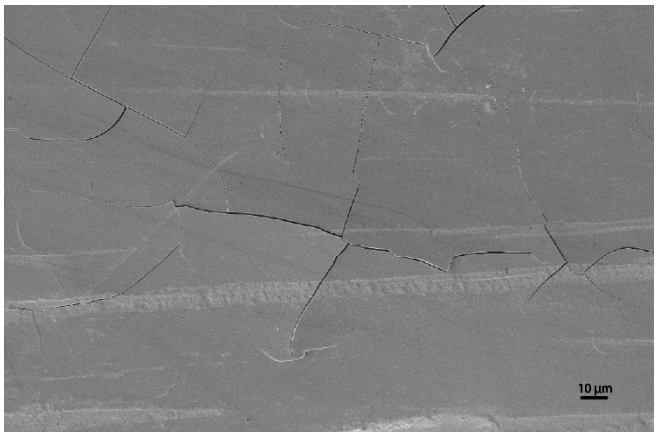

Figure A.3: SEM image of a cracked FeOOH on WO_3. The pictured film was synthesized using longer deposition times, generating a thicker layer. Cracking in the film was observed due to the film drying out.

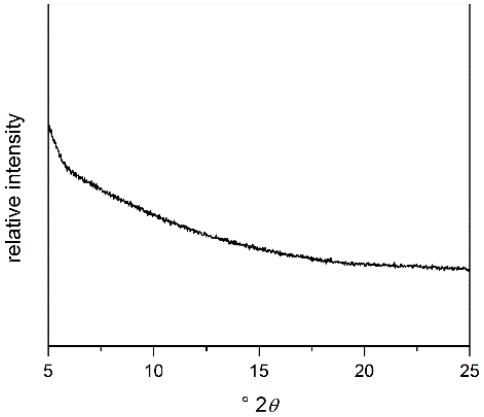

Figure A.4: Powder X-ray diffraction pattern of an electrodeposited FeOOH onto an FTO coated glass substrate.

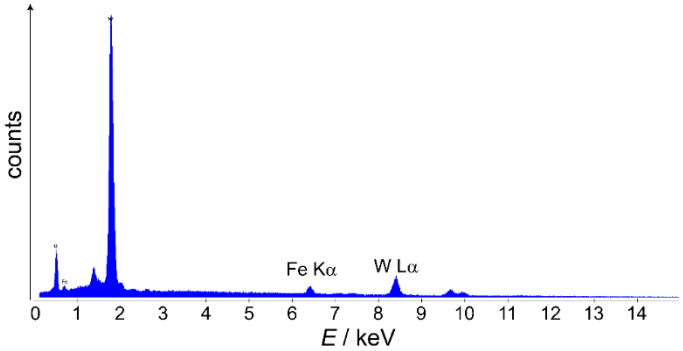

Figure A.5: EDX spectrum of a WO_3-FeOOH electrode.

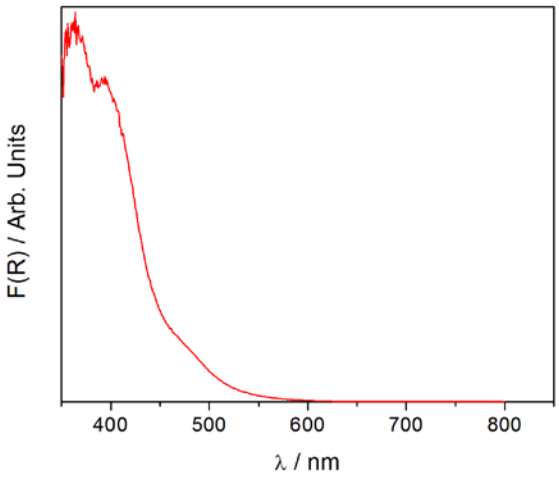

Figure A.6: F(R) spectrum for FeOOH electrochemically grown onto FTO.

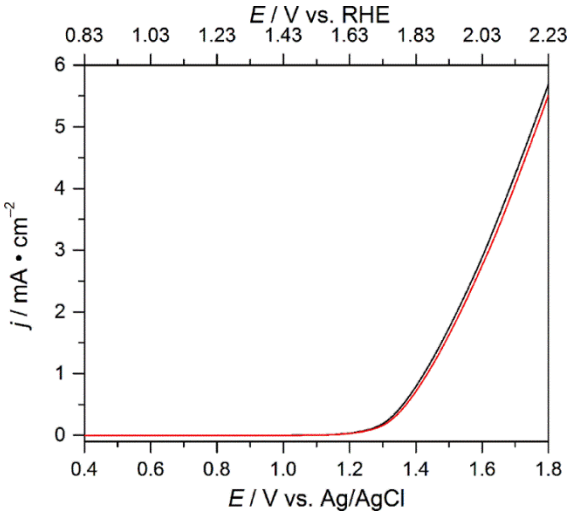

Figure A.7: LSV traces of FeOOH recorded in the dark (red) and under chopped light illumination (black).

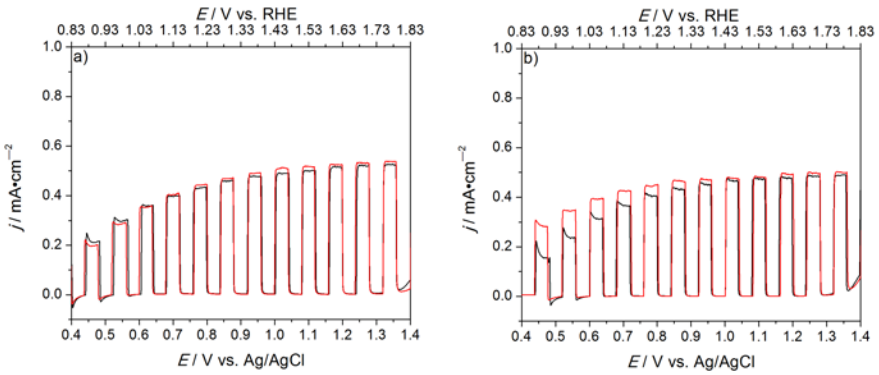

Figure A.8: CL-LSVs of a WO_3-FeOOH electrode before (black) and after (red) having been soaked overnight in a) 0.1M pH 4 KP_i and b) 0.1M pH 7 KP_i solutions. CL-LSVs were collected in 0.1M pH 4 KP_i under 1 sun illumination at 20 mV/s.

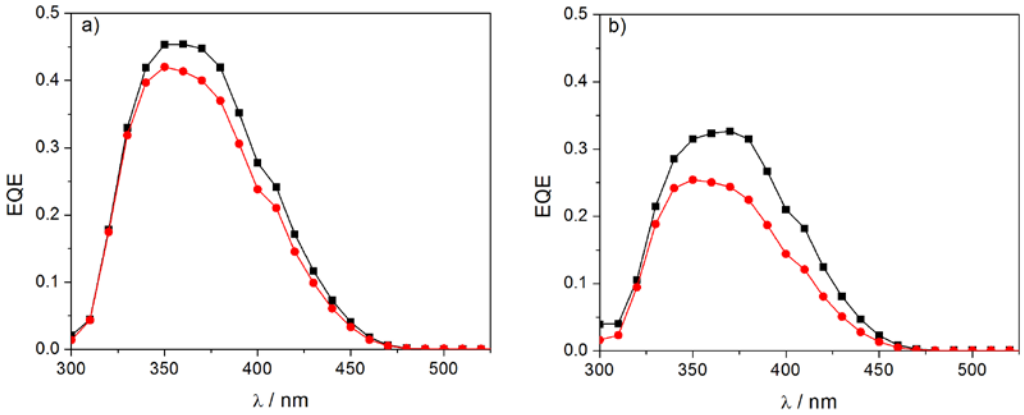

Figure A.9: EQE at different light chopping frequencies of a single WO_3 film before (a) and after (b) loading the FeOOH OEC. Black lines represent the EQE at 15Hz and red represent the EQE at 20 Hz.

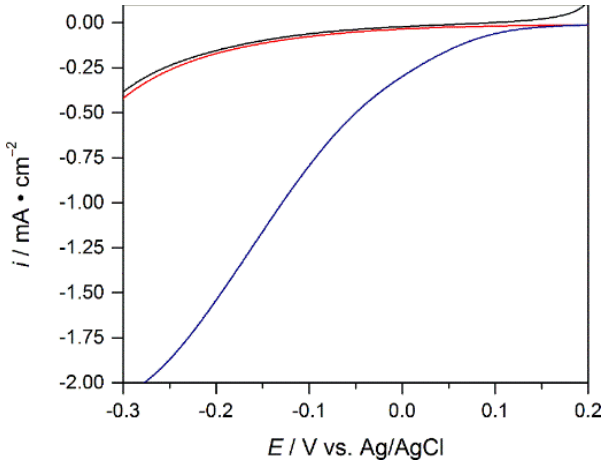

Figure A.10: Electrochemical detection of H_2O_2 on WO_3. Cathodic LSV scans were recorded before (black) and after (red) CPC of a WO_3 electrode under 1-sun AM1.5G illumination at 1.23 V vs. RHE for 2 hours in a 0.1 M KP_i buffer at pH 4. The blue line represents the cathodic scan of a WO_3 electrode in an identical solution that was spiked with 10 µL of H_2O_2.

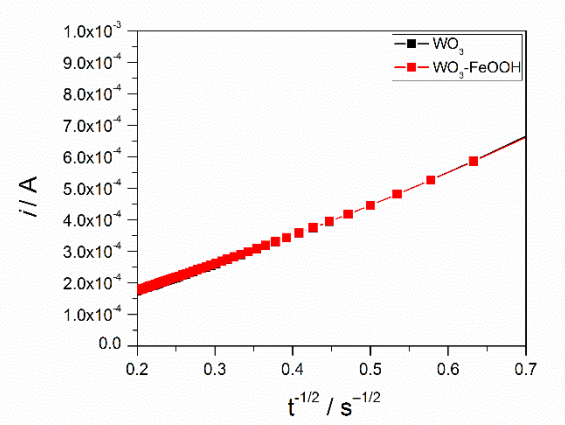

Figure A.11: Cottrell plot of the amperometric i-t curve. $[Fe(CN)_6]^{3-}$ reduction was measured at –0.05 V vs. Ag/AgCl in a 0.1 M KCl solution containing 6 mM $K_3[Fe(CN)_6]$. The Cottrell equation predicts a linear change in i vs. $t^{-1/2}$ and the slope is proportional to the active surface area of the electrode.

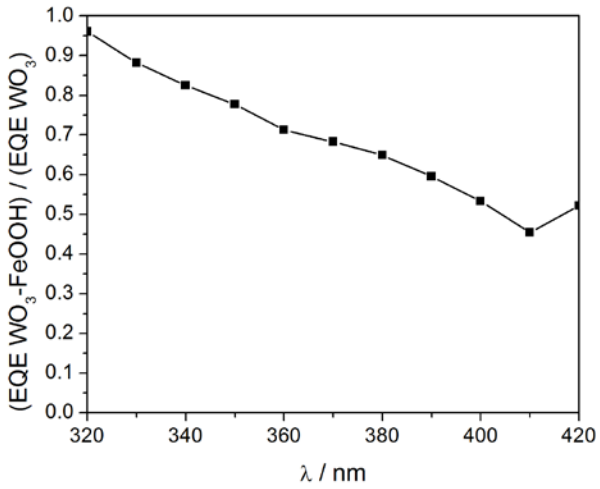

Figure A.12: (EQE WO_3) / (EQE WO_3-FeOOH). This plot was constructed from the data represented in Figure. 2.9 by taking the EQE of WO_3-FeOOH and dividing it by the EQE of WO_3. A decrease in (EQE WO_3-FeOOH) / (EQE WO_3) is observed with increasing wavelength due to parasitic absorption from the FeOOH.

Appendix B

Supporting Information for Chapter 3

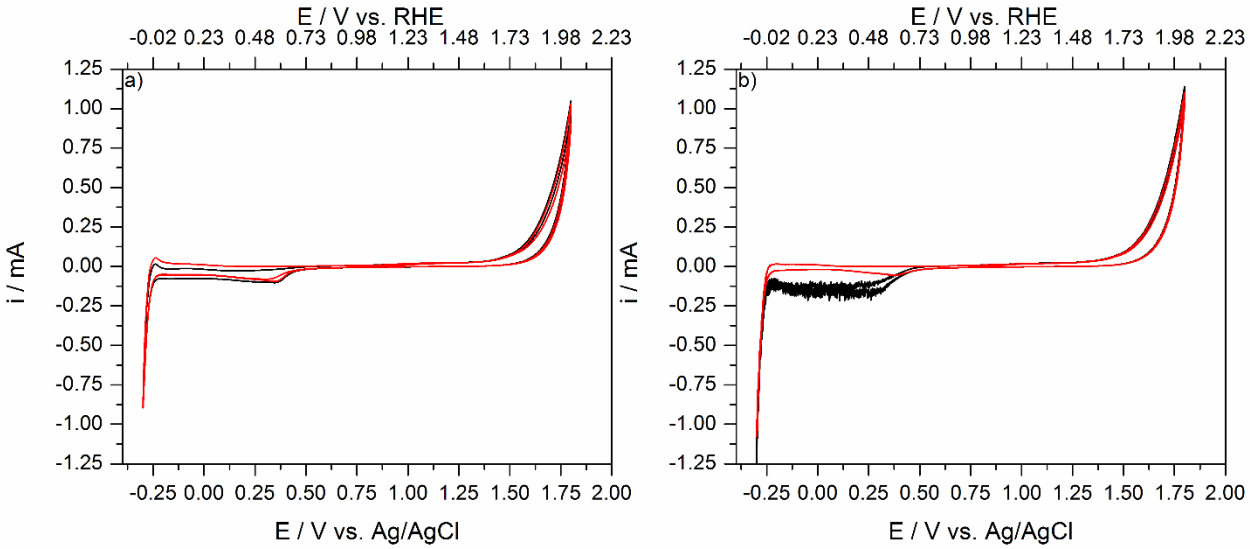

Figure B.1: Cyclic voltammograms of a Pt disk in 1N H_2SO_4 (pH 0.6) after saturation with O_2 (black) and N_2 (red) a) in a quiescent solution and b) while the solution was stirred at 500 RPMs. The stirred solution reveals that at potentials < 0.48 Vs. RHE the ORR is under diffusion control. The CVs were swept anodically first from OCP with a scan rate of 20 mV/s.

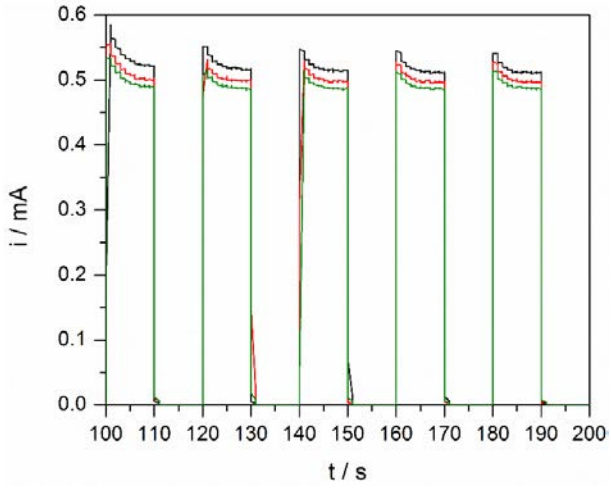

Figure B.2: Disk current for a WO_3:Pt disk under chopped illumination after consecutive runs in 1N H_2SO_4. Over consecutive runs the current was observed to decrease. Black was the first trial, red the second and green the third.

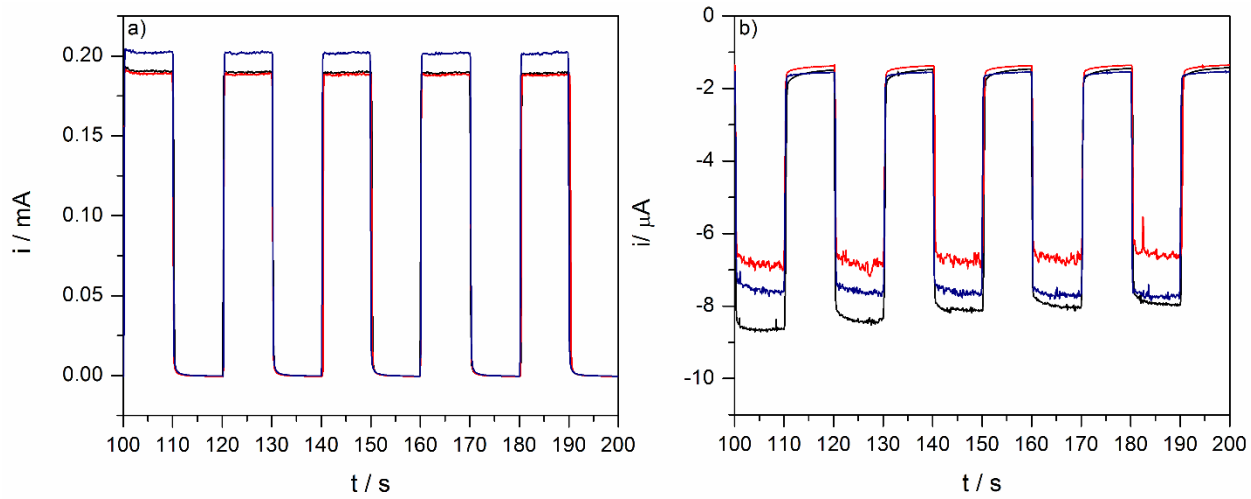

Figure B.3: a) disk current for a WO_3 thin film grown on Pt under chopped illumination after consecutive runs. b) Ring current at the Pt ring under chopped illumination after consecutive runs. For all trials the electrode was rotated at 2000 RPMs in 1N H_3PO_4. The applied potentials at the disk and the ring were 1.24 and 0.36 V respectively. The source of illumination was a 150W xenon lamp. (black) first trial, (red) second trial (blue) third trial.

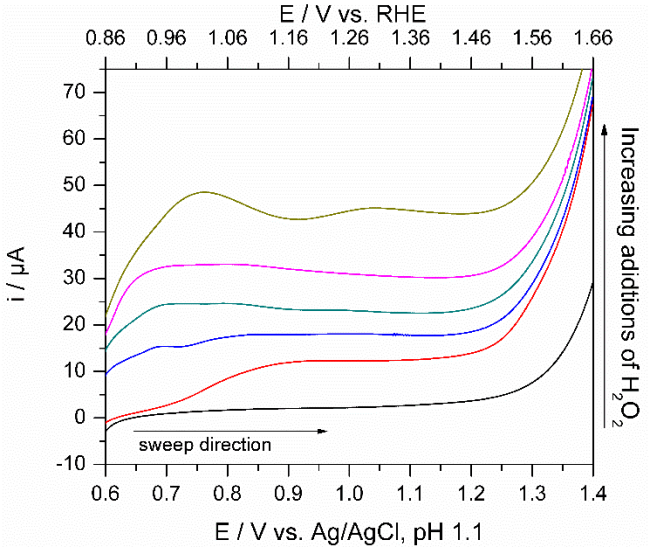

Figure B.4: Linear sweep voltammograms of the Pt ring with increasing additions of H_2O_2. Each LSV was taken after addition of 5 µL 10% v/v H_2O_2 starting with no H_2O_2 in 1N H_3PO_4 (black trace). Scan rate was 20 mV/s.

Appendix C

Supporting Information for Chapter 5

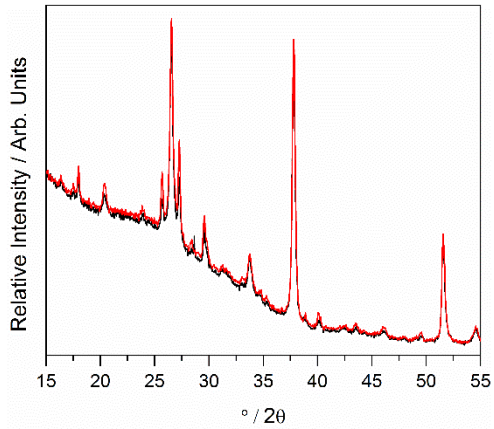

Figure C.1: Powder X-ray diffraction pattern of spray pyrolyzed $PbCrO_4$ using solutions that contained 1.5 eq. per metal (black) and 1 eq. per metal (red) EDTA.

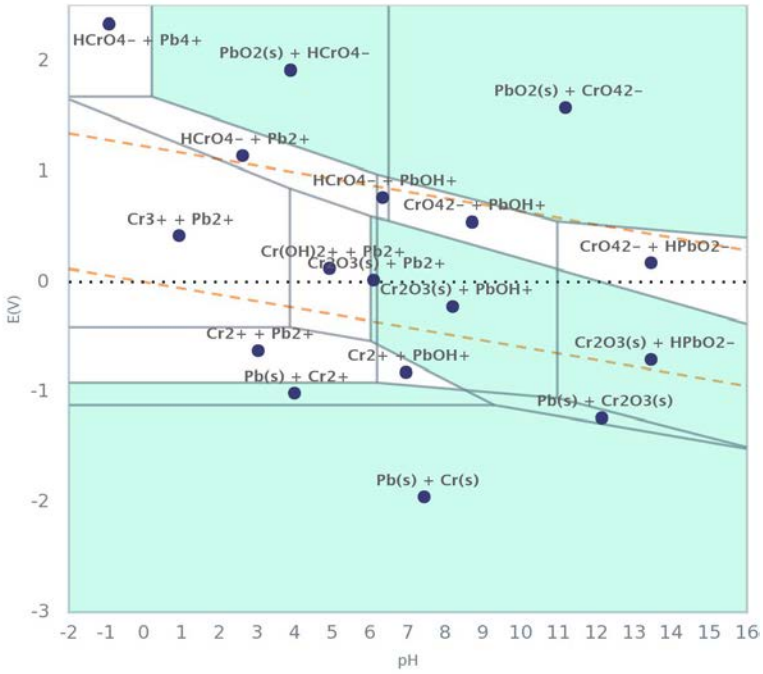

Figure C.2: Theoretical Pourbaix Diagram for $PbCrO_4$ in aqueous solution that contains 10^{-8} M Cr and Pb. Figure adapted from ref. 18 of Chapter 5.